

ALMA MATER STUDIORUM · UNIVERSITÀ DI BOLOGNA

SCUOLA DI SCIENZE
Corso di Laurea in Astrofisica e Cosmologia

Unveiling the AGN content and properties in a sample of interacting galaxies

Relatore:
Chiar.mo Prof.
Cristian Vignali

Presentata da:
Angelo Zaccardi

Sessione
Anno Accademico 2023/2024

Ciclo IV

Contents

Abstract	
1 Introduction	1
1.1 AGN structure	2
1.1.1 Supermassive Black Holes	2
1.1.2 Broad Line Region	5
1.1.3 Torus	6
1.1.4 Narrow Line Region	7
1.1.5 Jets and lobes	7
1.2 AGN classification	8
1.2.1 Radio classification	9
1.2.2 Infrared classification	10
1.2.3 Optical classification	11
1.3 The Unified model	12
1.4 AGN emission properties	12
1.4.1 Radio emission	13
1.4.2 IR emission	14
1.4.3 Optical-UV emission	15
1.4.4 γ -ray emission	15
1.4.5 X-ray emission	15
2 The SoSimple project	20
2.1 The presence of AGN in interacting galaxies	20
2.1.1 Detecting AGN activity in interacting/merging galaxies	22
2.1.2 X-ray observations of dual AGN	23
2.2 The SoSimple observing program	25
2.2.1 Scientific Objectives of SoSimple	27
2.3 The aim of my thesis	29
2.4 X-ray data in SoSimple	30

3	X-ray telescopes and data reduction	32
3.1	X-ray telescopes	32
3.1.1	The Effective Area	33
3.1.2	Angular and spectral resolution	34
3.1.3	Signal-to-noise ratio	35
3.2	Chandra X-ray Observatory	36
3.3	XMM-Newton	37
3.4	NuSTAR	38
3.5	Data reduction	38
3.5.1	Chandra data reduction	38
3.5.2	XMM-Newton data reduction	40
3.5.3	NuSTAR data reduction	41
3.6	Source detection	41
3.7	Spectral extraction	42
4	Analysis	47
4.1	Spectral analysis	47
4.2	Phenomenological models	48
4.2.1	Power law	48
4.2.2	Absorption components	48
4.2.3	Emission line component	48
4.2.4	Thermal emission component	49
4.3	χ^2 and Cash statistics	51
4.4	Main outcomes from X-ray spectral analysis	54
4.4.1	AM 0018-485	54
4.4.2	AM 0642-801	57
4.4.3	AM 0519-611	60
4.4.4	AM 2133-384	63
4.4.5	AM 2026-424 (ESO285-G019 West and East)	66
4.4.6	Arp 200	68
4.4.7	Arp255 (UGC 05304b)	70
4.4.8	Arp 303	72
4.4.9	Arp 245	75
4.4.10	AM 2048-571	80
4.5	Undetected X-ray sources	84
4.5.1	Chandra	84
4.5.2	XMM	86
4.6	More consideration about IC 5063 and NGC 2992	88
4.6.1	IC 5063	89
4.6.2	NGC 2992	91
4.7	Additional information from the preliminary MUSE analysis	94

5	Discussion and future prospects	98
5.1	Discussion	98
5.1.1	MUSE Spectroscopy and AGN-SF discrimination	102
5.2	Conclusion and future prospects	104
A	Dataset table information	106
B	MUSE spectra	107

Abstract

The role of Active Galactic Nuclei (AGN) in galaxy evolution remains a crucial open question in astrophysics, particularly in the context of galaxy interactions and mergers. Mergers are known to trigger gas inflows toward galactic centers, potentially fueling both AGN activity and star formation. However, the precise mechanisms governing AGN activation in interacting systems and the relative contribution of different physical processes remain debated.

In this regard, the SoSimple (Snapshot Optical Spectroscopic Imaging of Mergers and Pairs for Legacy Exploration) project is a major observational campaign utilizing the MUSE instrument at VLT to systematically study over 150 interacting galaxies in the southern hemisphere, selected from the Arp and Arp-Madore catalogs. This sample is morphologically selected, making it free from AGN-related biases and ideal for investigating the role of galaxy interactions in shaping star formation, gas dynamics, and, in particular, AGN activity. Complementary X-ray follow-up observations provide additional insights into nuclear activity, enabling a multi-wavelength approach to study SMBH accretion and galaxy evolution during mergers.

As part of this effort, we conduct a detailed X-ray spectral analysis using data from Chandra, XMM-Newton, and NuSTAR, focusing on AGN detection, and using purely phenomenological spectral models to derive the most relevant spectral properties, such as X-ray photon index, column density, observed flux, and intrinsic X-ray luminosity.

As interesting results, the possible presence of a Compton-thick AGN in the galaxy NGC 0089 (part of the AM 0018-485 system) can be highlighted for the first time, given the detection of a high column density ($N_{\text{H}} > 10^{24} \text{ cm}^{-2}$) and the presence of a prominent iron line. Additionally, the presence of an active AGN has been confirmed for the well-known galaxies NGC 2992 and IC 5063, consistent with their Seyfert Type-II (i.e. obscured) classification. The presence of a fourth AGN, though candidate, ESO285-G019 West (of the AM 2026-424 system), is also highlighted. It exhibits an X-ray luminosity exceeding 10^{41} erg/s , which could indicate the presence of an AGN. For the rest of the sample, the 2-10 keV luminosities lie in the range $\sim 10^{39-41} \text{ erg/s}$, leaving some uncertainty about their classification. They could potentially be classified as low-luminosity AGN, star-forming galaxies, or a combination of both.

In parallel with the X-ray analysis, we have initiated a preliminary optical spectroscopic study (using MUSE data) of these sources to further provide hints on their classification. Future work will expand this effort by constructing a proper Baldwin-Phillips-Terlevich (BPT) diagnostic diagram, allowing for a more precise separation on the classification of AGN and star-forming galaxies (or composite systems), as well as providing constraints on the ionization mechanisms at play. Additionally, increasing the sample size will enhance statistical significance and provide a more comprehensive picture

of the relationship between galaxy interactions, nuclear activity, and AGN obscuration properties.

This study underscores the importance of multi-wavelength approaches in AGN identification and classification. Further observations and deeper optical spectroscopic analysis will be crucial in refining AGN demographics in merging systems and assessing the role of galaxy interactions in shaping nuclear activity.

Chapter 1

Introduction

Active Galactic Nuclei (AGN) are fascinating astrophysical objects known for their high-energy output and significant impact on various aspects of astrophysics and cosmology. These objects serve as powerful converters of matter into energy through gravitational accretion processes around Super Massive Black Holes (SMBHs), with masses ranging from approximately 10^6 to 10^{10} times that of our Sun.

The effects of AGN activity extend over different scales. They influence the properties of galaxies on kiloparsec (kpc) scales and can have an impact on the megaparsec (Mpc) scales of entire Galaxy Clusters. Additionally, AGN play a crucial role in understanding the evolution of galaxies over cosmic time.

AGN are not ubiquitous, being present in up to a few percent of galaxies. The emission from AGN is observable across the entire electromagnetic spectrum. The bolometric luminosity of AGN can reach extremely high values, up to $L \sim 10^{14-15}$ times the solar luminosity. This immense energy output is attributed to various emission processes and different environmental factors, such as the type of galaxy and the nature of the accretion.

In studying AGN, scientists often analyze their Spectral Energy Distributions (SEDs), which is a representation of the energy output at different wavelengths. The SED provides insights into the contribution of different emission processes and allowing astronomers to classify and understand the nature of AGN.

The following sections delve into the structural and emission properties of AGN, as well as their classification schemes. This includes details about the physical characteristics of the surrounding material, the mechanisms driving the energy release, and the observational features that aid in categorizing different types of AGN. Understanding AGN is crucial for advancing our knowledge of the Universe large-scale structure and the processes influencing galaxy evolution.

1.1 AGN structure

Describing AGN requires a fundamental characterization of their structure in relation to their distinct constituents. This discussion focuses on the primary physical properties found in the nuclear regions and the diverse components that form the widely accepted AGN paradigm.

1.1.1 Supermassive Black Holes

The essential requirement for the presence of an AGN is the existence of a SMBH. The gravitational influence of matter accreting onto the central black hole which is present in nearly every galaxy, is a pivotal factor driving nuclear activity and the potential emergence of an active nucleus.

SMBHs, as the name suggests, are black holes with masses significantly surpassing stellar mass (1-100 M_{\odot}) and intermediate mass (10^2 - $10^5 M_{\odot}$) black holes, falling within the range of approximately 10^6 - $10^{10} M_{\odot}$. According to the “no-hair” theorem (Wheeler et al. 1971), a black hole can be described using only three fundamental parameters: the black hole mass (M_{BH}), the angular momentum (J), and the black hole electric charge (Q) (in this discussion $Q = 0$).

For a black hole with a given mass (M_{BH}), a characteristic scale length, called the gravitational radius (r_g), can be defined as follows:

$$r_g = \frac{M_{BH} \cdot G}{c^2} \sim 1.5 \cdot 10^{13} M_8 \quad [cm] \quad (1.1)$$

where G is the universal gravitational constant, M_{BH} is the black hole mass, M_8 represents the black hole mass in units of $10^8 M_{\odot}$, and c is the speed of light.

Another significant scale radius associated with a black hole is the Innermost Stable Circular Orbit (ISCO), defined as the last stable circular orbit below which a particle will fall onto the black hole. To describe the properties of the ISCO, the dimensionless black hole spin parameter (a) is introduced:

$$a = \frac{J \cdot c}{M_{BH}^2} \quad (1.2)$$

The event horizon r_{\pm}^{\pm} is then determined by the spin parameter:

$$r_+ = r_g \sqrt{1 - a^2} \quad (1.3)$$

For a non-rotating black hole (Schwarzschild BH, $a=0$), $r_+=2r_g$, and for a maximally spinning black hole (Kerr BH, $a=1$), $r_+=r_g$. The ISCO radius in these extreme cases can be computed using the event horizon radius: for a static black hole, the ISCO radius is $r_{ISCO}=6r_g$ and for a Kerr black hole, $r_{ISCO}=1.24r_g$.

These parameters are challenging to be constrained by through observations. Information on the black hole spin can be derived from studying jet properties or gravitational distortion effects on the Fe $K\alpha$ line (Fabian and Miniutti 2005). Black hole mass estimation can be accomplished through variability effects, emission-line equivalent width, stellar rotation curves, reverberation mapping phenomena, and galaxy-scale relations linking observable galaxy properties to central black hole mass.

Mechanism of accretion

As previously stated, the primary source of power in an AGN is the accretion of matter onto the SMBH. The precise mechanisms governing how matter “navigates” the gravitational field of the black hole before falling onto it are understood only partially. Extensive research has shed light on the fundamental physical processes occurring during accretion. One simplified yet useful approach to studying these accretion processes involves defining the Eddington Luminosity (L_{Edd}). Consider a scenario where ionized hydrogen gas is distributed spherically around the black hole. In this setup, two primary forces come into play:

- Gravitational Force (F_g): this force, exerted by the black hole’s gravitational field, acts to attract the gas toward the black hole

$$F_g = \frac{GM_{BH}m_p}{r^2} \quad (1.4)$$

with G gravitational constant, M_{BH} is the black hole mass, m_p the proton mass and r the radial distance from the central black hole.

- Radiation Pressure Force (F_p): this force arises from the pressure exerted by the radiation field generated by the heating of the gas. This radiation pressure opposes the gravitational force and tends to push the gas away from the black hole

$$F_p = \frac{L\sigma_T}{4\pi r^2 c} \quad (1.5)$$

where L is the luminosity, σ_T the Thomson cross section and c the light velocity.

In essence, the competition between these forces dictates the behavior of the gas. While gravity pulls the gas inward, radiation pressure counteracts this by exerting an outward force. The interplay between these forces determines the dynamics of accretion around the black hole, influencing the rate at which matter accumulates onto it and, consequently, the luminosity emitted by the AGN.

When assuming the gas is in equilibrium between the gravitational force pulling it inward and the radiation pressure pushing it outward, the luminosity at this equilibrium

is known as L_{Edd} . It can be calculated using the formula:

$$L_{\text{Edd}} = \frac{4\pi G m_p c}{\sigma_T} M_{\text{BH}} \sim 1.3 \cdot 10^{38} \left(\frac{M_{\text{BH}}}{M_{\odot}} \right) \quad (1.6)$$

This formula provides an approximate estimate of the maximum luminosity emitted by the AGN when the black hole mass is known.

Another important parameter associated with the Eddington luminosity is the Eddington accretion rate (\dot{M}_{Edd}), which is the accretion rate required to sustain a luminosity equal to the Eddington luminosity. It is given by:

$$\dot{M}_{\text{Edd}} = \frac{L_{\text{Edd}}}{\eta c^2} \quad (1.7)$$

where η is the efficiency of accretion, typically around $\eta \approx 0.1$ (this value is related to the type of black hole under consideration, for Kerr-type black holes it tends to be higher, up to 0.3-0.4 than for Schwarzschild-type black holes). The rate at which the black hole grows in mass is then $\dot{M} = (1 - \eta)\dot{M}_{\text{Edd}}$.

However, in most cases, the accretion process occurring around a SMBH differs from the simple assumptions made for calculating the Eddington luminosity. It is believed that accretion typically does not occur in a spherically symmetric manner, but instead through a disk-like, azimuthally symmetric structure on sub-parsec scales. These accretion disks found in AGN can vary in geometry, from geometrically thin to slim or thick, and may be optically thin or thick. Different disk properties imply various types and efficiencies of accretion onto the black hole. Two of the most prominent accretion models through a disk are the Shakura-Sunyaev model (Shakura et al. 1973) and the ADAF (Advection Dominated Accretion Flow) model (Ichimaru 1977; Narayan and Yi 1994; Abramowicz et al. 1995; Chen et al. 1995).

The Shakura-Sunyaev model is characterized by a geometrically thin, optically thick disk that emits thermally as a multicolor black body (Mitsuda et al. 1984). This emission arises from individual black-body emissions at different wavelengths (and temperatures), resulting in a spectrum like the left figure of 1.1. Typical temperatures of the accretion disk are around $10^5 - 10^6$ K, leading to emissions predominantly in the ultraviolet spectrum for typical black hole masses. The temperature of the disk depends on both the black hole mass and the distance from the center according to the relation (e.g. Peterson 2008):

$$T(r) = \left[\frac{3GM_{\text{BH}}\dot{M}}{8\pi\sigma r^3} \left\{ 1 - \left(\frac{R_{\text{in}}}{r} \right)^{\frac{1}{2}} \right\} \right]^{\frac{1}{4}} K \quad (r < R_{\text{in}}) \quad (1.8)$$

$$T(r) \approx 3.7 \cdot 10^5 \dot{M}^{\frac{1}{4}} \left(\frac{M_{\text{BH}}}{10^8 M_{\odot}} \right)^{-\frac{1}{4}} \left(\frac{r}{r_g} \right)^{-\frac{3}{4}} K \quad (r \gg R_{\text{in}}) \quad (1.9)$$

This type of disk is often associated with high-luminosity and efficiently accreting AGN.

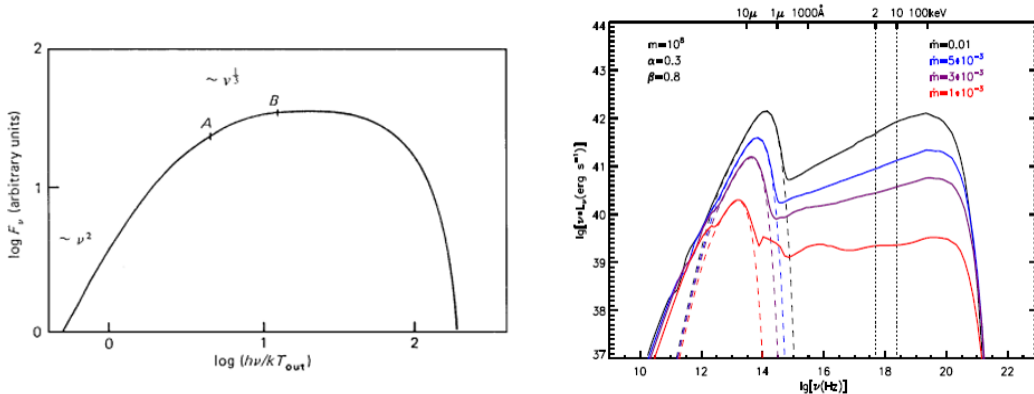


Figure 1.1: (Left panel): geometrically thin, optically thick-accretion disk spectrum as a function of the frequency. The units are arbitrary. Reproduced from FKR92.

(Right panel): spectra of an accretion disk around a black hole, which incorporates both an inner ADAF and an outer truncated accretion disk, are predicted by the disk evaporation model with a black hole mass of $10^8 M_\odot$, $\alpha=0.3$ and $\beta=0.8$ (the viscosity and magnetic parameter, respectively). The solid lines represent the combined emergent spectra from the inner ADAF plus the outer truncated accretion disk for mass accretion rates of \dot{m} of 10^{-3} , 3×10^{-3} , 5×10^{-3} and 0.01 , respectively, from bottom to top. The dashed lines represent the emergent spectra solely from the truncated accretion disk. From Qiao et al. 2013.

On the other hand, geometrically thick, optically thin accretion disks are often associated with low-efficiency AGN, where the luminosity is typically below few percent of the Eddington luminosity. The spectra of sources accreting via the ADAF mechanism tend to be harder (see figure 1.1), both for binary systems and AGN (Narayan and McClintock 2008).

1.1.2 Broad Line Region

The Broad Line Region (BLR) typically lies at distances ranging from 0.1 to 1 parsec from the central Black Hole (BH) and consists of dense clouds with densities around $10^9 - 10^{10} \text{ cm}^{-3}$ surrounding the BH. Optical emission lines are produced by the BLR due to excitation induced by the nuclear radiation.

These emission lines indicate the presence of a moving medium, with velocities typically ranging from 10^3 to 10^4 km/s and temperatures around 10^4 K. Due to its location within the obscuring torus, the BLR is not observed in all AGN, leading to different sources classification in Broad line and Narrow line galaxies (detailed in section 1.2.3).

Additionally, polarization studies (Antonucci and Miller 1985) have revealed the pres-

ence of broad emission lines in polarized light even in sources where the BLR cannot be directly detected.

1.1.3 Torus

A fundamental component in the paradigm of AGN and the history of AGN classification is the dusty torus. Traditionally, the obscuring torus has been conceptualized as a smooth and doughnut-shaped structure. The modeling of the obscuring torus, as pioneered by Krolik 1988, played a pivotal role in the development of the first unified theories, such as the work by Urry et al. 1995, aimed at explaining the observed differences between Type 1 and Type 2 AGN. The obscuring torus is believed to consist of a distribution of dusty and molecular matter surrounding the SMBH, within its gravitational influence, at distances ranging from about 1 to 30 parsecs (e.g., studies by Jaffe et al. 2004 and Hickox et al. 2018).

Evidence supporting the existence of the torus is derived from observations across the entire electromagnetic spectrum, with particular emphasis on the mid-infrared and X-ray bands. The torus absorbs the nuclear radiation emitted by the AGN; this radiation is thermalized and subsequently re-emitted primarily in the mid-infrared portion of the spectrum.

Initially, simplistic smooth and azimuthally symmetric models were employed to describe the distribution of obscuring material in AGN tori. These models are characterized by parameters such as the torus opening angle, which is linked to the covering factor of the obscuring material, and assume homogeneity within the material. In this configuration, the extent of source obscuration is solely determined by the geometry of the torus; therefore, the source is obscured if its radiation intersects the obscuring material.

Recent advancements in observational quality have required more sophisticated models of the obscuring torus, such as those proposed by Nenkova et al. 2002, Jaffe et al. 2004, Burtscher et al. 2013. Some of these models are capable of replicating the clumpiness observed in X-ray spectral fitting, often leveraging infrared information as well (as demonstrated by Buchner et al. 2019). The most widely accepted torus model today is the clumpy or patchy torus.

A patchy torus comprises multiple clouds, each possessing its own absorption and thermal properties determined by factors such as size and composition. In this framework, features are typically in absorption, e.g. the Silicate feature at $9.7 \mu\text{m}$ (Hatziminaoglou et al. 2015) if the torus is seen edge-on, otherwise in emission.

Additionally, alternative models have been explored, which are based on the presence of a wind generated near the disk by magnetic fields, as proposed by Elitzur 2008. These alternative models provide further insight into the complex dynamics and structure of the obscuring material in AGN tori.

1.1.4 Narrow Line Region

Above and below the dusty torus, there exist clouds where the gas velocities typically range from 300 to 1000 km/s. This region is known as the Narrow Line Region (NLR), and it extends over typical sizes ranging from hundreds of parsecs to a few kiloparsecs. Narrow emission lines are produced within the NLR.

Positioned outside the torus, the NLR is likely to be affected only mildly by extinction effects and observable in almost all AGN. Compared to the BLR, the density of the NLR is lower, typically around 10^4 particles per cubic centimeter. Additionally, the temperature of the NLR gas ranges between 10^4 and $2.5 \cdot 10^4$ K.

Numerous studies have investigated the morphology of the NLR, revealing shapes such as bi-conical or hourglass-like structures. For example, Das et al. 1985 utilized a combination of optical and radio observations to delve into the kinematics of the NLR. They found that the NLR behavior can be well-described by a bi-conical outflow model.

1.1.5 Jets and lobes

In the presence of radio-loud AGN (see section 1.2.1) there are two additional components, jets and lobes. These features are unique to radio-loud AGN, which constitute only a small fraction of the overall AGN population, about 10%.

Jets emit radiation across a wide range of wavelengths, from gamma-rays to the radio band, and represent highly collimated outflows originating in the inner regions of the AGN. The primary emission mechanism responsible for jet radiation is synchrotron radiation, generated through the interaction between relativistic electrons and magnetic fields near the AGN nucleus. Jets are believed to form due to the combined effects of black hole rotation, accretion disk dynamics, and the presence of magnetic fields, as proposed by Blandford and Znajek 1977 and Blandford and Payne 1982.

Jets often give rise to the formation of large-scale radio-emitting lobes spanning kiloparsec to megaparsec scales. These structures are characteristic features of radio galaxies and result from the interaction between the energetic jets and the surrounding environmental medium, which can consist of either the Inter Galactic Medium (IGM) or the Intra Cluster Medium (ICM).

In Figure 1.2, a schematic representation of the structure of an AGN as a function of distance from the center, where the SMBH is located, is depicted. It can be observed that the BLR is situated within the region of the dusty torus, indicating the difficulty in observing this component in obscured systems. On the other hand, the NLR is shown to be outside the torus, making it more easily detectable in all systems.

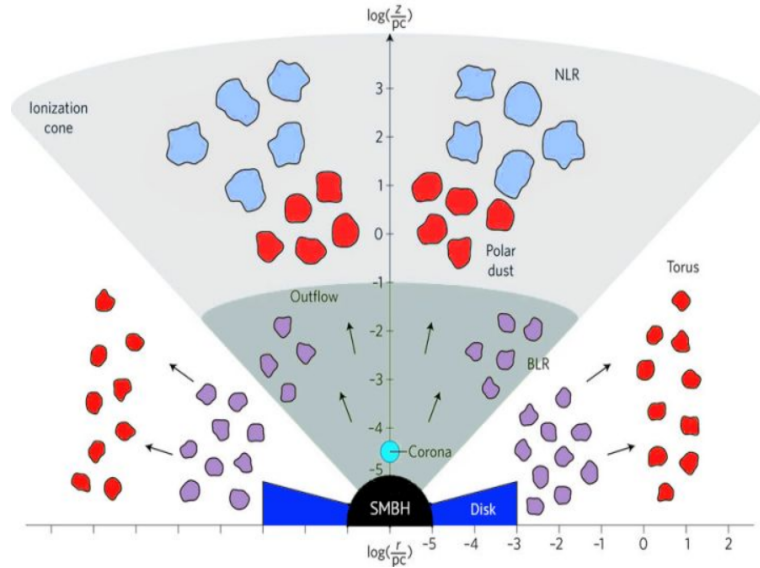


Figure 1.2: A diagram illustrating the structure of an AGN and relative components as a function of distance from the center (from Almeida et al. 2017).

1.2 AGN classification

The classification of AGN has undergone several revisions since the initial discovery of Seyfert galaxies (Seyfert 1943), and their recognition as non-stellar entities. Identifying a source as an AGN typically relies on satisfying one or more of the following criteria (Netzer 2013):

- It exhibits emission levels exceeding those expected from stellar processes within a compact nuclear region.
- Non-stellar continuum signatures are evident from its core.
- Its emission line spectrum indicates ionization processes not associated with stars.
- Variability is observed in both line and continuum emissions.

Once identified as an AGN, further classification into specific types necessitates consideration of various geometrical and physical parameters (Padovani 2017), including orientation (Antonucci 1993; Urry et al. 1995; Netzer 2015), accretion rate (Heckman et al. 2014), and the generation of jets from the central engine (Padovani 2016).

However, the classification process is not straightforward due to its dependence on the observing wavelength, leading to different classifications across various bands of the

electromagnetic spectrum. Additionally, obscuration poses challenges to accurately constraining the properties of AGN. In the following sections, the classification of AGN across different spectral bands is detailed.

1.2.1 Radio classification

A potentially highly effective method for obtaining an impartial view of both obscured and unobscured AGN is through radio observations. Unlike other wavelengths, at radio frequencies, where the emission is primarily from non-thermal processes like synchrotron radiation, the influence of extinction is minimal. Historically, AGN identified in radio surveys have been categorized into two primary groups:

- Radio-loud (RL) AGN: These are the most robust radio emitters, typically with luminosities exceeding 10^{24-25} W/Hz (Miller 1990, Yun et al. 2001). They often exhibit prominent extended radio emission, such as kiloparsec-scale relativistic jets and lobes.
- Radio-quiet (RQ) AGN: These are weaker radio emitters, with their radio emission concentrated in a compact, unresolved region (approximately less than 0.1 parsecs), often referred to as the “core.” This group constitutes the majority of AGN population, approximately 90% (Miller 1990, Stocke et al. 1992).

A popular method of classifying AGN uses the ratio of the radio (at 5 GHz), to optical (at 4400 Å), through the so-called radio-loudness parameter (R), typically set at R=10. This parameter is defined as the ratio of the monochromatic flux density in the radio and optical bands ($R = S_{rad}/S_{opt}$). This classification has been established in various studies (e.g., Kellermann et al. 1989, Laor 2000).

At high radio fluxes, AGN dominate the radio source population. However, at lower radio fluxes (in the sub-microjansky regime, μ Jy), a significant portion of the radio sources are attributed to star-forming galaxies (SFGs), becoming even more prevalent at fluxes below approximately 1 μ Jy (e.g., Seymour et al. 2008).

The non-thermal radio continuum observed in star-forming galaxies originates from synchrotron radiation emitted by cosmic ray electrons and positrons, accelerated by supernova remnants. These processes are prevalent in young stellar populations within star-forming regions (Condon 1992).

The observed radio emission in star-forming galaxies exhibits a tight correlation with emissions in the far-infrared (FIR) band (typically around 40-120 μ m), as both are products of star formation processes (Condon 1992, Yun et al. 2001, Helou et al. 1985). This correlation, initially observed in local star-forming galaxies and starbursts, has been confirmed to hold also at high redshifts (up to around $z \sim 2$, e.g. Ibar et al. 2008, Ivison et al. 2010, Mao et al. 2011).

Combining analyses in the FIR and radio bands provides a means to distinguish between SF galaxies and AGN. Despite the fact that even RQ-AGN adhere to the same FIR/radio correlation observed in SF galaxies (Padovani et al. 2011, Morić et al. 2010), the wide range of radio-loudness among AGN enables the identification of AGN through deviations from this expected correlation. These deviations are often termed “*radio-excess*” sources (Donley et al. 2005, Roy et al. 1997).

Fanaroff et al. 1974 defined sub-classes of radio galaxies as type I or II based on the distance between the highest surface brightness part of the lobes and the lowest surface brightness contour. If the ratio between these two quantities is less than 0.5, the radio galaxy is classified as FR I (with radio power at 1.4 GHz, $P_{1.4\text{GHz}} < 10^{24.5}$ W/Hz); if the ratio is > 0.5 , the source is classified as FR II (with radio power at 1.4 GHz, $P_{1.4\text{GHz}} > 10^{24.5}$ W/Hz). Morphologically, FR I galaxies exhibit a bright core and non-collimated jets leading to edge-darkened lobes, while FR II galaxies have one-sided collimated jets flowing into large, edge-brightened lobes. Furthermore, FR II and FR I galaxies also display differences in evidence of non-thermal nuclear activity in the optical band (Ledlow et al. 1996).

Another method for classifying radio-emitting AGN relies on the steepness of their spectrum, leading to the categorization into flat-spectrum and steep-spectrum radio sources. Flat-spectrum sources have spectral indices (α) lower than 0.5, while steep-spectrum sources have spectral indices higher than 0.5 ($S_\nu \propto \nu^{-\alpha}$) (Kimball et al. 2008). Flat-spectrum radio sources are typically compact and exhibit strong emission lines, whereas steep-spectrum sources tend to be extended and display weak emission lines.

Furthermore, AGN observed in the radio band can be classified based on the presence of excitation emission lines (Hine et al. 1979). If high-excitation lines are present, the source is classified as a High-Excitation Galaxy (HEG); if low-excitation lines dominate, the source is categorized as a Low-Excitation Galaxy (LEG). LEGs tend to exhibit redder optical colors and are characterized by inefficient accretion, while HEGs display more efficient accretion properties ($0.01 < L/L_{Edd} < 1$). It is noted that HEGs are often associated with FR II radio galaxies, while LEGs can be both FR I and FR II type radio galaxies.

A new category of radio galaxy, termed FR 0, was recently discovered (Baldi et al. 2015). These sources share properties similar to FR I galaxies but lack evidence for extended radio emission. The absence of prominent jets and lobes in FR 0 galaxies could be attributed to high-efficiency adiabatic loss or confinement of the jets within the corona region (Capetti et al. 2020).

1.2.2 Infrared classification

In the Infrared (IR) band, emission is primarily driven by the presence of dust in the circumnuclear region of AGN. Selection criteria typically rely on colors to distinguish mid-IR emitting AGN from stars or inactive galaxies (Padovani 2017), as AGN tend to

exhibit redder colors (Stern et al. 2005).

Major instruments utilized for characterizing large AGN samples in the mid-IR band include IRAS (Neugebauer et al. 1984), the Spitzer Space Telescope (Fazio et al. 2004; Werner et al. 2004), AKARI (e.g., Murakami et al. 2007), and WISE (Wright et al. 2010). However, because IR selection of AGN relies on dust emission, AGN lacking dust may be missed by these surveys.

IR observations have led to the discovery of various object types. For instance, Dust-Obscured Galaxies (DOGs, Dey et al. 2008), which are observationally characterized as faint in the optical and bright in the infrared, the final stage of galaxy mergers and are essential objects in the evolution of galaxies and AGNs, were identified using the Spitzer Space Telescope, employing colors between optical R-band and the MIPS 24 μm band. Additionally, a population of Extremely Red Quasars, candidate young objects in an early transition stage of massive galaxy evolution, was uncovered using WISE and SDSS data (Ross et al. 2015). Another class of IR-emitting AGN identified through WISE colors is represented by Hot Dust Obscured Galaxies (Hot DOGs, Eisenhardt et al. 2012), a population of hyper-luminous obscured quasars characterized by a high level of star formation.

1.2.3 Optical classification

The optical classification of AGN is based on the observation of emission lines in their spectra. These emission lines can be classified as narrow (with Full Width at Half Maximum (FWHM) approximately 500-1000 km/s) or broad (FWHM approximately 1500-15000 km/s). The presence of both narrow and broad lines indicates a nearly direct view of the nucleus, without interception by any absorbing medium. It is believed that narrow lines originate from the NLR and broad lines from BLR. Conversely, if only narrow lines are observed, it suggests that the line-of-sight (LOS) intercepting the obscuring torus, inhibiting the observation of the BLR.

Sources exhibiting both narrow and broad lines are termed Broad Line AGN or Type 1 AGN (or Seyfert 1 or quasar 1), with typically blue optical continuum (Big Blue Bump, emission from the accretion disc, see 1.4.3), while galaxies showing only narrow lines are classified as Narrow Line AGN or Type 2 AGN (or Seyfert 2 or quasar 2), commonly with a weak continuum because of the disc emission is largely suppressed by the extinction. This classification into Type 1 and 2 AGN applies across various bands, such as X-rays, and is closely associated with the Unified model, which will be discussed in the following section.

Another class in this band is that of LINERs (Low Ionization Nuclear Emission-Line galaxies), characterized by a weak continuum, the dominance of host-galaxy emission, and the presence of strong low-ionization emission lines in their spectra. LINERs can be classified into two main types: type-I, which exhibit broad emission lines, and type-II, which only display narrow emission lines (Laor 2003). Notably, some LINERs exhibit

point-like X-ray and UV sources, as well as variations in UV and X-ray emissions, although this characteristic is not universal across all LINERs (e.g. Maoz 2007).

Finally, lineless AGNs comprise a subgroup of active galactic nuclei characterized by exceedingly faint or entirely absent emission lines. They are identified by the presence of a non-stellar central source and occasionally exhibit continuum variability. This category encompasses two specific sub-groups: low-luminosity sources (Trump et al. 2009), and very high-luminosity sources (Shemmer et al. 2010, Meusinger et al. 2014).

1.3 The Unified model

The various classes of AGN described previously were initially perceived as distinct sources with unique properties. However, with increasing observations of these sources, leading to a better understanding of their physical characteristics, a unified model (Antonucci 1993; Urry et al. 1995) was developed. The primary objective of the unified model is to account for the observed differences among the diverse AGN population through considerations of orientation and accretion properties.

In this framework, an AGN is regarded as a galaxy having the properties described in section 1.1, which can be classified as described in section 1.2, contingent upon orientation effects and various forms of accretion.

Key advancements towards unifying the AGN population revolve around the role of the dusty torus, which re-emits absorbed optical/UV and soft X-ray radiation at infrared wavelengths, being responsible for the distinction between Type 1 and Type 2 AGN (Osterbrock 1978).

Additionally, the inclination angle plays a crucial role, resulting in radiation amplification (and superluminal motion) through Doppler boosting, as observed in Blazars (same as quasar but they have their jets directly pointed to Earth) and quasars when viewed almost face-on (Blandford and Rees 1978).

In Figure 1.3, the schematic representation of the AGN Unified Model is depicted. Notably, powerful active galaxies are classified as NLRG/BLRG (or Type II/I QSO) depending on whether the line-of-sight traverses the dusty torus. If the observer's view is aligned directly with the central engine through the jet (if it is present), the source is classified as a Blazar. Conversely, if the source displays low power, it is labeled as a FR I radio galaxy. Lastly, a source is assigned as a Sy1 or Sy2 based on its inclination angle.

1.4 AGN emission properties

AGN emission covers the entire electromagnetic spectrum, from the Radio band to the Gamma-rays. Each structural component contributes to the SED with distinct emission processes and within specific wavelength ranges. Figure 1.4 illustrates an example of an

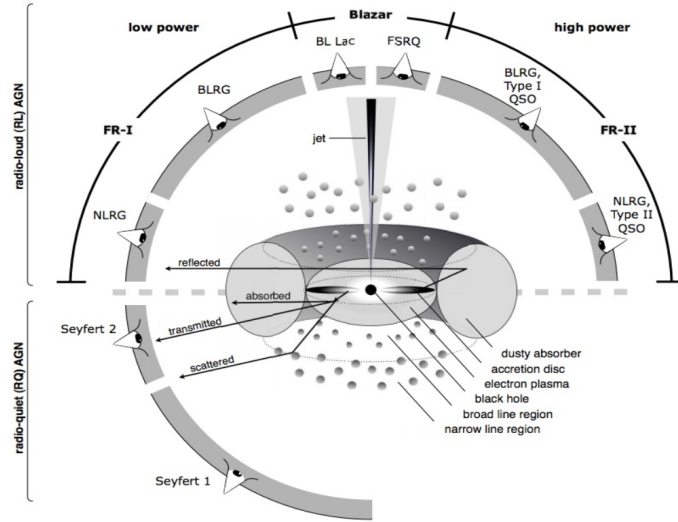


Figure 1.3: The AGN Unified Model shown. Various lines of sight and their corresponding classifications are depicted. The structure of Radio Loud (RL) AGN is illustrated at the top of the scheme, while Radio Quiet (RQ) AGN is represented below (from Beckmann et al. 2012).

unobscured AGN SED. At a basic level, the SED can be characterized by a triple hump, attributed to dust emission from the torus at Infrared wavelengths, thermal emission in the Ultraviolet from the disk, and thermal Comptonization plus reflection emission in X-rays.

In the subsequent sections, the processes and principal properties of AGN emission across various bands will be outlined, with particular emphasis on the X-ray emission component due to its pivotal role in this thesis.

1.4.1 Radio emission

The radio emission observed from AGN is primarily attributed to non-thermal synchrotron radiation. Both jetted and non-jetted AGN exhibit compact, point-like radio emission originating from the central nucleus. This emission typically follows a flat spectrum. In addition to this compact emission, jetted AGN also display extended emission from their jets and lobes, which typically exhibit a steeper spectrum.

When considering the population of electrons within the AGN, their energy distribution can often be described by a power-law function of the form

$$N(E)dE \propto E^{-\delta}dE \quad (1.10)$$

where $N(E)$ represents the number of electrons with energy between E and $E+dE$, α is the spectral index and $\delta=2\alpha+1$ is referred to the index of this energy distribution.

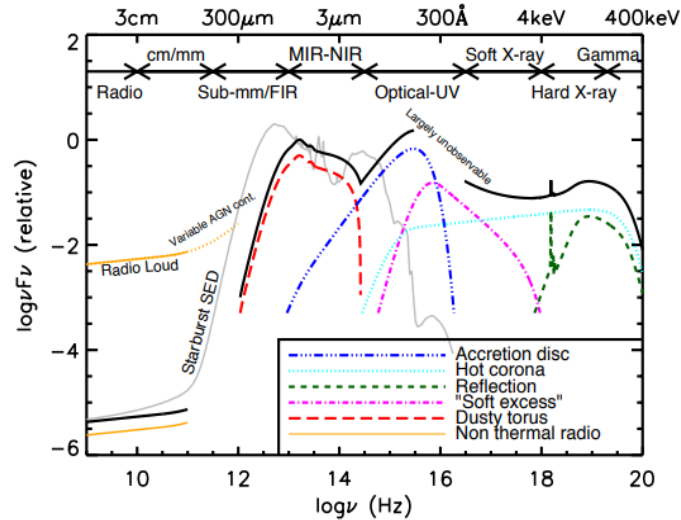


Figure 1.4: Schematic representation of the SED of an unobscured AGN with the main physical components separated into colored curves (from Harrison et al. 2014).

Synchrotron emission can be approximated by a power-law, with $F(\nu) \propto \nu^{-\alpha}$, with α the spectral index.

Despite its importance in characterizing AGN, radio emission typically contributes only modestly to the overall bolometric luminosity of these objects (Risaliti et al. 2004).

1.4.2 IR emission

The IR emission observed from AGN is primarily associated with circumnuclear dust. This dust, located within the obscuring torus surrounding the AGN central engine, absorbs ultraviolet (UV) and soft X-ray radiation emitted from the inner regions of the AGN. Subsequently, it re-emits this absorbed energy at longer wavelengths, typically peaking between 10 and 30 micrometers. The temperature of the dust typically ranges between 50 and 2000 Kelvin.

At lower frequencies, the efficiency of dust grey body emission decreases rapidly. Additionally, at shorter wavelengths, the dust can reach temperatures close to its sublimation point (approximately 1000 to 2000 Kelvin), resulting in a minimum in emission around 1 to 2 micrometers.

On average, the contribution of infrared emission to the total emission from an AGN is approximately 30% (Fadda et al. 2014). It is worth noting that in Radio Loud AGN, synchrotron emission can also contribute to the infrared emission other than thermal emission from the circumnuclear dust.

1.4.3 Optical-UV emission

In the optical and ultraviolet (UV) wavelength range, the dominant feature observed in the emission from active galactic nuclei (AGN) is known as the Big Blue Bump (BBB) (Malkan et al. 1982). The BBB typically spans wavelengths between approximately 30 to 300 nanometers. This spectral component is believed to originate from the accretion disk located in the central region of the AGN. The various temperatures present within the accretion disk lead to the emission of multiple black-body spectra, which when combined, contribute to the overall emission observed in the BBB (see 1.1.1).

Alongside the thermal continuum emission from the accretion disk, both emission and absorption features are commonly observed in the optical and UV spectra of AGN (e.g. Telfer et al. 2002, Berk et al. 2001). These features include both broad and narrow emission lines, which are distinct from those typically associated with stellar activity. By analyzing these spectral features, it becomes possible to estimate fundamental parameters of the AGN, such as its redshift and the mass of its SMBH.

1.4.4 γ -ray emission

Gamma-ray emission in AGN is predominantly observed in face-on sources, such as Blazars and BL Lacertae objects. This emission arises from the interaction between low-frequency synchrotron radiation emitted by relativistic electrons and these same electrons, through a process known as Inverse Compton scattering. This interaction, termed Synchrotron Self-Compton (SSC), results in a double-peaked broad-band spectrum, with emission observed both in the radio and gamma-ray bands.

The investigation of this phenomenon has led to the delineation of what is known as the Blazar sequence (e.g. Fossati et al. 1998, Donato et al. 2001), as shown in figure 1.5. The Blazar sequence describes a relationship between the properties of Blazars and their spectral characteristics.

Blazars can be classified into two main categories based on the energy at which their gamma-ray emission peaks. Sources with the gamma-ray emission peak at higher frequencies, typically ranging from around 50 MeV to 10 TeV, are termed High-frequency Blazars. Conversely, AGN where the gamma-ray peak occurs at lower energies, spanning approximately 100 MeV to 100 GeV, are referred to as Low-frequency Blazars.

1.4.5 X-ray emission

The X-ray emission observed from AGN typically ranges from approximately 0.1 keV, corresponding to the energy of the Galactic absorption cutoff (Risaliti et al. 2004), up to about 500 keV, which represents the cutoff energy of the emission itself (Dadina 2008).

The primary components of the X-ray emission from AGNs can be summarized as follows:

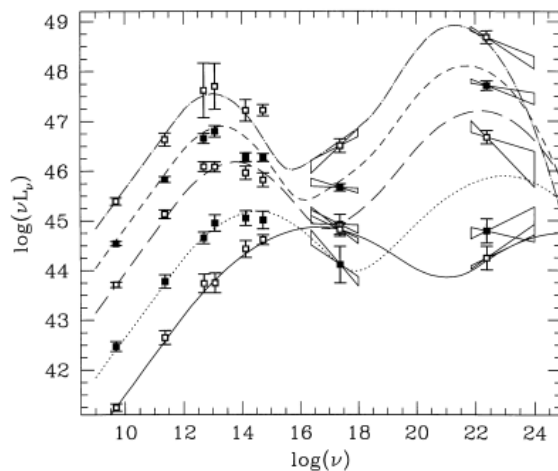


Figure 1.5: Blazar sequence. Different curves illustrate different luminosity AGN classes (from Fossati et al. 1998).

- Soft excess: This component is observed in the energy range of approximately 0.1 to 1 keV and is characterized by an excess of X-ray emission compared to what would be expected from the simple extrapolation of the hard power-law spectrum to soft X-rays.
- Comptonization emission: Extending from soft to hard X-rays, this component represents the main continuum emission and is typically described by a power-law function.
- Warm absorber component: This component arises from absorption features in the X-ray spectrum caused by intervening gas clouds along the line of sight to the observer.
- Reflection component: This component is due to the presence of the Compton Hump, a characteristic feature observed in the X-ray spectrum. It arises from the reflection of X-rays off dense material surrounding the central engine of the AGN.
- Fe $K\alpha$ fluorescent emission line: This is a prominent emission line observed at ~ 6.4 keV in the X-ray spectrum, originating from the fluorescence of neutral iron atoms in the accretion disk around the central supermassive black hole.

In Figure 1.6, a schematic representation of the X-ray spectrum is shown, illustrating the individual components described above. This schematic serves to visually convey the various spectral features observed in the X-ray emission from AGN.

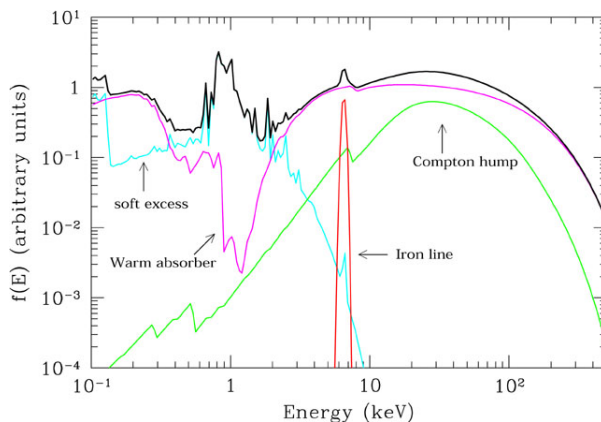


Figure 1.6: The total spectrum of a Type I AGN is represented as a black solid line. The individual components contributing to this spectrum are reported as colored solid lines: the main emission component and the warm absorber are shown in magenta, the soft excess is represented by a cyan line, the reflection component, including the Compton hump, is plotted in green and the Fe $K\alpha$ emission line is reported as a red line (from Risaliti et al. 2004).

Soft excess

The soft excess is a prominent feature observed in the spectra of almost all AGN, yet its origin remains a subject of debate within the astrophysical community. Initially, it was hypothesized to be associated with the high-energy tail of the thermal emission from the accretion disk (Czerny et al. 1987). However, subsequent studies have revealed problems with this interpretation: the observed temperatures and energies of the soft excess are much higher than what would be expected based on this thermal disk emission model (Gierlinski et al. 2004). Furthermore, attempts to resolve the soft excess into individual emission lines have largely been unsuccessful, indicating a continuum-like spectrum.

Done 2007 propose that the presence of a soft excess with a seemingly fixed temperature may be attributed to atomic processes, such as OVII/OVIII and Fe L shell absorption, which exhibit increased opacity around 1 keV. However, another plausible explanation suggested by Done is the presence of a reflection component contributing to the soft excess.

An alternative explanation for the soft excess is thermal Comptonization occurring within an optically thick corona with a temperature around 1 keV, as proposed by Petrucci et al. 2018. In this scenario, the soft excess arises from the thermal Comptonization of soft photons by hot electrons within the corona.

Comptonization emission

The primary X-ray emission from AGN can be approximated by a power-law spectrum extending from around 1 keV to approximately 300 keV. This emission is thought to arise from thermal Comptonization within the hot corona surrounding the AGN's central engine. The electrons within the hot corona have very high energies, corresponding to temperatures on the order of 10^8 - 10^9 Kelvin. These energetic electrons interact with optical/UV seed photons emitted by the accretion disk through multiple Inverse Compton scattering events, resulting in a spectrum composed of these up-scattered photons.

Typically, the photon index Γ of the power-law spectrum is in the range of 1.8 to 2, where $F(E) \propto E^{-\Gamma}$. This photon index describes the rate at which the intensity of the emitted X-rays decreases with increasing energy.

A debate exists regarding the dependence of the spectral index on redshift or luminosity, which could provide insights into whether there are variations in the properties of AGN central engines over cosmic time or with their emitting power. Such investigations aim at discerning any potential evolutionary trends or correlations between AGN properties and environmental factors, as background density or influence of other objects present in the neighborhood (Singh et al. 2023). The study of these dependencies is crucial for understanding the evolution and behavior of AGN populations across different epochs of the Universe.

Warm absorber

The warm absorber was initially identified by Halpern 1984 using data from the Einstein telescope. It is a notable absorption feature frequently observed in X-ray spectra of Seyfert 1 AGN, as documented by Maloney et al. 2000. Approximately 50% of Seyfert 1 galaxies exhibit these characteristics, as reported by Nandra et al. 1994. The warm absorber is believed to stem from absorption lines associated with warm ionized gas, with temperatures typically ranging between 10^4 and 10^5 Kelvin, and velocities spanning from 100 to 1000 kilometers per second. This gas is situated in the circumnuclear regions, as elucidated by studies such as those conducted by Kaspi et al. 2002 and Netzer 2002.

On the other hand, UFOs (Ultra Fast Outflows) constitute highly ionized and dense winds, with velocities denoted by v_{UFO} approximately equal to 0.1 times (or higher) the speed of light (c), originating from the innermost regions of the accretion disk. These outflows are observable in around 50% of both radio-loud and radio-quiet AGN, suggesting that the jet related radio-quiet/radio-loud AGN dichotomy might not hold for AGN winds (Tombesi et al. 2014). Additionally, investigations into the variation of ionization parameters relative to the distance from the SMBH, as undertaken by Tombesi et al. 2013, have indicated that both warm absorbers and UFOs may arise from the same outflowing wind. The distinction lies in their velocities, which are contingent upon the distance from the central black hole.

Reflection component

The reflection component arises from the interaction, primarily Compton scattering, of emission photons with ionized gas present in the accretion disk. In figure 1.6, the reflection component is shown as a solid green line. The continuum spectrum, resulting from electron scattering with the reflection component, exhibits a prominent peak around 30 keV and a notable drop in energy between 4 and 5 keV. This decrease is attributable to the photoelectric absorption of radiation at lower energies. For a Compton-thick reflector, the efficiency of reflection typically falls within the range of a few percent to around 30% at the peak (Ghisellini et al. 1994). Conversely, in the case of a Compton-thin reflector, the efficiency is notably lower.

Iron fluorescence emission line

In several AGN, an emission feature is consistently observed at around 6.4 keV. This emission line corresponds to the neutral Fe $K\alpha$ fluorescent line, which is a combination of $K\alpha_1$ and $K\alpha_2$ transitions. The precise region responsible for generating the iron line is still a subject of debate. However, the presence of a narrow component in the line profile suggests its production within a cold medium rather than in a region very close to the SMBH. On the other hand, a broad, gravitationally distorted iron line may be produced in the vicinity of the SMBH, such as the accretion disk, as proposed by studies like Fabian 2000.

The Fe $K\alpha$ line is generated through the fluorescence process: when the radiation field's energy surpasses the K-edge threshold ($E = 7.1$ keV), a K-shell electron is ejected. This can lead to either an Auger decay or the emission of a fluorescent line. The probability of fluorescent emission occurring is determined by the fluorescence yield, denoted as $Y = Z^4 / (Z^4 + 33^4)$, where Z represents the atomic number. Additionally, the effect is more pronounced for high atomic number (Z) elements due to their higher cross-section, which scales approximately as $Z^{4.5}E^{-3.5}$. Therefore, iron, being abundant and having a high atomic number, is particularly favored by this process.

In some instances, there is also the $K\beta$ line at 7.06 keV, and the nickel $K\alpha$ line at 7.5 keV is expected.

Chapter 2

The SoSimple project

2.1 The presence of AGN in interacting galaxies

The second law of thermodynamics asserts that in a closed system, the total entropy either increases or remains constant over time. In the context of astrophysics, such as in spiral galaxies, where stars exhibit ordered orbits, this law suggests a tendency for systems to move from ordered states towards more randomized or relaxed states. However, this transition typically requires the introduction or presence of some form of instability.

The study of galaxy evolution delves into understanding how galaxies undergo this transition from ordered to more relaxed motion. One plausible mechanism for introducing instability is the close interaction between galaxies. When two galaxies come into close proximity, their gravitational fields start to influence each other. This gravitational perturbation can disrupt the conservation of angular momentum of objects in ordered orbits, leading to the funneling of gas and dust towards the central regions of the galaxies.

The sudden inflow of material into the central region can then trigger various processes. For instance, it may initiate the accretion of material onto the central SMBH, causing it to grow in mass. Additionally, this inflow of material can lead to a phase of intense star formation, commonly referred to as a starburst phase, occurring around the nucleus of the galaxy. These events typically unfold within the inner pc to kpc scales at the center of the galaxy.

Figure 2.1 illustrates the progressive stages of interaction between two galaxies, modeled after the anticipated interaction between Abell 901 and Abell 902. This montage amalgamates images sourced from various observations capturing different stages of the interaction process. The six stages depicted in the montage are succinctly described as follows:

- In the initial stages, distinct galactic structures can still be discerned, with tidal forces beginning to stretch and distort the shapes of the galaxies as they approach

each other. As the merger progresses, the galaxies become increasingly entangled, their shapes morphing and merging into a complex network of stars, gas, and dust.

- During the peak of the merger, the galaxies appear as overlapping or intertwined structures, with bridges of material connecting them. Intense star formation may be triggered in these regions of overlap, as gas and dust are compressed and ignited by the gravitational forces at play.
- In the later stages, the merger remnant begins to settle into a more relaxed state, resembling a single, larger galaxy with features reminiscent of its progenitors. Tidal tails and shells of stars may still be visible, bearing witness to the violent history of the merger.
- Ultimately, the merger process reshapes the involved galaxies, leading to the formation of new stellar populations and potentially fueling the growth of central supermassive black holes.

Through these stages, mergers play a crucial role in the evolution of galaxies, driving changes in their morphology, star formation rates, and overall structure.

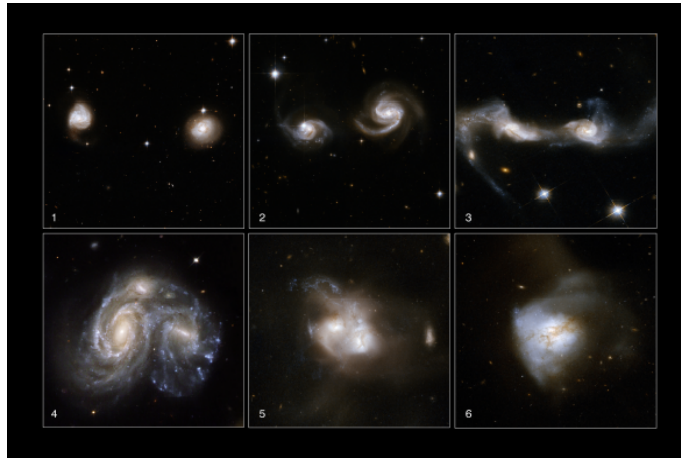


Figure 2.1: The images indicate various galaxies in different stages to replicate the merger between galaxies Abell 901 and Abell 902, captured by the Hubble Space Telescope in the optical band with filters ACS/WFC: F606W (V). Each stage offers a glimpse into the intricate dance of gravitational interaction between these galaxies as they merge over cosmic timescales. Image credit: NASA, ESA, the Hubble Heritage Team (STScI/AURA)-ESA/Hubble Collaboration and A. Evans (University of Virginia, Charlottesville/NRAO/Stony Brook University), K. Noll (STScI), and J. Westphal (Caltech).

The violent effects observed in the interactions of two equally massive, gas-rich galaxies are known as major mergers. These mergers typically involve galaxies with a mass ratio ranging from 1:1 to 1:3 (Lotz et al. 2010). Conversely, if one of the interacting galaxies has lower mass, resulting in a mass ratio higher than 1:3, the interaction is classified as a minor merger. While minor mergers typically preserve the spiral structure of the more massive galaxy, they stimulate significant gas inflows and induce star formation (e.g., Kaviraj 2014). It is worth noting that minor mergers might be more prevalent than major mergers (e.g., Lin et al. 2004, Stewart et al. 2008, Jogee et al. 2009).

The gas content of the progenitor galaxies is a critical factor influencing the evolution of the interaction. In gas-rich interactions, termed wet mergers, abundant gas reservoirs facilitate substantial star formation and accretion (e.g., Nikolic et al. 2004, Hopkins et al. 2006, Lin et al. 2008). Conversely, in gas-poor interactions, termed dry mergers, the lack of gas inhibits widespread star formation. Although dry mergers do not significantly alter the star formation rates of galaxies, they play a crucial role in the growth of stellar mass in massive red galaxies in the present epoch (e.g., Tran et al. 2005, Faber et al. 2007, Lin et al. 2008).

2.1.1 Detecting AGN activity in interacting/merging galaxies

The activation of AGN activity during galaxy mergers has been thoroughly investigated through both observational and theoretical approaches. Various observational techniques, spanning across different wavelengths and numerical methodologies, have been employed. These methodologies offer complementary insights as each has its inherent limitations (De Rosa et al. 2019).

Multiple strategies have been devised to pinpoint potential dual and binary AGN candidates. The identification of AGN candidates and pairs with separations ranging from parsecs to kiloparsecs has primarily relied on extensive surveys across optical, radio, mid-infrared, and hard X-ray bands. Additionally, targeted observations, particularly in the high-energy domain, have contributed significantly to this endeavor.

However, the identification of dual AGN systems remains challenging, and most detections have occurred serendipitously. A significant hurdle in these studies is the necessity for a statistically robust sample of dual and multiple AGN, spanning a wide range of spatial separations. Despite the discovery of numerous AGN pair candidates and merging galaxies in recent years, only a limited fraction have been confirmed, typically following intensive and observationally demanding multiband follow-up efforts.

For instance, the use of SDSS optical spectral data has facilitated the identification of dual AGN through the presence of doubled-peaked [O III] lines. However, merely about 2 percent of these candidates are ultimately confirmed through multi-wavelength follow-up observations (De Rosa et al. 2019). This low confirmation rate is attributed to the non-uniqueness of the doubled-peaked profile as a signature of dual AGN, as other phenomena, such as matter outflows from a single AGN, can produce similar spectral

features.

Similar challenges arise in observations at other frequencies. For instance, relying solely on radio data may pose difficulties in distinguishing AGN from star formation processes in radio-emitting regions. Moreover, the detection of X-ray emission associated with a source does not definitively indicate the presence of an active nucleus, as X-ray emission can also originate from star-forming galaxies and weakly accreting black holes, such as LINERs and AGN with inefficient accretion disks.

Furthermore, mid-infrared all-sky surveys can identify obscured systems, complementing optical AGN searches. In essence, the most effective observational strategy involves initially identifying promising candidates, followed by confirmation through appropriate follow-up programs. Each wavelength band contributes uniquely to this pursuit, aiding in the eventual detection and confirmation of AGN.

Simulations

Numerical simulations contribute significantly to our understanding of galaxy mergers and the emergence of multiple AGN systems. There are two primary avenues of research in this domain: cosmological simulations and isolated simulations of mergers.

Cosmological simulations enable the generation of galaxy mergers and multiple AGN systems, offering a crucial complement to observational studies (Steinborn et al. 2016). These simulations allow for the quantification of the dual AGN fraction relative to single AGN (Volonteri et al. 2022, Sharma et al. 2023). While a variety of hydrodynamic cosmological simulations exist, only a limited number of them are capable of resolving AGN pairs with separations down to kiloparsec scales due to the computational expense of combining large volumes with high resolution.

Conversely, idealized merger simulations can resolve sub-kiloparsec scales, which is essential for tracking the dynamics of SMBHs during mergers (Van Wassenhove et al. 2012, Blecha et al. 2013). However, simulations of isolated galaxy mergers cannot directly predict the fraction of AGN pairs among the total population of AGN. Instead, it is possible to compute an activity-dual time normalized to the duration when at least one black hole is active, providing insights into the temporal behavior of AGN activity during mergers (Capelo et al. 2017).

2.1.2 X-ray observations of dual AGN

The detection of spatially-resolved dual AGN, with projected separations of a few tens of kpc, has been notably observed in optical and mid-infrared surveys, particularly through data from the Sloan Digital Sky Survey (SDSS) (York et al. 2000, Abazajian et al. 2009), the Baryonic Oscillation Spectroscopic Survey (BOSS) (Ahn et al. 2012), and the Wide-field Infrared Survey Explorer (WISE) (Wright et al. 2010). This reinforces the notion

that gas-rich mergers may serve as triggers for the active nuclear phase in both galaxies (e.g., Foreman et al. 2009, Weston et al. 2017).

Bright AGN pairs with separations of less than a few hundred kpc represent excellent probes for investigating both the small-scale (less than approximately 100 kpc) structure of the IGM and the large-scale (on the order of Mpc) rich environment where mergers are more likely to occur (e.g., Djorgovski et al. 2007, Farina et al. 2013, Lusso et al. 2018).

The high penetrative power of hard X-rays serves as a unique and often indispensable tool in the quest for multiple active nuclei within a galaxy. Hard X-ray observations are less susceptible to contamination from stellar processes and absorption, although they are still limited by spatial resolution limitations. Indeed, it was X-ray imaging spectroscopy that initially led to the identification of the first pair of accreting SMBHs in the galaxy NGC 6240 (Komossa et al. 2002).

A large, point-like luminosity exceeding approximately 10^{42} erg/s is most likely attributed to an AGN than to a starburst and/or emission from low-mass X-ray binaries (Fragos et al. 2013, Lehmer et al. 2016). However, in many cases, both a nuclear and an extended component can contribute to the X-ray spectrum of a dual system. This necessitates high spatial resolution and low background levels to accurately discern the weak AGN emission from any diffuse component.

Ultimately, X-ray observations serve as an efficient means to detect accretion-powered processes in low-to-moderately obscured sources. While heavy obscuration may hinder a comprehensive census of the AGN population, deep exposures, combined with comprehensive hard X-ray coverage, have the potential to alleviate this issue.

The observed effect of interactions on AGN activity at $z \sim 0$

The influence of galaxy interactions and mergers on AGN activity has been extensively observed in the nearby universe. For instance, Ellison et al. 2013 conducted analyses on interaction-induced AGN enhancement using observations from SDSS. They examined a spectroscopic galaxy pair sample with a stellar mass ratio of less than 4, a visually identified post-merger sample, and corresponding mass and redshift-matched samples of isolated (control) galaxies. The classification of optical AGN in their samples was performed using the BPT diagram. BPT stands for Baldwin, Phillips, and Terlevich (Baldwin et al. 1981), who first introduced this diagnostic diagram in 1981.

Their findings, illustrated in 2.2, demonstrate a clear trend of increasing AGN excess (the ratio of AGN fraction in paired galaxies compared to the controls) with decreasing projected separation, particularly for separations below 40 kpc. The most substantial enhancement, approximately 2.5 times larger than controls, was observed at the closest projected separations (less than 5 kpc). Numerous studies in the nearby universe have corroborated similar results, indicating a significant enhancement of AGN activity in galaxy pairs (e.g., Woods et al. 2007, Satyapal et al. 2014).

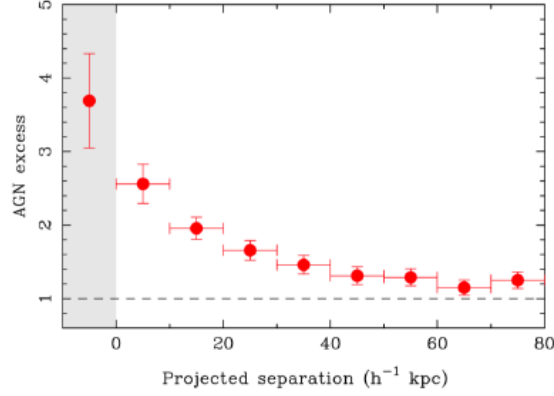


Figure 2.2: The plot illustrates the AGN excess, defined as the ratio of the AGN fraction in galaxy pairs to that of the control sample, as a function of projected separation. The filled points represent observations from SDSS galaxy pairs. The gray box highlights the enhancement observed in their post-merger sample. From Ellison et al. 2013.

Another example on this type of study is given by Koss et al. 2012, who studied the fraction of dual AGN in a sample of nearby ($z < 0.05$) selected AGN from the all-sky Swift BAT survey. In the 14-195 keV band, combining Chandra and Gemini observations along with optical and X-ray observations, they find that the dual AGN frequency at scales < 100 kpc is 10%.

2.2 The SoSimple observing program

Galaxy mergers arise as a direct consequence of the hierarchical growth of dark matter halos in the favored Λ CDM cosmological model. These mergers, observed across all redshifts, present a spectacle of varied and intricate shapes that captivate scientists and the public alike.

As described in section 2.1, these interactions represent some of the most violent and transformative events they experience. During these encounters:

- Tidal forces tug gas and stars into different orbits.
- Gas compression can fuel intensified star formation.
- Central SMBHs may more efficiently accrete matter, leading to AGN.
- Star formation may subsequently dwindle due to rapid gas consumption or feedback from stars or AGN.

- The SMBHs of the merging galaxies can eventually coalesce, emitting gravitational waves.
- Tidal debris gives rise to tidal dwarf galaxies and super star clusters. The system may ultimately evolve into a massive elliptical galaxy, with star formation halting rapidly.

These processes collectively illustrate the dynamic and transformative nature of galactic mergers, shaping the cosmic landscape over cosmic time.

Observationally, these processes have been extensively studied using large spectroscopic samples from surveys like the SDSS, as well as detailed multi-wavelength mapping of select individual galaxies. Hydrodynamical simulations offer predictions on the time evolution of galaxy properties across different merger configurations. However, these simulations rely on sub-grid physical models.

Therefore, it is crucial to systematically compare the predictions of these simulations with observational data. This comparison allows for the refinement of the underlying physical models, ensuring they accurately capture the complex dynamics of galaxy mergers.

In this regard, integral field unit (IFU) spectroscopy has emerged as an effective method for mapping the physical properties of galaxies. Past and ongoing IFU surveys such as CALIFA (Sánchez et al. 2012), MaNGA (Bundy et al. 2015), and SAMI (Konstantopoulos et al. 2013) have provided optical IFU data for extensive galaxy samples. However, these surveys often lack sufficient coverage of merging galaxies and suffer from limitations such as small field of view (FoV) and poor spatial resolution.

The sensitivity and expansive FoV of instruments like MUSE offer a distinct opportunity to systematically characterize nearby interacting galaxies. With MUSE, researchers can comprehensively study the dynamics and properties of merging systems, shedding light on the intricate processes involved in galaxy interactions.

The Snapshot Optical Spectroscopic Imaging of Mergers and Pairs for Legacy Exploration (SoSimple, PI: B. Husemann) is a major public filler-time proposal employing the MUSE instrument at VLT. The program targets a broad sample of over 150 interacting galaxies in the southern hemisphere ($\delta < 20^\circ$), sourced primarily from the Arp (Arp et al. 1987) and Arp-Madore catalogs. These catalogs, despite their age, remain invaluable for studying nearby interacting galaxies ($0.01 < z < 0.05$) due to their rich archival data and well-characterized morphological features. By definition, this sample is free from any bias toward the presence of AGN, as it is selected solely based on the morphological properties of interacting galaxies, without criteria related to their nuclear activity.

Many of these galaxies have been previously observed with the HST or are part of an ongoing large-scale HST filler-gap program (PI: J. Dalcanton). This extensive dataset allows for a comprehensive multi-wavelength study of galaxy interactions, providing an

unprecedented opportunity to examine the role of mergers in triggering star formation, AGN activity, and gas redistribution processes.

While more recent merger catalogs, such as those derived from the SDSS Galaxy Zoo, offer larger samples, they typically feature higher median redshifts, requiring deeper observations with superior seeing conditions to achieve comparable spatial resolution. Moreover, many SDSS-based merger catalogs lack the high-resolution HST imaging available for the Arp and Arp-Madore galaxies, further highlighting the unique advantages of the SoSimple target selection.

Complementary to the optical observations, a follow-up Swift/XRT X-ray survey (Swift Observations of Merging and Interacting Galaxy Pairs, PI: A. De Rosa, INAF/IAPS) has been initiated to confirm potential nuclear activity within these interacting galaxies. The combination of optical, X-ray, and multi-wavelength data enhances our understanding of the dynamic processes at play during galactic mergers and their impact on SMBH evolution.

2.2.1 Scientific Objectives of SoSimple

The extensive dataset collected by SoSimple enables a variety of scientific investigations. The primary objectives of the program include:

- **Investigating SMBH Accretion Events During Mergers:** Major mergers are expected to result in binary SMBH systems. However, direct observation of SMBHs is challenging unless they accrete material and appear as AGN. AGN activity is often enhanced during mergers (Darg et al. 2010), but its detection can be obscured due to dust and gas (Almeida et al. 2017) or stochastic variability (Schawinski et al. 2015, McElroy et al. 2016). For example, a study based on IllustrisTNG simulations found that, on average, post-merger galaxies exhibit SMBH accretion rates approximately 1.7 times higher than isolated galaxies, with an increased probability of hosting luminous AGN by a factor of 3-4. Observing dual AGN signatures still remains difficult, as simultaneous AGN activity in both SMBHs is uncommon (Steinborn et al. 2016, De Rosa et al. 2019).
- **Characterizing Star Formation Dynamics:** Close galaxy pairs and interacting systems exhibit elevated star formation rates (Ellison et al. 2008, Davies et al. 2015). The starburst activity is generally concentrated in galaxy centers and diminishes at post-coalescence (Schawinski et al. 2014). Observations of localized starbursts within mergers provide insight into the temporal and spatial evolution of star formation. A large sample of interacting galaxies is required to analyze gas-disc re-growth, star formation suppression, and spatial variations in these processes (Ellison et al. 2018).

- **Mapping Large-Scale Gas Flows Using Metallicity Gradients:** Galactic interactions facilitate significant gas redistribution, influencing metallicity gradients across the system. Observations show that relaxed disk galaxies exhibit characteristic negative metallicity gradients (Sánchez et al. 2014), while mergers often display flattened or inverted gradients, indicative of metal dilution due to inflowing gas (Kewley et al. 2010, Rich et al. 2012). Understanding these processes requires detailed spectroscopic mapping.
- **Studying Gas and Stellar Kinematics:** The MUSE instrument enables detailed extraction of gas and stellar velocity fields, which encode critical information about the angular momentum and orbital dynamics of merging galaxies. Comparing stellar and gas kinematics can reveal misalignments and insights into merger histories (Barrera-Ballesteros et al. 2015).

A good example of the importance of multi-wavelength observations, in particular in X-rays, in determining the dual AGN fraction among galaxies is the work of De Rosa et al. 2023 (though not based on the SoSIMPLE catalog of sources). This study examines optically selected dual AGN with separations between 3 and 97 kpc using multi-wavelength data (optical, X-rays, mid-IR) to characterize their intrinsic properties and compare them with isolated AGN. Out of 124 X-ray detected AGN candidates, 52 were in pairs and 72 were single sources.

More than 80% of the AGN in pairs were confirmed through multi-wavelength analysis. X-ray spectral analysis showed that AGN luminosity increases as separation decreases, indicating that mergers may trigger more luminous AGN. Approximately 80% of the AGN are Compton-thin, while 16% are Compton-thick, with these obscured fractions being higher than in isolated AGN.

The difference between Compton-thin and Compton-thick AGN is based on the amount of obscuring gas and its effect on X-ray radiation:

- In Compton-thin AGN, the column density ranges between 10^{22} and 10^{24} cm^{-2} . X-rays can partially pass through, with soft X-rays below 10 keV being absorbed, while hard X-rays above 10 keV remain detectable.
- In Compton-thick AGN, the column density is much higher, exceeding 1.5×10^{24} cm^{-2} . This dense gas blocks even hard X-rays, making direct detection difficult. These AGN are often identified through infrared emission and a strong Fe K α line at 6.4 keV.

The trend of higher obscuration in AGN pairs was further supported by comparing de-reddened [O III] emission with observed X-ray luminosity. The fraction of Compton-thick sources in early merging stages is lower than in later stages. Comparing N_{H} from X-rays with E(B-V) from Narrow Line Regions suggests the absorbing material is likely associated with the torus or Broad Line Regions.

The study also found that X-ray data, when observed under optimal conditions, are highly effective in confirming and studying dual-AGN systems.

2.3 The aim of my thesis

The primary goal of my thesis is to investigate the AGN content using an expanded catalog of interacting galaxies. Specifically, the research focuses on selecting SoSIMPLE sources from the HST program that have X-ray observations from the Chandra, XMM-Newton, and NuSTAR telescopes, either as primary targets or as serendipitous detections within the observational fields. These X-ray datasets are critical for identifying AGN, as hard X-rays penetrate obscuring material more effectively than optical or infrared observations, providing a less biased view of nuclear activity.

A key aspect of this study is assessing the incidence of AGN in an unbiased sample of interacting galaxies across different merger stages, characterized by varying levels of galaxy separation. By analyzing AGN fractions as a function of pair distance, this work would like explore how merger dynamics influence nuclear activity and whether close interactions preferentially trigger AGN compared to widely separated pairs. This approach allows for a direct investigation of the AGN-merger connection without pre-selecting sources based on AGN-related criteria, ensuring that the study remains free from biases toward already known active nuclei.

To contextualize these findings, the AGN occurrence in interacting galaxies should be compared, in the end, with a control sample of isolated galaxies with similar redshift and stellar mass distributions. This control sample will be drawn from large-scale surveys such as the SDSS, ensuring a statistically meaningful comparison between galaxies undergoing interactions and those evolving in relative isolation. Such a comparative analysis will help disentangle the role of mergers in triggering AGN, distinguishing interaction-driven nuclear activity from that arising in secularly evolving galaxies.

In particular, the primary focus of my study was to identify the potential presence of AGN in the X-ray band through a detailed spectral analysis of the sources in the sample. The X-ray properties derived in this study—such as spectral index (Γ), column density (N_{H}), and X-ray luminosity (L_X)—will serve as first-order indicators for classifying these galaxies in terms of AGN activity. Distinctive features of AGN, including high point-like luminosity, power-law spectral continua, and strong Fe line emissions, will be used to differentiate AGN from starburst-driven emission. Additionally, this work will explore the fraction of obscured versus unobscured AGN across different merger stages, providing insights into how interactions influence AGN obscuration and fueling mechanisms.

Furthermore, the research will integrate optical spectroscopy from MUSE to conduct a multi-wavelength comparative analysis of interacting galaxies. In my work, a preliminary investigation of the optical analysis using MUSE spectra has been started. The first step of this analysis has been initiated by visually inspecting the optical spectra,

focusing on the presence and relative strength of key emission lines as well as the shape of the continuum. The spectra have been extracted from a region spanning 1–3 arcseconds around the core of each galaxy, ensuring that the nuclear properties are well sampled while minimizing contamination from extended star-forming regions. This initial examination provides a starting foundation for classifying galaxies based on their dominant ionization mechanism and nuclear activity.

Optical spectra offer crucial diagnostics for distinguishing AGN from star-forming galaxies, with the continuum shape playing a key role. A red continuum may indicate an older stellar population, the possibility that the accretion disk is completely extinted, i.e. the presence of a heavily absorbed AGN, whereas a blue continuum is typically associated with active star formation or unobscured AGN emission. By systematically analyzing these spectral features, we can identify potential AGN candidates and assess the impact of interactions on nuclear activity.

In addition to continuum characteristics, the possibility of using carefully MUSE spectroscopic data in the future for a more detailed analysis, particularly in examining the emission lines present in the spectra, such as [OIII] λ 5007, H β , [NII] λ 6584, H α , and [SII] λ 6717,6731. These lines are fundamental for applying classical diagnostic tools, such as the BPT diagram, to separate AGN-driven ionization from star formation. Specifically, a high [OIII]/H β ratio combined with an elevated [NII]/H α ratio is a strong indicator of AGN activity, while lower values suggest ionization dominated by young stellar populations.

By integrating these spectral diagnostics with the X-ray properties derived in this study, a more careful and specific identification of potential AGN classification framework within interacting galaxies could be made. Moreover, the spatially resolved nature of MUSE data will enable the investigation of ionized gas kinematics, potentially revealing outflows, shocks, or dual AGN signatures that may emerge due to galaxy interactions. This multi-wavelength approach will offer a more comprehensive understanding of how mergers influence nuclear activity and the physical conditions of the surrounding interstellar medium.

2.4 X-ray data in SoSimple

Starting with the catalog of Arp and Arp-Madore sources observed by HST, the first step involved cross-matching these galaxies with the MUSE archive to identify targets with available integral field spectroscopic data. This search yielded 63 targets with HST and MUSE coverage.

Next, these targets were cross-correlated with the archives of the Chandra, XMM-Newton, and NuSTAR X-ray telescopes to determine the availability of X-ray observations. This search identified 11 targets with high-energy data, forming the sample for this thesis research. Data from the Swift telescope were also available; however, the focus

was primarily on those from Chandra, XMM, and NuSTAR, especially due to the higher sensitivity of Chandra and XMM compared to Swift.

Some of these galaxies have observations from multiple X-ray missions, providing an opportunity for spectral comparisons across different energy bands and exposure depths. Details regarding the observational parameters and individual sources are provided in Appendix A.

Below is a table summarizing the 11 Arp and Arp-Madore sources that were analyzed in X-rays along with their corresponding targets composing these systems.

The sample		
Target	Components	Redshift
AM 0018-485	NGC 0092, NGC 0089, NGC 0088, NGC 0087	0.011
AM 0642-801		0.016
ARP 100	IC 0018, IC 0019	0.020
ARP 200	NGC 1134 (Arp 200), IC 0267	0.012
ARP 245	NGC 2992, NGC 2993	0.007
ARP 255	UGC 05304(ned01), UGC 05304(ned02)	0.040
AM 0519-611	ESO119-IG054, ESO119-IG055	0.016
ARP 303	IC 0563, IC 0564	0.022
AM 2133-384	ESO343-IG013	0.019
AM 2026-424	ESO285-G019 (west and east)	0.050
AM 2048-571	IC 5063	0.011

Table 2.1: List of the 11 interacting galaxy systems included in the sample. The “Target” column lists the system names, while the “Components” column provides the individual galaxies within each system when multiple components are present. For systems where only one galaxy is listed, the target name corresponds to an alternative designation from the Arp and Arp-Madore catalogs.

Chapter 3

X-ray telescopes and data reduction

This chapter will describe the basic properties of X-ray telescopes, then focus more on those used for observations relevant to the thesis work. Subsequently, a concise presentation of the data reduction procedure conducted to analyze the data for each telescope will be provided.

3.1 X-ray telescopes

Due to the Earth’s atmosphere being opaque to high-energy radiation, X-ray telescopes must be positioned in orbit outside the atmosphere. A pivotal advancement in X-ray astronomy has been achieved through the implementation of focusing optics. These optics play a crucial role in discerning a specific source from the surrounding background and other nearby sources. They also enable the detailed study of morphological properties and facilitate reaching lower flux limits. However, a significant challenge arises in the fact that X-rays can easily penetrate through reflective materials. To overcome this problem, it becomes essential to employ reflections with low angles and materials of appropriate density. The critical angle, defined as the angle above which a photon will not be reflected (but rather refracted according to Snell’s law), is dependent on both the material density and the photon energy. The critical angle (θ_c) is proportional to the square root of the material density (ρ) divided by the photon energy (E_{ph}):

$$\theta_c = \frac{\sqrt{\rho}}{E_{ph}} \quad (3.1)$$

Materials with higher densities allow for higher critical angles, offering improved performance in X-ray focusing, but the requirement for launching into space necessitates that they cannot be too heavy, otherwise, excessive weight would become an issue.

In X-ray telescopes, the technique known as “double grazing incident reflection” is utilized to improve the collection efficiency of X-ray light and spatial resolution. This

method involves two reflective surfaces working together to focus X-rays.

First, incoming X-rays strike the first reflective surface at a very shallow angle, causing nearly total reflection and directing them towards the telescope’s focal point. Then, these reflected X-rays are redirected towards a second reflective surface, positioned to receive the X-rays from the first surface. The second surface reflects X-rays again, further directing them towards the telescope’s focal point. This double grazing incident reflection enables better collection of X-ray light and enhances the telescope’s spatial resolution.

In summary, the implementation of double grazing incident reflection in X-ray telescopes maximizes light collection and improves the telescope’s ability to distinguish fine details in high-resolution images.

One of the most prevalent optical configurations is attributed to Wolter (1952), who introduced three distinct configurations for X-ray optics known as Wolter I, II, and III. The first two configurations are based on parabolic and hyperbolic mirrors, while the third configuration, although not widely utilized, involves parabolic and ellipsoidal reflections. The most commonly used configuration in X-ray telescopes is the Wolter I.

3.1.1 The Effective Area

A key parameter characterizing X-ray telescopes is the effective area, representing the instrument’s capability to collect photons. The effective area (A_{eff}) is determined by the product of several factors:

$$A_{eff}(E, \theta, x, y) = A_{geom} \cdot R(E) \cdot V(E, \theta) \cdot Q(E, x, y) \quad [cm^2] \quad (3.2)$$

The different parameters contributing to the effective area are as follows:

- A_{geom} is the geometric area, referring to the cross-sectional area of the telescope or the transverse section of the mirror assembly, i.e., the area visible to the incoming photons.
- $R(E)$ is the reflectivity, representing the fraction of photons reflected by the mirrors based on their energy.
- $V(E, \theta)$ denotes vignetting, representing the fraction of leaked photons as a function of their energy and off-axis angle θ . The vignetting is associated with the focusing process of X-ray photons through double grazing incidence.
- $QE(E, x, y)$ represents quantum efficiency, i.e. the fraction of incident photons registered by the detector based on their energy and position (x,y) on the detector.

The effects of vignetting become more pronounced at larger distances from the axis and at higher energies. In such cases, as photons move away from the pointing axis, the source becomes “less exposed”. The effective area is critical, because it is used in the

analysis of X-ray data, as shown in section 3.7 when the Ancillary Response File (ARF) is introduced.

3.1.2 Angular and spectral resolution

The distribution of light from a point-like source on a detector is characterized by the Point Spread Function (PSF). In the realm of X-rays, the PSF's features are contingent upon both the incident photon energy and the off-axis angle. Notably, it exhibits heightened sharpness in the central region of the detector, progressively broadening moving at off-axis positions. Often, when dealing with X-ray spatial resolution, the term Half Energy Width (HEW) is used. The HEW indicates the width of the region encompassing half of the photons emitted by the point source. An alternative way for quantifying angular resolution is the Encircled Energy Fraction (EEF), a numerical measure that quantifies the proportion of the total energy or flux enclosed within a specific radius relative to the total energy or flux of the entire source (an example is shown in figure 3.1). This parameter provides valuable insights into the angular distribution of the collected light from the point-like source. Higher encircled energy fractions within smaller apertures indicate better focusing and higher image quality.

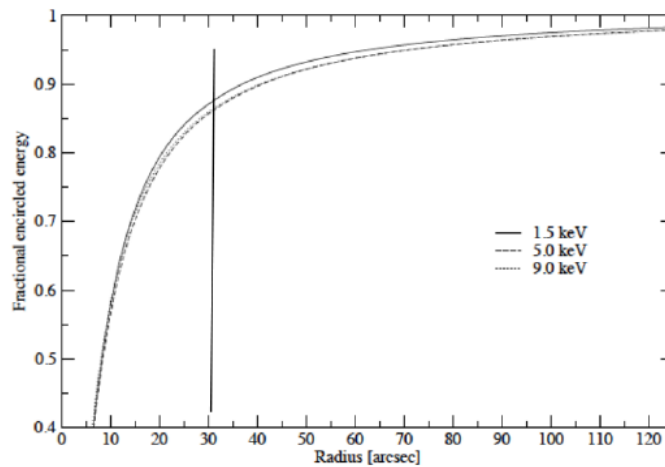


Figure 3.1: The EEF for the XMM-Newton pn camera varies with different energies. When observing at lower energies, a circle of a given radius encompasses a larger fraction of the total energy compared to observations at higher energies. This phenomenon is illustrated by plotting three different energy levels: 1.5 keV, 5.0 keV, and 9.0 keV. These energies are represented graphically by solid, dashed, and dotted lines, respectively. Image taken from European Space Agency, XMM-Newton Science Operations Centre.

The spectral resolution, or resolving power, is a measure of the ability to distinguish

close (in energy) spectral features, such as emission and absorption lines. This resolution is initially expressed in a Poissonian context as:

$$R_{Poisson} \propto \frac{\Delta\lambda}{\lambda} \propto \frac{2.35\sigma}{\sqrt{N}} \propto \frac{1}{\sqrt{N}} \quad (3.3)$$

Here, N represents the spectral counts, and σ is the error. The resolving power is inversely proportional to the square root of the spectral counts, indicating that higher counts lead to better resolution. In cases where the counts distribution deviates from the Poissonian distribution, the resolving power is modified and given by:

$$R_F = \frac{r_F}{\sqrt{N}} \quad (3.4)$$

In this equation, r_F is the Fano factor, the deviations from a pure Poisson regime. This formulation accommodates situations where the statistical distribution of counts differs from the Poisson distribution, offering a more flexible description of the resolving power.

3.1.3 Signal-to-noise ratio

The signal-to-noise ratio (SNR) is a crucial concept used to quantify the quality of data. It essentially measures the strength of the signal (desired information) relative to the background noise (“unwanted” interference or random fluctuations). Understanding the SNR is fundamental in assessing the reliability and significance of X-ray sources.

Mathematically, it’s represented as:

$$SNR = \frac{c_s}{\sqrt{c_s + c_{bkg}}} \quad (3.5)$$

where c_s represents the source counts and c_{bkg} represents the background counts.

The variance of signal (σ_S^2) includes contribution from both the source and background counts, given by Poissonian errors:

$$\sigma_S^2 = \sigma_{S+B}^2 + \sigma_B^2 = (\sqrt{S+B})^2 + (\sqrt{B})^2 = S + 2B \quad (3.6)$$

This leads to the expression for SNR as:

$$SNR = \frac{S}{\sqrt{S + 2B}} \quad (3.7)$$

Source (S) and background (B) counts can be expressed in terms of various parameters as follows:

$$S = \epsilon \cdot A \cdot T \cdot \Delta E \cdot F_{src} \quad (3.8)$$

$$B = A \cdot T \cdot \Delta E \cdot F_{bkg} \quad (3.9)$$

where ϵ is the efficiency in source detection, A is the effective area, T is the exposure time, ΔE represents the energetic band, F_{src} and F_{bkg} are the source and background fluxes respectively.

There are two regimes: one where the source dominates (low background or bright source) and the other where the background dominates. In the former, $B \ll \epsilon F_{src}$, leading to SNR depending only on source flux and exposure time ($\text{SNR} \propto \sqrt{F_{src} \cdot T}$). In the latter, $B \gg \epsilon F_{src}$, leading to $\text{SNR} \propto \sqrt{T} (F_{src}/2F_{bkg})$.

The minimum detectable flux is derived from SNR expression as:

$$F_{lim} = \frac{SNR}{\epsilon} \cdot \sqrt{\frac{B}{A \cdot \Delta E \cdot T}} \quad (3.10)$$

SNR can also be expressed in terms of angular and detector parameters:

$$\frac{S}{N} = \frac{S \cdot A^{\frac{1}{2}} \cdot T^{\frac{1}{2}}}{\sqrt{B_1 \cdot A + B_2 \cdot \Omega}} \quad (3.11)$$

where B_1 is the particle background, B_2 is the cosmic background, and Ω is the solid angle subtended by the source. These equations and explanations are fundamental in understanding the signal-to-noise ratio and its implications in data reduction processes, particularly in choosing the extraction region.

During the thesis work, observations from the Chandra, XMM, and NuSTAR missions were analyzed, leveraging their complementarity. Chandra boasts superior angular resolution, XMM features a significantly larger collecting area, ensuring noteworthy spectral resolution. Additionally, XMM has the advantage of its constituent instruments working simultaneously. Meanwhile, NuSTAR covers a much broader energy spectral range than the two former missions.

In cases where a particular source had observations available from different telescopes, a comprehensive analysis was conducted to gain a deeper understanding, capitalizing on the unique capabilities of each instrument.

3.2 Chandra X-ray Observatory

The Chandra X-ray Observatory (CXO), launched in 1999 by NASA, stands as a pioneering telescope designed to achieve unparalleled angular resolution, boasting the sharpest PSF among X-ray telescopes. Specifically, it features a HEW of 0.5" on axis, a remarkable accomplishment in the field. The key component responsible for this exceptional performance is the High-Resolution Mirror Assembly (HRMA), comprised of four reflecting mirrors with a diameter of 1.2 m and a focal length of 10 m. The effective area ranges from approximately 700 cm² between 1-2 keV to about 400 cm² at 5 keV. Chandra is equipped with four instruments:

- Advanced CCD Imaging Spectrometer (ACIS): ACIS consists of two detectors, ACIS-I (front-illuminated) and ACIS-S (front and back-illuminated). ACIS-I employs four CCDs for wide-field observations (16×16 arcmin²), while ACIS-S utilizes six CCDs and is optimized for readout when using the High Energy Transmission Grating (HETG). ACIS enables high-resolution imaging and offers moderate spectroscopic and time resolution capabilities.
- High-Resolution Camera (HRC): the HRC, operating on micro-channel plate technology, achieves a spatial resolution below 0.5 arcsec and a temporal resolution of approximately 16 ms. HRC-I is configured for imaging, while HRC-S is optimized for spectroscopy.
- High and Low Energy Transmission Grating (HETG and LETG): HETG facilitates high-resolution spectroscopy within the 0.4 to 10 keV energy range, with resolving power ranging from 800 (at 1.5 keV) to 200 (at 6 keV). LETG boasts a resolving power exceeding 1000 at energies in soft X-ray around 2 keV.

For this thesis work, the only instrument used for the analyzed observations was the ACIS imager, specifically the ACIS-S detector (without grazing).

3.3 XMM-Newton

The ESA XMM-Newton observatory currently stands as the premier instrument in terms of effective area. Comprising three telescopes, it features 58 nested Wolter I shells with a focal length of 7.5 m and a diameter of 70 cm. The observatory's impressive collecting area is 1900 cm² up to 150 eV, 1500 cm² at 2 keV, and gradually declines to 350 cm² at 10 keV.

The imagers utilized for observing the sources under investigation in this thesis are the PN and MOS (1 and 2) European Photon Imaging Camera (EPIC) cameras. Simultaneous operation of all three cameras is possible. Notably, the MOS cameras typically receive less than half of the radiation collected by the PN camera, as the radiation is split into two directions—directed towards the MOS cameras and the Reflection Grating Spectrometer (RGS).

The pn HEW varies from 15.1 to 14.8 arcsec in the energy range of 1.5-8 keV. For MOS1, the HEW is 13.6 arcsec at 1.5 keV and 12.5 arcsec at 8 keV. MOS2 exhibits a HEW range of 12.8-12.2 arcsec between 1.5 and 8 keV. The resolving power of the EPIC cameras is approximately $\Delta E/E \sim 20-50$ over the range 0.3-10 keV. The XMM-Newton telescope excels in photon collection, resulting in high-quality spectra.

Two of the three XMM-Newton telescopes are equipped with a grating spectrometer known as the Reflection Grating Spectrometer (RGS). The spectral resolution of the RGS varies from 100 to 500 in FWHM units within the 0.33-2.5 keV energy range. The

two components of the RGS are the Reflection Gratings Assemblies (RGAs) mounted on telescopes associated with the EPIC MOS cameras, and the RGS Focal Cameras (RFCs), consisting of 9 MOS CCD chips intercepting the dispersed light from the RGAs.

3.4 NuSTAR

Chandra and XMM-Newton are instruments covering the energy band below 10 keV. In contrast, NuSTAR telescope covers nominally the energy band from 3 until 79 keV. It consists of two co-aligned focusing hard X-ray telescopes, each featuring a multilayer coating. The use of a multilayer coating is a crucial aspect of the telescope's design, enabling it to effectively capture and focus hard X-rays. This innovative technology allows the telescopes to reflect and concentrate high-energy photons, providing enhanced sensitivity in the hard X-ray portion of the electromagnetic spectrum. The co-alignment of the telescopes ensures precise and coordinated observations, maximizing the scientific output of NuSTAR. This dual-telescope configuration contributes to NuSTAR's capabilities in exploring and studying celestial objects emitting hard X-rays. NuSTAR employs the Wolter I optic with a focal length of approximately 10 m. The collecting area is around 850 cm² at 9 keV, gradually decreasing to 60 cm² near 79 keV. The optical performance is characterized by a Half Power Diameter (HPD) of about 58 arcsec and a FWHM of around 16 arcsec. The spectral response of NuSTAR varies in the range of $\Delta E \approx 0.4\text{--}1.0$ keV in the range between 6-60 keV. In the figure 3.2, the effective area of NuSTAR is presented in comparison with the effective areas of Chandra and XMM-Newton. Unlike Chandra and XMM-Newton, which employ CCDs for detection, NuSTAR utilizes a Cadmium Zinc Telluride (CzT) detector. This difference in detector technology leads to a distinct spectroscopic resolution for NuSTAR. The CzT detector provides a unique capability for capturing and analyzing hard X-rays, expanding the observational capabilities of astronomers and researchers in this energy range.

3.5 Data reduction

This section describes the processes required to reduce X-ray data from various observations obtained with the Chandra X-ray Observatory, XMM-Newton, and NuSTAR telescopes. Following that, the procedure for detecting sources within the observations will be outlined.

3.5.1 Chandra data reduction

To conduct a scientific analysis of the data obtained using Chandra telescope, it is imperative to generate clean event files.

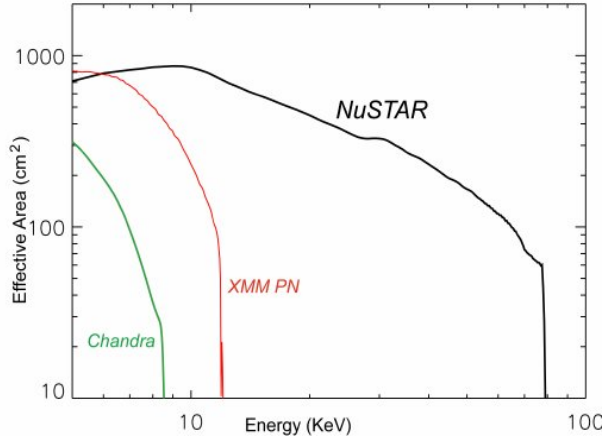


Figure 3.2: NuSTAR employs a low grazing angle design coupled with depth-graded multilayer coatings to enhance its effective area across a range of energies, surpassing the capabilities of telescopes like Chandra and XMM. This innovative approach extends NuSTAR’s sensitivity up to 80 keV (from Hunter et al. 2010).

The CIAO (Chandra Interactive Analysis of Observations) `chandra_repro` tool was employed for this purpose, facilitating the reprocessing of data through the Standard Data Processing (SPD). In this process, the latest calibrations are applied to the observations, ensuring their accuracy. The `chandra_repro` task sequentially executes various data processing steps for ACIS imaging data, excluding absolute astrometric corrections. Furthermore, it is necessary to inform the task about the observation mode, which can be either FAINT or VERYFAINT. The distinction lies in the fact that with the latter, there is a lower background level.

Essentially, the `chandra_repro` task performs the following steps in order:

- Reprocessing Data to Create a New Clean Event File: generates a new, clean event file, incorporating the latest calibrations and excluding astrometric corrections.
- Setting Observation-Specific Bad Pixel Files: ensures accuracy by setting observation-specific bad pixel files, even though most calibration files reside in the Chandra Calibration Database (CALDB).
- Filtering Data for a Specific Energy Band: for this study, the data are filtered within the chosen energy range. The energy range 0.3-7 keV, was selected to optimize the signal-to-noise ratio. At the extremes of the spectrum, where the effective area is the smallest, events may be dominated by background, hence excluding these energy ranges is crucial.

- Removing Warm ACIS Data: considering the variation in ACIS focal plane temperature (FPTEMP) during an observation, periods where FPTEMP exceeds the nominal set point temperature are removed.

Once the reprocessing is completed, a clean event file is available and ready for analysis.

In the case of OBSID 3956, a phenomenon known as “readout-streak” was observed within the clean event file. The tool `acisreadcorr` was used to reassign these readout streak events to their respective sources, correcting the sky coordinates. This is due to the presence of “pileup” in this dataset.

Pileup is a phenomenon that occurs in X-ray detectors, including those on telescopes like Chandra. It occurs when the rate of incoming X-ray photons is so high that multiple photons arrive at the same location on the detector at nearly the same time. Instead of being registered as separate events, these photons can overlap or pile up, leading to distorted or combined signals. It is particularly problematic when observing bright or intense X-ray sources, as the high photon flux increases the likelihood of multiple photons hitting the same detector pixel simultaneously. This can affect the ability to accurately analyze and interpret the data, especially for sources with high X-ray fluxes.

In this dataset, the pileup rate was found to be larger than 60%, therefore, this was taken into account during the spectral analysis by using a model for the pileup.

3.5.2 XMM-Newton data reduction

The Science Analysis Software (SAS) is a specialized software designed explicitly for the reduction and analysis of data obtained from XMM. The first step involves reprocessing Observation Data Files (ODFs) to obtain calibrated and concatenated event lists. The tasks utilized for this process are `emproc` and `epproc`. Following that, it is feasible to eliminate defective pixels and generate the light curve. Examining the light curve proves beneficial in choosing a threshold for excluding portions of the observation notably affected by noise, especially high-background intervals beyond $E > 10$ keV. Specifically, this “noise” originates from particle background interactions occurring between particles intercepted in the spacecraft orbits and the instrument.

The threshold value choice is different from each dataset, it is important determine where the light curve is slow and constant and choosing a threshold to delineate the “low background” intervals, as shown in figure 3.3. The result of this process is an EPIC filtered event list that has been cleared of time intervals characterized by high-background activity.

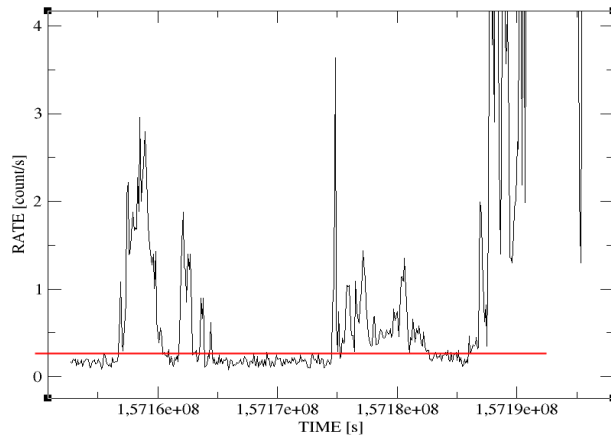


Figure 3.3: Example of particle flaring in the light curve in EPIC pn. The red line denotes where the light curve is low and sufficiently constant, the constant value becomes the threshold to be considered for having the cleaned data.

3.5.3 NuSTAR data reduction

The final telescope utilized in this study is NuSTAR, acknowledged for its revolutionary focusing capabilities, particularly its broad energy range spanning from 3 to 79 keV. The initial stage of a standard NuSTAR data reduction involves the generation of calibrated event files, which will undergo cleaning and contribute to the production of an exposure map. This essential process is executed using the `nupipeline` task. This task encompasses various crucial calibration steps, such as metrology data processing, correction of attitude file, flagging events for bad pixels, searching for hot and flickering pixels, energy correction, conversion of raw coordinates into detector and sky coordinates, in the first stage. In the second stage other steps follow, like filter file generation, Good Time Intervals generation and event file screening, event files dead time correction and sky exposure maps generation.

3.6 Source detection

Once the clean event files for all observations were available, the next step was the detection of sources within the observations. The source detection procedure is carried out around the coordinates of interest. This step is essential to verify whether the sources of interest in this work are revealed in X-rays.

For Chandra, the CIAO software’s `wavdetect` task was employed. This tool operates in two stages. Initially, it identifies potential source pixels within a dataset by iteratively

correlating it with “Mexican Hat” wavelet functions of various scale sizes. Pixels exhibiting significant positive correlation values are treated as presumed sources and are subsequently excluded from the image. The correlation process is then repeated at the same scale. In the second stage, a source list is generated based on the information obtained from the first stage at each wavelet scale. This tool effectively distinguishes closely spaced point sources and identifies extended sources, provided appropriate wavelet scales are selected. Key parameters of this task are *scales* and *sigthresh*: the *scales* parameter comprises a list of radii (in image pixels) corresponding to Mexican Hat wavelet functions, with each scale undergoing a wavelet transform. It is recommended to select wavelet scales that align with the sizes of the sources of interest, considering the PSF size. Typically, scales are chosen such that each succeeding value is a factor of 2 or the square root of 2 larger than the previous one. The primary consideration is to match the first scale size with the PSF. In this work I have set ”1.0, 1.4, 2.0, 2.8, 4.0, 5.6”. The *sigthresh* parameter represents the significance threshold for source detection. Setting a *sigthresh* value that is proportional to the inverse of the number of pixels in the image aims to yield approximately one false source per field; this parameter has been set in 10^{-4} .

The same process was carried out for the XMM datasets, in this case using the SAS tool `edetect_chain`. For these datasets (described in appendix A), the initial detection was performed by setting the threshold to 10 (equivalent to 4σ). In cases where detection did not occur in an observation, the threshold was gradually decreased to a minimum of 4 (corresponding to 2σ). If, even at the threshold value of 4, detection did not occur, the target(s) of interest in the dataset were considered non-detected.

An example of Chandra and XMM source detection is shown in figure 3.4.

Once the targets of interest in the various datasets have been detected, a positional check was performed to verify whether the X-ray emission originated from the nucleus of the galaxy and not from other potential objects. This positional verification was conducted with the assistance of both Hubble Space Telescope (HST) images of the sources, when available, and the NASA/IPAC Extragalactic Database (NED), accessible online.

3.7 Spectral extraction

The next step consists in the extraction of the spectra, the process involves selecting an extraction region for both the sources and the background, with the condition that the background region remains unaffected by the presence of other sources. The spectral extraction was performed assuming the sources to be point-like. The source extraction region should have a size comparable to the EEf at a fixed energy. For this reason, the choice of extraction radii varied for each telescope to achieve apertures that contained a good fraction of EEf.

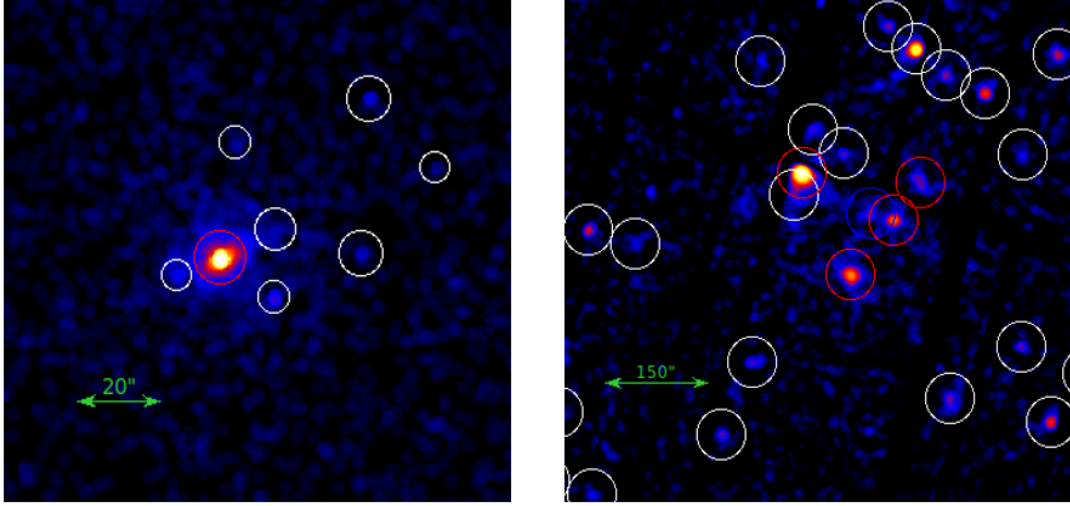


Figure 3.4: Example of source detection for the Chandra telescope (left image, 0.3-7 keV) and XMM (right image, 0.3-8 keV). Yellow circles indicate all detections made by the respective search task, while red circles denote the targets of interest that have been revealed.

For Chandra, the extraction radii for sources were 2-4 arcsec, which in terms of EEF corresponds to more than 90 percent, and for backgrounds, they were 15-25 arcsec. For XMM, source extraction radii covered 10-20 arcsec that in terms of EEF translates to 60-80% of the total energy, and background radii were set between 40-70 arcsec. For NuSTAR, source radii were about 40'' corresponding to almost 80% of the EEF, while background radii extended to about 150''.

The background extraction region has been selected to be sufficiently close to the source to quantify the level of background in the source vicinity, yet also distant enough to avoid incorporating any radiation from the source itself. Additionally, it should not contain signals from other sources, in order to achieve the best possible SNR, in agreement with what was said in section 3.1.3. In cases where the target(s) of interest within the observation are found to be weak (low statistics), the source extraction radius is chosen to be smaller. This is done to incorporate as little background as possible within the spectral extraction regions of the sources, aiming to conduct a good spectral analysis, albeit at the expense of achieving a source EEF lower than the desired 80-90%, but in favor of achieving the best possible SNR.

Table 3.1 lists the source and background extraction radii of the analyzed sources in this study, along with their respective net counts already subtracted from the background.

During this phase, two crucial files are generated, providing information about the instrument response. Response information serves as the bridge between astrophysical quantities like flux and spectral shape, and detector-specific values such as count rates in spectral bins. Thus, having accurate response information is essential for drawing meaningful conclusions from astrophysical observations. Response information is primarily categorized into two types: Ancillary Response Files (ARFs) and Response Matrix Files (RMFs).

ARFs encapsulate the total throughput of the detector, referred to as effective area (see section 3.1.1), measured in cm^2 . The ARF essentially translates the collected counts into a modeled flux ($\text{photons cm}^{-2} \text{s}^{-1}$). ARFs also typically include information about off-axis effects like vignetting.

RMFs contain information about energy redistribution, is logically a 2-d array which gives for each input photon energy the probability of assigning the photon to a given output channel of the detector.

Once the spectral extraction process is completed, the extracted spectrum of the source, the respective background spectrum, the ARF and RMF files are grouped together into a single file containing the source's counts convolved with the response of the respective instrument. This file is then ready for analysis using the XSPEC software, which is a command-driven, interactive X-ray spectral-fitting program designed to be completely detector-independent, making it applicable for use with any spectrometer.

Based on the initial analysis of the 11 available systems, particularly from HST images and the X-ray source detection process, the following observations have been made:

- Interaction Phase: 8 systems are in an interaction phase, with a distance range of $20 < d < 40$ kpc for six of them, while one is a $d \sim 150$ kpc (Arp 200).
- Merging/Coalescing Phase: 3 systems are in a more advanced merging or coalescing state ($d < 10$ kpc).

Among these, 4 systems have been partially detected (only one component of the system was detected in the X-ray detection process); for 1 system, no X-ray detection was achieved for either of the two interacting galaxies. The summary of these findings is illustrated in the accompanying diagram in figure 3.5.

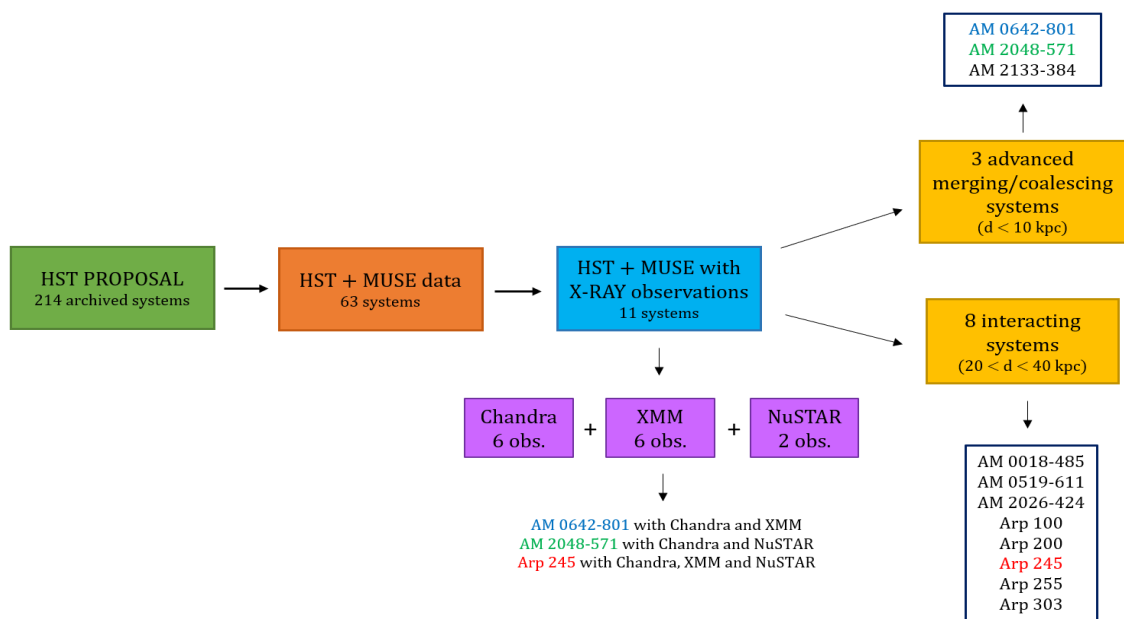


Figure 3.5: Starting from HST observations, there are 63 systems with MUSE data available, then from these 11 targets with available X-ray observations were identified. Among these, 8 systems are in an interactive state, while 3 systems are in a more advanced state.

Target	Telescope	Obsid	Source region	Background region	Net cts/s
ESO119-IG054	Chandra	13001	3.6''	22''	$(2.3 \pm 0.2) \cdot 10^{-2}$
ESO119-IG055	Chandra	13001	3.8''	22''	$(1.4 \pm 0.5) \cdot 10^{-3}$
AM 0642-801	Chandra	14925	4.1''	16''	$(0.8 \pm 0.1) \cdot 10^{-3}$
	XMM	0781710101	15.5''	44''	$(1.5 \pm 0.3) \cdot 10^{-3}$
IC 0563	Chandra	15070	3''	22''	$(1.2 \pm 0.3) \cdot 10^{-3}$
IC 0564	Chandra	15070	4''	22''	$(1.1 \pm 0.3) \cdot 10^{-3}$
AM 2133-384 (core1)	Chandra	15073	4.2''	16''	$(4.0 \pm 0.5) \cdot 10^{-3}$
AM 2133-384 (core2)	Chandra	15073	2.8''	16''	$(0.7 \pm 0.2) \cdot 10^{-3}$
ESO285-G019 (West)	Chandra	22360	3.2''	15''	$(1.0 \pm 0.3) \cdot 10^{-3}$
	Chandra	3956	4.6''	41''	$(3.5 \pm 0.1) \cdot 10^{-1}$
NGC 2992	XMM	0840920201	16''	69''	(12.6 ± 0.1)
	NuSTAR	90501623002	40''	149''	(1.6 ± 0.1)
NGC 2993	Chandra	3956	3.3''	41''	$(2.0 \pm 0.1) \cdot 10^{-2}$
IC 5063	Chandra	7878	3.5''	23''	$(1.1 \pm 0.1) \cdot 10^{-1}$
	NuSTAR	60061302002	38.8''	140''	$(2.8 \pm 0.1) \cdot 10^{-1}$
NGC 0087	XMM	0152330101	16.5''	55''	$(4.5 \pm 0.6) \cdot 10^{-3}$
NGC 0088	XMM	0152330101	10.6''	55''	$(2.1 \pm 0.4) \cdot 10^{-3}$
NGC 0089	XMM	0152330101	14''	55''	$(1.3 \pm 0.1) \cdot 10^{-2}$
NGC 0092	XMM	0152330101	19''	55''	$(6.1 \pm 0.2) \cdot 10^{-2}$
Arp 200	XMM	0693540101	17.2''	57''	$(3.0 \pm 0.3) \cdot 10^{-2}$
UGC 05304b	XMM	0103260801	6.6''	29''	$(3.5 \pm 0.3) \cdot 10^{-3}$

Table 3.1: The table displays the extraction regions for the detected sources and background in arcseconds ("), along with the net (i.e., background-subtracted) count rates within the extraction region.

Chapter 4

Analysis

4.1 Spectral analysis

Spectral analysis was carried out using the XSPEC software (Arnaud 1996) adopting a phenomenological approach. Initially, models were constructed with simplistic components, gradually increasing complexity by incorporating additional elements, if needed. Primary components for the phenomenological analysis included absorption attributed to the Milky Way, primary power-law emissions (comprising absorbed and scattered components), emission lines such as Fe K α , and thermal components used to characterize the soft excess. Statistical significance assessment of any newly introduced component was performed using the F-test limit; the components considered are clearly based on our current understanding of AGN. This statistical tool facilitated the determination of the validity and necessity of incorporating additional components into the model, ensuring a robust and accurate representation of the observed spectral data. Through this iterative process of model refinement and evaluation, the aim was to elucidate the underlying physical mechanisms driving the observed phenomena, thereby advancing understanding of the system under investigation. The statistical methods used in the conducted spectral analysis varied depending on the nature of the data. The χ^2 statistic (Gaussian statistic) was employed when the data were normally distributed and there were a sufficient number of events in each data bin. Conversely, in cases of low statistics characterized by few events and non-Gaussian uncertainties, the Cash statistic (Poissonian statistic) was utilized. The Cash statistic is commonly employed in scenarios of low counts to assess the goodness of fit during the analysis (Cash 1979).

4.2 Phenomenological models

4.2.1 Power law

To incorporate the primary emission from the Active Galactic Nucleus (AGN), as described in the first chapter, a simple photon power law (`po`) is used:

$$A(E) = KE^{-\Gamma} \quad (4.1)$$

Here, the free parameters include the photon index Γ and the normalization K [photons/keV/cm²/s] at 1 keV.

4.2.2 Absorption components

In heavily obscured AGN, the primary emission undergoes attenuation, particularly at energies below 10 keV. This attenuation is accounted for in the phenomenological models through a photoelectric absorption component situated at the redshift of the source (`zpha`). The absorption is parametrized as follows:

$$M(E) = \exp[-N_H\sigma(E[1+z])] \quad (4.2)$$

Here, $\sigma(E[1+z])$ represents the photoelectric cross-section in units of cm², which depends on the observed energy, z denotes the redshift of the source, and N_H is the equivalent hydrogen column density measured in units of 10²² atoms cm⁻².

Another absorption factor that requires consideration is the Galactic absorption (i.e., absorption by the Milky Way), reproduced by `pha` in `XSPEC`. It is analogous to `zpha` but at $z=0$. This parameter was evaluated using the HEASARC (High Energy Astrophysics Science Archive Research Center) command-line tool `nh` by inputting the coordinates of the target of interest and the equinox. Table 4.1 indicating the values of Galactic absorption of the Milky Way for the different analyzed systems, with the values depending on the positions of the respective systems.

4.2.3 Emission line component

In the X-ray spectrum of an AGN, especially when the main continuum is attenuated in the soft band, several emission lines may be observed. Among these, the most prominent is the iron fluorescence $K\alpha$ line at 6.4 keV if originating from neutral material, sometimes accompanied by the fainter $K\beta$ line at 7.06 keV. These emission lines can be represented by a Gaussian line profile (`zgauss`) positioned at the redshift of the source:

$$A(E) = K \frac{1}{\sqrt{2\pi}\sigma} \exp\left[-\frac{(E - E_l)^2}{2\sigma^2}\right] \quad (4.3)$$

System	$N_{\text{H}}(\text{gal})$ [cm^{-2}]
AM 0018-485	$1.6 \cdot 10^{20}$
AM 0519-611	$1.6 \cdot 10^{20}$
AM 0642-801	$1.1 \cdot 10^{21}$
AM 2026-424	$3.4 \cdot 10^{20}$
AM 2048-571	$6.0 \cdot 10^{20}$
AM 2133-384	$3.3 \cdot 10^{20}$
Arp 100	$2.5 \cdot 10^{20}$
Arp 200	$9.5 \cdot 10^{20}$
Arp 245	$5.3 \cdot 10^{20}$
Arp 255	$3.1 \cdot 10^{20}$
Arp 303	$4.5 \cdot 10^{20}$

Table 4.1: Values of Galactic absorption for the different analyzed systems, obtained using the `nh` tool from HEASARC.

Here, E_l represents the line energy expressed in keV, σ denotes the line width in keV, and K is the normalization factor.

4.2.4 Thermal emission component

The X-ray spectrum of AGN often exhibits a significant soft emission, typically below 2-3 keV, ascribed to the host galaxy. This emission can be approximately modeled by a thermal emission component originating from hot diffuse gas, commonly referred to as `mekal` (Mewe et al. 1985). Additionally, the model includes line emissions from elements such as carbon (C), nitrogen (N), oxygen (O), and silicon (Si). The main parameters for the `mekal` component include:

- Plasma temperature kT [keV]
- Hydrogen density in cm^{-3}
- Metal abundances
- Redshift z
- Normalization

These parameters collectively define the characteristics of the thermal emission component and the associated line emissions within the model.

Figure 4.1 illustrates an example of a phenomenological model incorporating the components described earlier.

The main models used for spectral analysis are as follows:

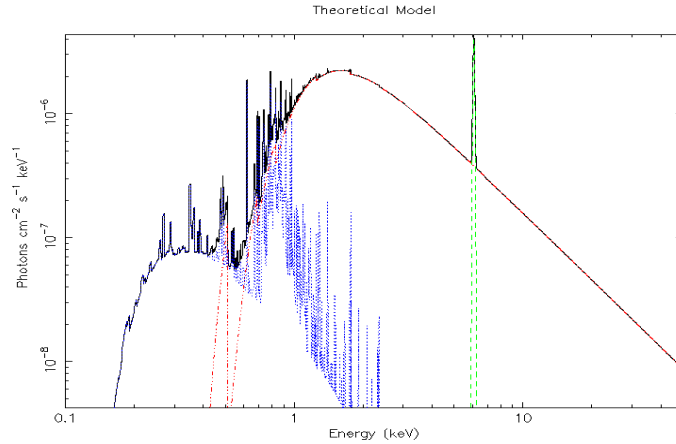


Figure 4.1: An example of a spectral model is shown in the plot. The solid black line represents the overall model, while individual components are illustrated in different colors. At low energies (around 0.1 keV), absorption due to the Milky Way is observed, followed by a dip in the spectrum caused by intrinsic absorption at the redshift of the source (**zpha**). The primary component (**po**) is represented in red, with a photon index $\Gamma=1.8$. The Fe $K\alpha$ emission line at 6.4 keV is shown in green. Additionally, the **mekal** component, characterized by a temperature of 0.3 keV, is plotted as a blue line.

- a. $\text{pha}^*\text{zpha}^*\text{po}$
- b. $\text{pha}^*(\text{mekal}+\text{zpha}^*\text{po})$
- c. $\text{pha}^*(\text{po}+\text{zpha}^*(\text{po}+\text{zgau}))$
- d. $\text{pha}^*(\text{mekal}+\text{zpha}^*(\text{po}+\text{zgau}))$
- e. $\text{pha}^*(\text{mekal}+\text{po}+\text{zpha}^*\text{po})$
- f. $\text{pha}^*(\text{zpha}^*(\text{po}+\text{zgau}))$
- g. $\text{pha}^*(\text{mekal}+\text{po}+\text{zpha}^*(\text{po}+\text{zgau}_1+\text{zgau}_2))$
- h. $\text{pha}^*(\text{mekal}+\text{po}+\text{zpha}^*(\text{po}+\text{zgau}))$

Where two power law appear in the model, the first is due to scattering, while the second represents the nuclear one, which may be obscured (**zpha** component multiplying the power law). The Γ of the scattering power law is fixed to be the same as that of the nuclear one, as expected in the case of Thomson scattering. It should also be said that the power-law model used in the analysis could represent the primary emission from the AGN and/or the unresolved emission from a possible population of X-ray binaries that remain

individually undetected by the current instruments. The population of X-ray binaries can be in the form of low-mass x-ray binaries (LMXBs) and high-mass X-ray binaries (HMXBs); the former comprises X-ray sources accreting from a low-mass companion, the latter from a high-mass companion. As such, their combined (unresolved) X-ray emission can be considered a proxy of the host galaxy stellar mass and star formation, respectively.

In the case of non-detected sources, specific tools were used to quantify an upper limit value on the observed flux to derive a value on the intrinsic luminosity of the galaxy core, these will be described in the dedicated section (see section 4.5).

4.3 χ^2 and Cash statistics

The chi-square (χ^2) statistic is a measure commonly used in statistical analysis to evaluate the goodness of fit between observed data and a theoretical model. It quantifies the discrepancy between the observed data and the expected values predicted by the model.

$$\chi^2 = \sum_{k=1}^n \frac{(O_k - E_k)^2}{\sigma_k^2} \quad (4.4)$$

where O_k represents the observational data, E_k the expected value, σ_k^2 the uncertainty associated with data point k , and n the number of available data points. Essentially, it quantifies how much the adopted model diverges from the observational standpoint, taking into account for each data point its respective error bar (the larger the error bar, the easier for a model to approach the observational data point).

The rule of thumb for a good fit is that:

$$\frac{\chi^2}{dof} \approx 1 \quad (4.5)$$

where dof represents the number of degrees of freedom (the number of available data points minus the number of free parameters in the fit). If this holds true, it indicates that the adopted model effectively reproduces the observed data.

Where the assumptions underlying the χ^2 statistic are not met, such as when dealing with low-count data, the Cash statistic (`cstat` in `Xspec`) was used (Cash 1979). The Cash statistic is based on the likelihood function (it quantifies the probability of observing a particular set of data given a specific statistical model with unknown parameters), which measures the probability of obtaining the observed data given a specific model. For a given model M with parameters θ and observed data D , the likelihood function $L(\theta|D)$ is defined as the probability density of observing D given the model M and its parameters.

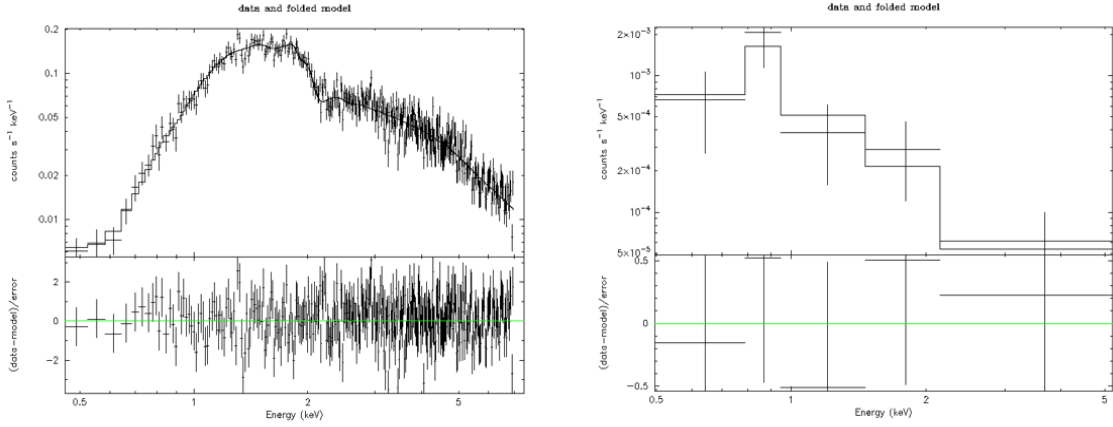


Figure 4.2: On the left: high-quality spectrum where χ^2 statistic is adopted (NGC 2992), while on the right a low-photon statistic spectrum (and Cstat applied) is shown (IC 0564).

The Cash (C) statistic is defined as

$$C = -2\ln(\Theta) + 2 \sum_i (M_i - D_i) \quad (4.6)$$

where Θ represents the maximum likelihood estimate of the model parameters, M_i and D_i are the model-predicted and observed counts in bin i , respectively.

The Cash statistic essentially quantifies the deviation between the model-predicted counts and the observed counts. A smaller value of C indicates a better fit of the model to the data. Unlike the chi-square statistic, the Cash statistic does not assume Gaussian-distributed uncertainties, making it suitable for analyzing low-count data or data with non-Gaussian uncertainties.

In this study, the χ^2 statistic was applied to targets with more than 1000 counts, grouped into 25 counts per bin. For all those falling below this threshold, the C statistic was applied, with one count per bin. In Figure 4.2 examples of a spectrum treating with the χ^2 statistic and C statistic are shown.

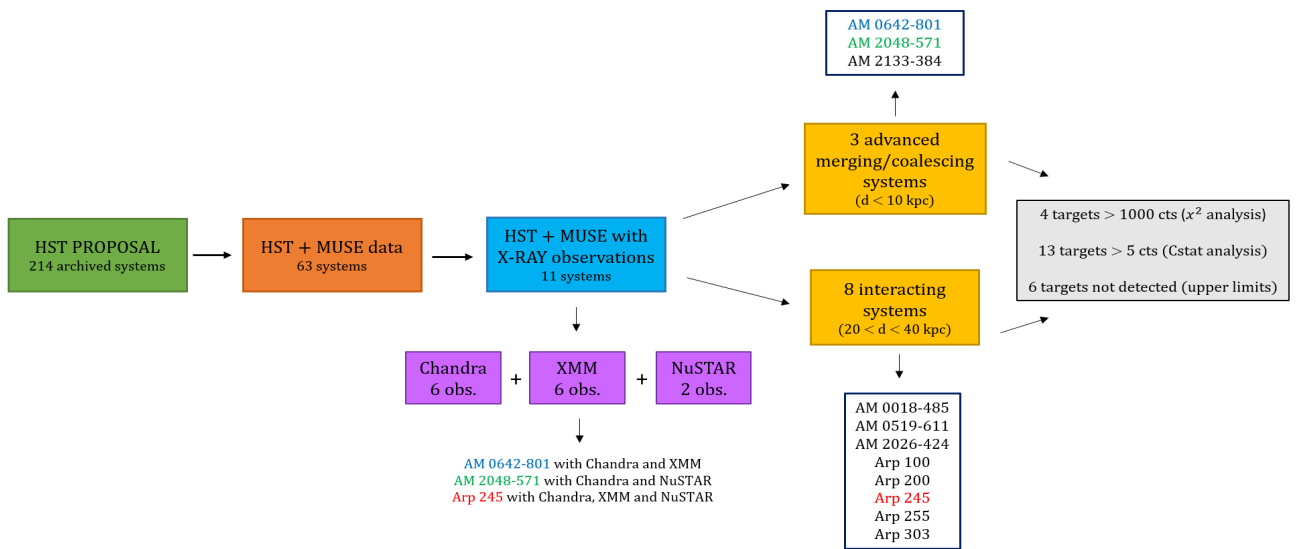


Figure 4.3: To complete the diagram in figure 3.5, among the 11 systems with X-ray observations, there is a total of 23 targets available for spectral analysis. 4 of these were analyzed using χ^2 statistics, 13 using Cstat statistics, while the remaining 6 were not detected, and specific tools were used to obtain upper limits. In this context, a single system can include multiple sources. For example, the system AM 0018-485 comprises four galaxies, from NGC 0087 to NGC 0092.

4.4 Main outcomes from X-ray spectral analysis

This section discusses the main results of the X-ray analysis of the targets analyzed during my thesis work, with a brief description of the systems. Spectral analysis focuses on obtaining the primary spectral information of the sources under consideration, specifically the spectral index, column density, observed flux, and intrinsic luminosity, to provide an initial indication for their classification.

Most of the sources analyzed do not have any X-ray analysis in the literature, therefore their spectral analysis also serves as an initial indication of emission in this band for these galaxies.

4.4.1 AM 0018-485

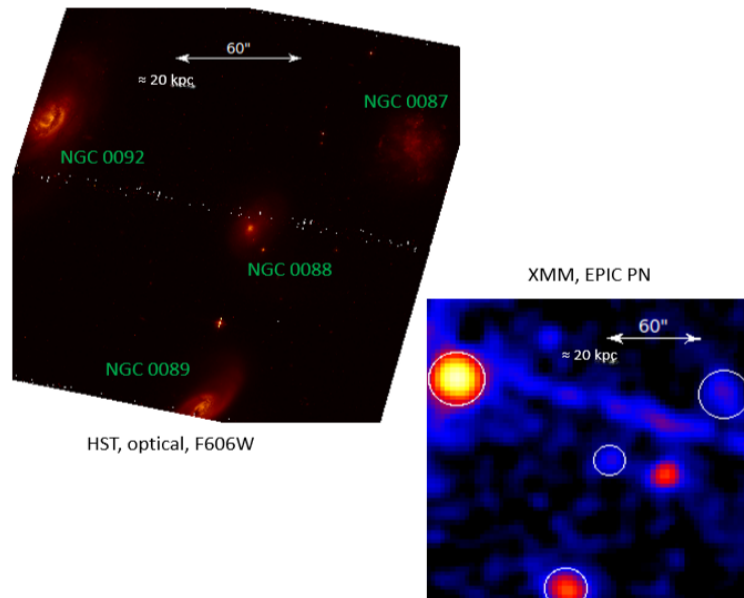


Figure 4.4: On the left, the HST image of AM 0018-485 obtained with filter F606W, while on the right, the XMM pn image in the 0.3-10 keV band of the same region. The circles mark the four galaxies of the system.

Robert’s Quartet (in figure 4.4) is a striking collection of four distinct galaxies, situated roughly 160 million light-years away near the center of the southern constellation Phoenix. This group, discovered by John Herschel in the 1830s, consists of NGC 0087, NGC 0088, NGC 0089, and NGC 0092.

- NGC 0087: This irregular galaxy resembles the Magellanic Clouds, which are satellite galaxies of the Milky Way.

- NGC 0088: Located at the center, this spiral galaxy is enveloped in a diffuse outer layer, likely made up of gas.
- NGC 0089: It is a spiral galaxy characterized by two prominent spiral arms.
- NGC 0092: The largest galaxy in the quartet, is an Sa-type spiral galaxy with a peculiar appearance. One of its arms, about 100,000 light-years long, is distorted from interactions and contains a significant amount of dust.

Located at $z=0.011$, Robert’s Quartet stands out as an exemplary compact galaxy group. Such groups provide excellent opportunities to study galaxy interactions and their influence. This system has been observed with XMM. The models used for the spectral analysis and the corresponding results are shown in the table 4.2.

Target	Model (a)	Statistics (b)	Γ (c)	$N_{\text{H}}(z)$ (d)	kT (e)	Line E, EQW (f)	F_{2-10} (g)	L_{2-10} (h)
NGC 0087	a.	$\frac{C}{\text{d.o.f.}} = \frac{108.7}{100}$	$1.91^{+0.74}_{-0.32}$	< 0.16			$-14.01^{+0.19}_{-0.30}$	$39.42^{+0.19}_{-0.29}$
NGC 0088	a.	$\frac{C}{\text{d.o.f.}} = \frac{56.6}{48}$	$2.13^{+1.69}_{-0.52}$	< 0.26			$-14.43^{+0.34}_{-0.67}$	$39.00^{+0.21}_{-0.66}$
NGC 0089	h.	$\frac{C}{\text{d.o.f.}} = \frac{120.2}{187}$	$2.14^{+0.36}_{-0.42}$	$426.8^{+209.8}_{-224.7}$	$0.39^{+0.30}_{-0.10}$	$6.44^{+0.05}_{-0.05}, 2.79^{+1.94}_{-1.40}$	$-12.02^{+0.95}_{-0.91}$	$41.40^{+0.95}_{-0.91}$
NGC 0092	b.	$\frac{\chi^2}{\text{d.o.f.}} = \frac{57.2}{39}$	$2.69^{+0.28}_{-0.23}$	$0.49^{+0.21}_{-0.11}$	$0.63^{+0.06}_{-0.07}$		$-12.97^{+0.06}_{-0.07}$	$40.46^{+0.06}_{-0.06}$

Table 4.2: Main spectral parameters of the XMM-Newton spectra of AM 0018-485 system. (a) phenomenological model assumed for spectral analysis (description in 4.2.4); (b) adopted statistics, with the ratio between the statistical value and the degrees of freedom; (c) spectral index; (d) column density at the redshift of the source in units of 10^{22} cm^{-2} ; (e) temperature of the thermal emitting medium in keV; (f) emission line and its equivalent width in keV; (g) logarithm of the 2-10 keV observed flux in units of $\text{erg/cm}^2/\text{s}$; (h) logarithm of the 2-10 keV intrinsic luminosity in units of erg/s . All errors are reported at the 90% confidence level.

It should be noted that NGC 0089 appears to be the galaxy with the highest nuclear activity compared to the others, exhibiting a relatively high X-ray luminosity $L_{(2-10)\text{keV}} \sim 10^{41} \text{ erg/s}$. It appears to be a highly obscured AGN, riddled with significant errors, yet still emitting intense luminosity, a possible indication that we are possibly in the presence of an obscured AGN. This is supported by the rise of the source emission in the hard X-rays, while in the soft X-ray emission is mostly dominated by a scattering component, which led to adding a second power law component to fit this rise. The photon index Γ of this power law due to scattering was fixed with the Γ value representing the power law of nuclear emission.

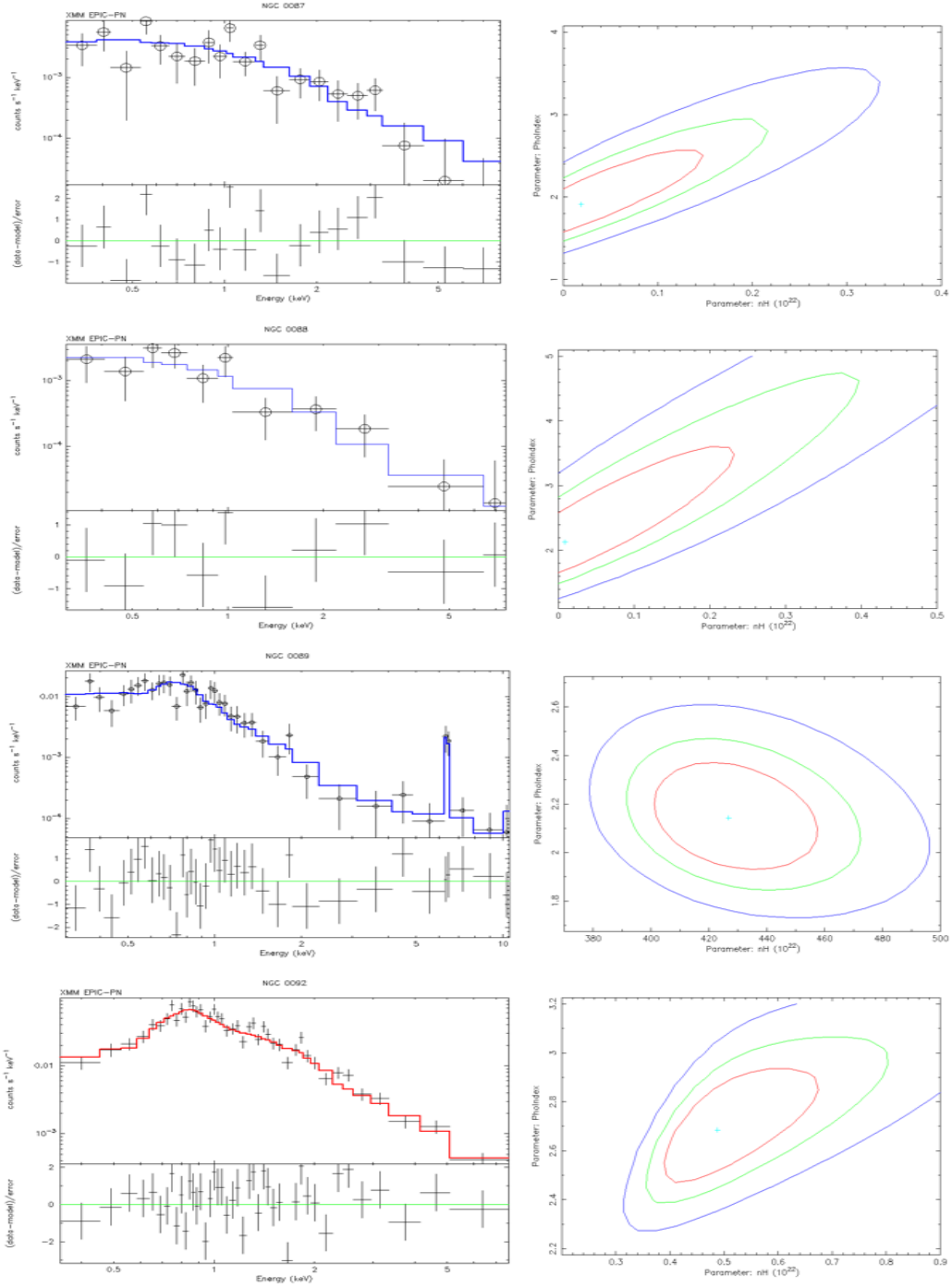


Figure 4.5: In the first panel, the best fit of AM 0018-485 system XMM spectra is shown, alongside the $N_H(z)$ - Γ contour plot: red, green and blue levels correspond to a Delta fit statistic of 1.0, 2.706 and 9.21 (corresponding to 68%, 90% and 99% confidence level, respectively). Blue lines indicate models analyzed with C statistics, while red lines with χ^2 statistics.

The presence of a prominent neutral iron line at $6.44^{+0.05}_{-0.05}$ keV is also highlighted, with an equivalent width ~ 3 keV.

For the other three galaxies in the system, the low observed $L_{(2-10)\text{keV}}$ values (below 10^{40} erg/s) suggest that their X-ray emission is most likely dominated by star formation, and in this case, the power-law component could represent an unresolved population of X-ray binaries, so therefore not consistent, at face value, with AGN emission.

4.4.2 AM 0642-801

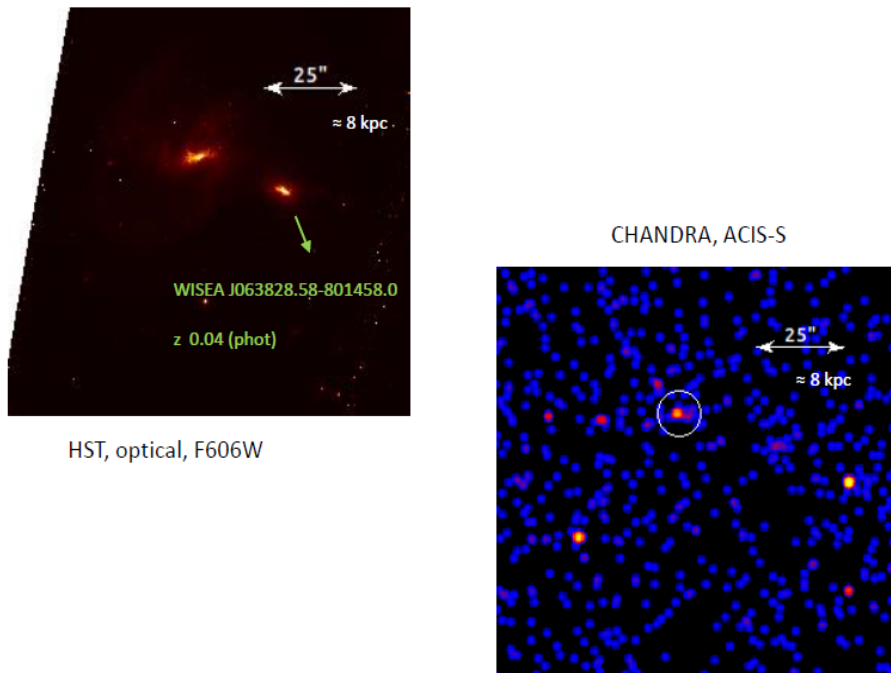


Figure 4.6: On the left, the HST image of AM 0642-801 with filter F606W is shown, while on the right the Chandra image 0.3-7 keV of the same region is reported.

This system is located at a redshift of $z=0.016$, observations have been made using both XMM-Newton and Chandra telescopes. In the optical, it is classified as a collisional ring galaxy (Madore et al. 2009).

Its apparent companion, WISEA J063828.58-801458.0, located at a $z=0.04$ (photometric, from NED), does not show any X-ray emission. Furthermore, additional information for this system is limited. Given the absence of uncertainty in the photometric redshift, it was decided to also analyze this companion, despite its lack of X-ray detection. Upper limits on flux and luminosity for this galaxy have been estimated using specific tools, with the results presented in the dedicated section (see 4.5).

In the case of XMM-Newton, for AM 0642-801, it was necessary to perform a spectral analysis of the background first (C_{back}), as the background emission was dominant over the X-ray emission from the source, which is not the target of the pointing. The background was fitted with a purely phenomenological model, and instead of subtracting it from the source spectrum as it is typically done, its spectral fit was incorporated within the source spectrum.

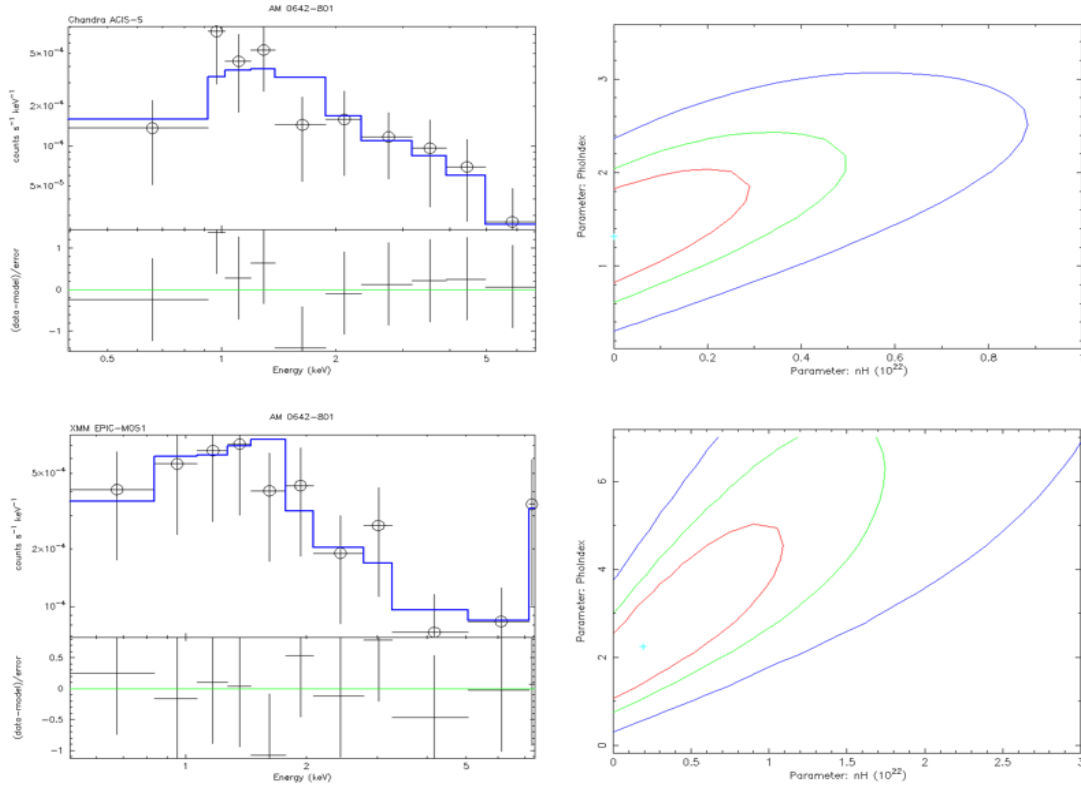


Figure 4.7: The panel on the left shows the Chandra and XMM-Newton spectra of AM 0462-801, while on the right the $N_{\text{H}}(z)$ - Γ contour plot: color codex is the same as Fig. 4.5.

The data obtained from spectral analysis (Table 4.3) suggests that the source exhibits a relatively consistent spectral behavior across both instruments, though some differences are observed, particularly in the flux and luminosity values (both consistent within 2.5σ between the two telescopes). This difference in values obtained from the two telescopes could also probably be due to an increase in activity in AM 0642-801 over time, as the Chandra observation was completed in 2013, while the XMM observation was conducted in 2016.

It cannot be ruled out that the data might be compatible with an AGN, although

the X-ray luminosity values are more indicative of the presence of a star-forming galaxy, or the emission could suggest the presence of a population of unresolved X-ray binaries near the galaxy's core region.

Therefore, the data do not appear to be completely inconsistent with an AGN, but further analysis may be needed to confirm this interpretation.

The spectral line found at 7.28 keV, while statistically improving the fit, is at an energy where emission is not commonly seen in AGN spectra. Given that nickel (Ni) $K\alpha$ transitions (~ 7.48 keV) are typically weak, the nature of this feature remains uncertain.

	XMM	Chandra
Model	a.+C _{back}	a.
Statistics	$\frac{C}{d.o.f.} = \frac{20.0}{28}$	$\frac{C}{d.o.f.} = \frac{19.0}{26}$
Γ	$2.25^{+3.19}_{-1.15}$	$1.31^{+0.81}_{-0.53}$
$N_H(z)$	< 1.20	< 0.33
F_{2-10}	$-13.29^{+0.19}_{-0.27}$	$-14.05^{+0.24}_{-0.32}$
L_{2-10}	$40.47^{+0.16}_{-0.24}$	$39.71^{+0.24}_{-0.32}$

Table 4.3: Main spectral parameters of XMM and Chandra spectra of AM 0642-801. All errors are reported at the 90% of confidence level.

4.4.3 AM 0519-611

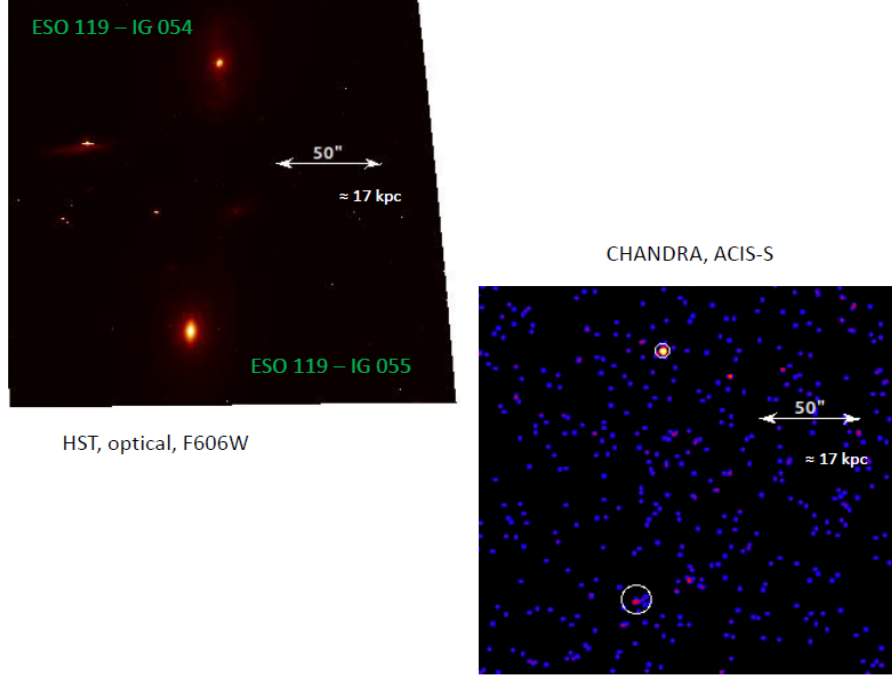


Figure 4.8: On the left, the HST image of AM 0519-611 obtained with the filter F606W, while on the right, the Chandra image in the 0.3-7 keV band of the same region.

AM 0519-611 is a system consisting of two interacting spiral galaxies, ESO119-IG054 (north component) and ESO119-IG055 (southern component) (Arp et al. 1987, see figure 4.8). These galaxies exhibit characteristics typical of interacting pairs, such as disturbed structures and tidal features. The system is located at a redshift of $z=0.016$. The interactions between these galaxies are likely leading to significant gravitational effects and star formation activity.

This system was observed by Chandra, and the main results obtained through spectral analysis are given in the table below, with the relative bests fit (table 4.4).

For ESO119-IG054, the photon index Γ is consistent with the typical values expected for AGN. From the X-ray spectral analysis, only an upper limit on the N_{H} was derived ($N_{\text{H}} < 0.20 \cdot 10^{22} \text{ cm}^{-2}$ at the 90% c.l.). Additionally, the presence of an emission line at around 6.37 keV, likely associated with iron fluorescence, further supports the presence of an AGN. The luminosity in the X-ray band also indicates a moderate level of activity, that may be consistent either with a low-luminosity AGN or a SF galaxy.

ESO119-IG055, on the other hand, shows a photon index with very large uncertainties, making it difficult to determine the precise spectral shape. The absorption level also in this case, it is just an upper limit ($N_{\text{H}} < 1.20 \cdot 10^{22} \text{ cm}^{-2}$ at the 90% c.l.). Unlike

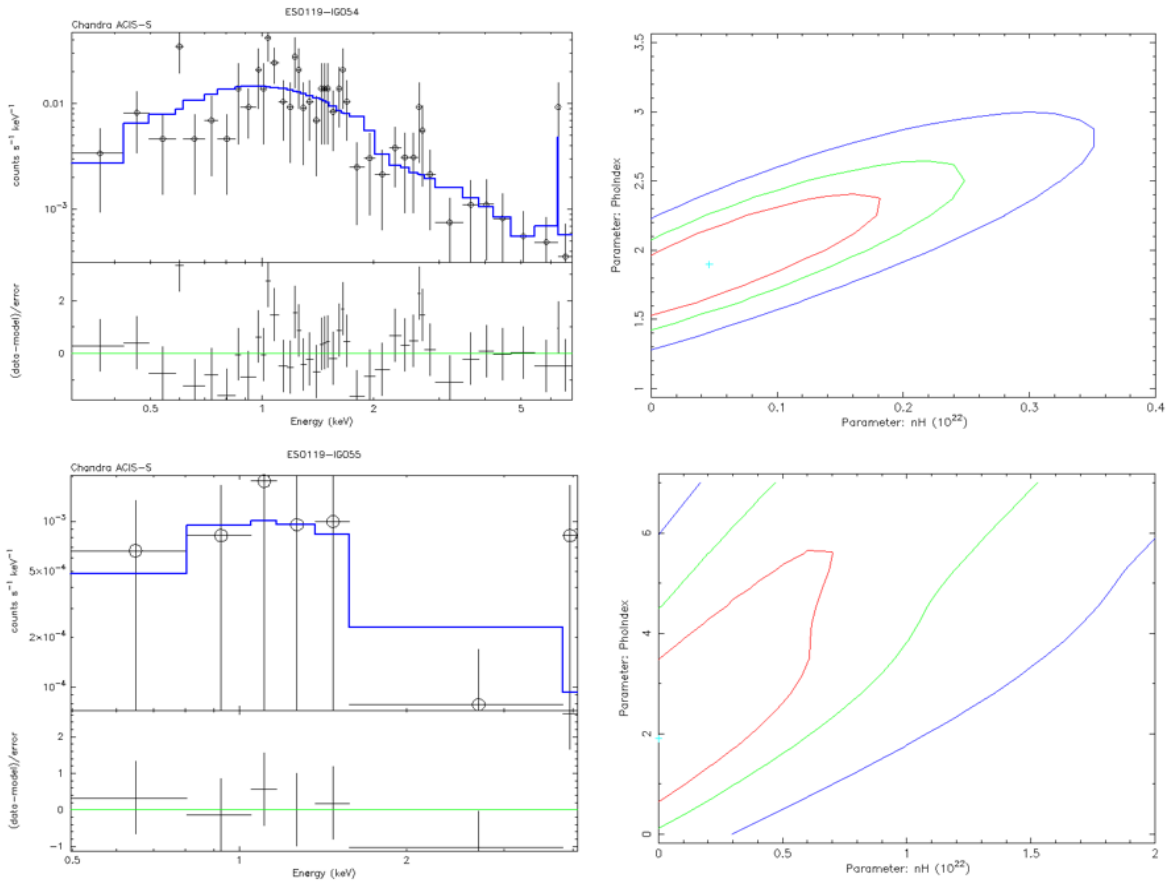


Figure 4.9: The Chandra best-fit spectrum of the two galaxies, ESO119-IG054 and ESO119-IG055, are shown on the left, while on the right the respective $N_{\text{H}}(z)$ - Γ contour plot. Confidence levels are the same as in Fig. 4.5.

	ESO119-IG054	ESO119-IG055
Model	f.	a.
Statistics	$\frac{C}{\text{d.o.f.}} = \frac{73.3}{82}$	$\frac{C}{\text{d.o.f.}} = \frac{4.4}{4}$
Γ	$1.90^{+0.56}_{-0.43}$	$1.75^{+6.25}_{-1.29}$
$N_{\text{H}}(z)$	< 0.20	< 1.10
Line E, EQW (*)	$6.37^{+0.07}_{-0.07}, < 3.90$	
F_{2-10}	$-12.95^{+0.18}_{-0.19}$	$-14.01^{+0.50}_{-1.45}$
L_{2-10}	$40.81^{+0.17}_{-0.19}$	$39.78^{+0.74}_{-0.95}$

Table 4.4: Main spectral parameters of Chandra spectra of AM 0519-611. (*) corresponds to a neutral iron line at 6.4 keV and its respective equivalent width in keV. All errors are reported at the 90% of confidence level.

ESO119-IG054, there is no clear detection of an iron emission line. Furthermore, the X-ray flux and luminosity are significantly lower, placing this source at the lower end of the AGN luminosity scale. This could suggest the presence of a SF galaxy, but the large uncertainties in the spectral parameters make it difficult to reach a definitive conclusion.

4.4.4 AM 2133-384

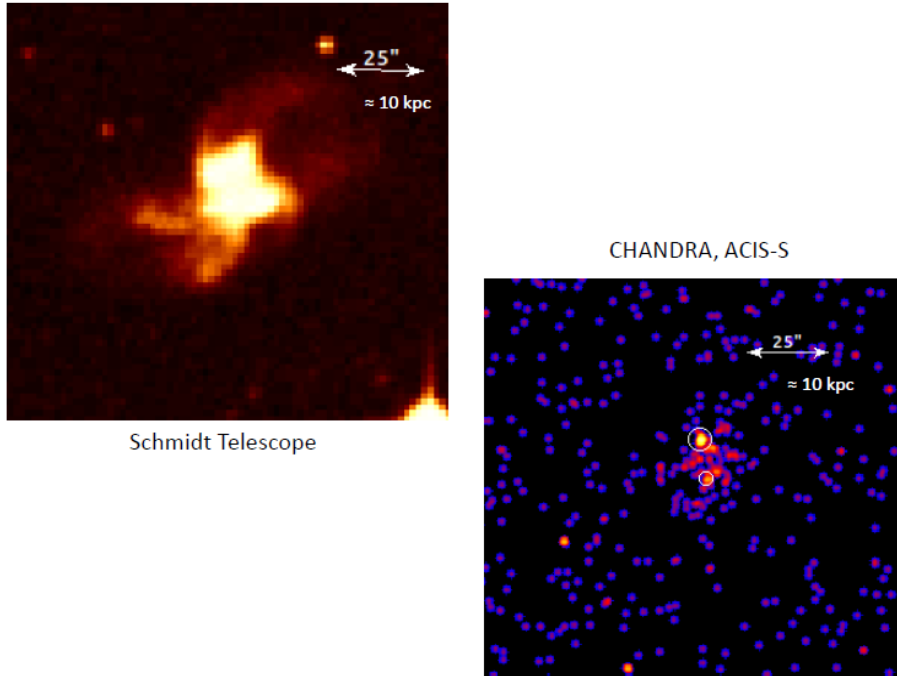


Figure 4.10: On the left the optical Schmidt telescope image of AM 2133-384, and on the right the Chandra 0.3-7 keV image of the same region. The two white circles indicate the potential cores of the system, with core 1 on the North and core 2 on the South. The positions of these nuclear regions have also been verified using MUSE data for this target.

AM 2133-384 is a galactic system that consists of a pair of interacting galaxies, currently in the process of merging. Observed with optical and infrared telescopes (e.g. Dopita et al. 2002), AM 2133-384 reveals detailed gravitational interactions and intense star formation, creating features like stellar bridges and tidal tails. The merger compresses interstellar gas, leading to the birth of new stars and star clusters. Studying this system provides valuable insights into galactic mergers and their effects on the structure and evolution of the involved galaxies.

This system, located at a redshift of $z=0.019$, has been challenging to interpret in X-ray analysis, primarily due to the limited data available. The results and their respective best fits for the system are presented below (see tab 4.5).

For core 1, the photon index is quite low, suggesting a rather hard spectrum. This could indicate a non-thermal emission process, or it might suggest a heavily absorbed source where the intrinsic emission is being modified. However, the absorption appears

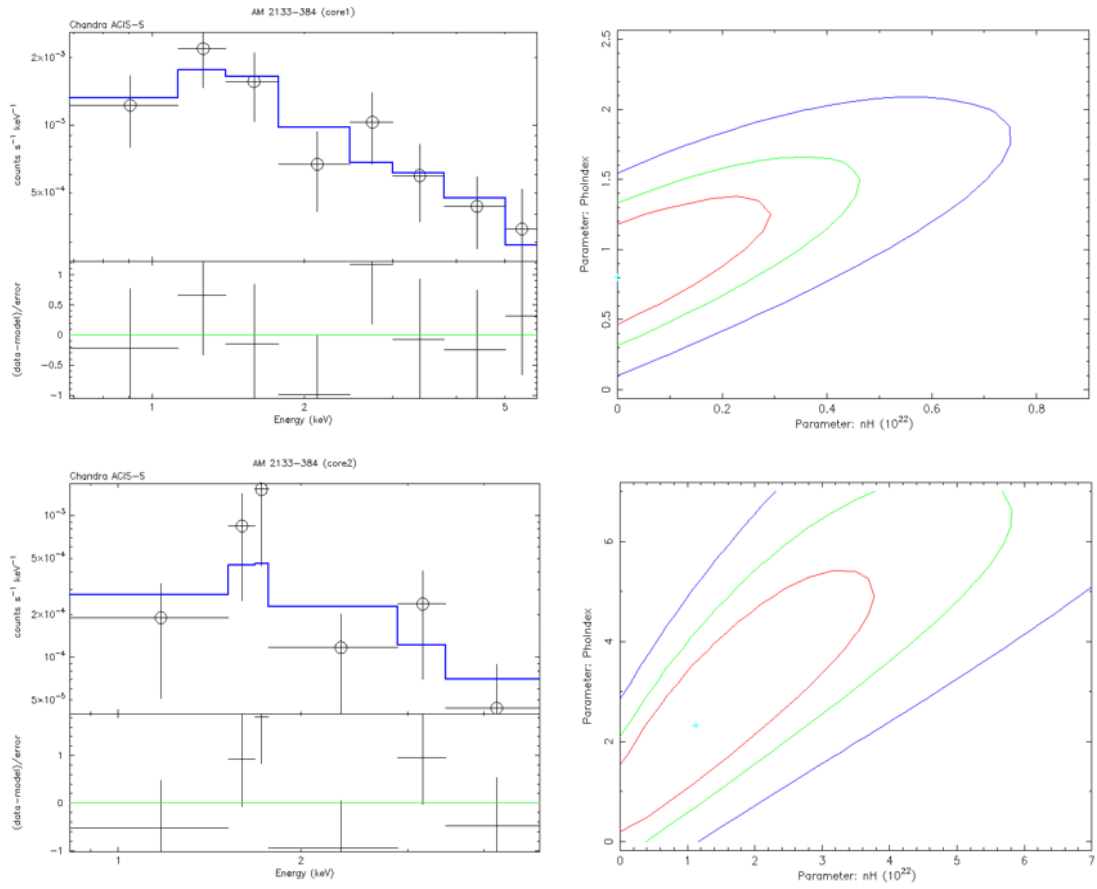


Figure 4.11: On the left panel, the best fit of Chandra AM 2133-384 core1 and core2 spectra is shown. On the right panel it is reported the respectively $N_{\text{H}}(z)$ - Γ contour plot. Confidence levels are the same of Fig. 4.5.

	AM 2133-384 (core 1)	AM 2133-384 (core 2)
Model	a.	a.
Statistics	$\frac{C}{\text{d.o.f.}} = \frac{42.4}{50}$	$\frac{C}{\text{d.o.f.}} = \frac{11.5}{8}$
Γ	$0.71^{+0.69}_{-0.39}$	$2.34^{+3.46}_{-2.22}$
$N_{\text{H}}(z)$	< 0.33	< 4.23
F_{2-10}	$-13.12^{+0.19}_{-0.21}$	$-14.07^{+0.59}_{-0.48}$
L_{2-10}	$40.77^{+0.17}_{-0.21}$	$39.84^{+0.57}_{-0.47}$

Table 4.5: Main spectral parameters of Chandra spectra of AM 2133-384. All errors are reported at the 90% of confidence level.

to be relatively low ($N_{\text{H}} < 0.33 \cdot 10^{22} \text{ cm}^{-2}$ at the 90% c.l.). The X-ray flux and luminosity place this source within the range expected for an AGN, but the unusually hard spectrum raises questions about its exact nature. The intermediate luminosity level ($\log(L_X) \sim 40.8$ erg/s) suggests that it could be a combination of emission from an AGN along with emission from an unresolved population of X-ray binaries. It could also indicate a high level of star formation due to the close interaction between the two components.

For core 2, the photon index is much higher, but with very large uncertainties, making it difficult to draw firm conclusions about the spectral shape. The absorption is relatively unconstrained. The X-ray flux and luminosity are lower compared to core 1, maybe indicative of star formation.

Overall, core 1 appears to have a harder spectrum than typical AGN, which might suggest an unusual emission mechanism or some level of obscuration that is not fully accounted for. Core 2 has a much softer spectrum but is poorly constrained, requiring deeper observations to clarify its nature.

4.4.5 AM 2026-424 (ESO285-G019 West and East)

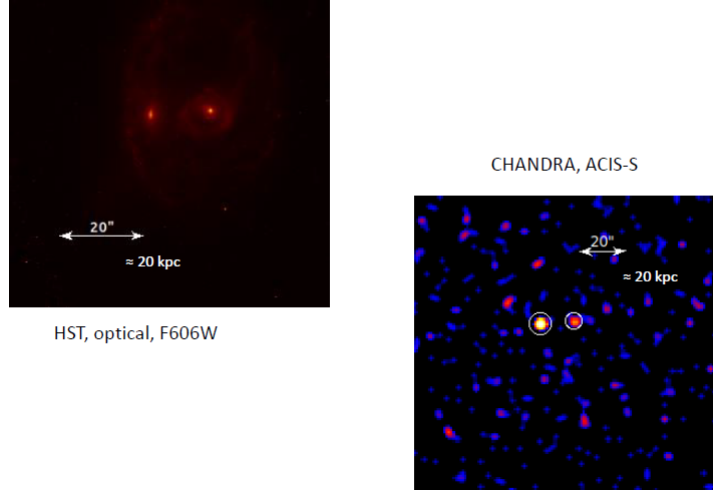


Figure 4.12: On the left, the HST image of AM 2026-424 taken with the F606W filter, while on the right, the Chandra image of the same region in the 0.3-7 keV energy range.

The AM 2026-424 system, a.k.a. ESO285-G019 (West and East, respectively) is classified as a peculiar galaxy, that exhibits unusual structural, spectral, or kinematic characteristics that deviate from the standard classifications of elliptical, spiral, or lenticular galaxies. This may be the result of interactions, mergers, tidal distortions, or internal dynamical processes; in particular this system is classified as collisional ring galaxy (Madore et al. 2009). This system, located at $z=0.012$, exhibits morphological and spectral characteristics indicative of past interactions or mergers with other galaxies. The HST images reveal that AM 2026-424 has a highly disturbed morphology. Key features include extended tidal tails, a warped disk, and possible remnants of a galactic core merger. The Chandra observation of this system shows that its X-ray emission is difficult to analyze (limited data quality), because the source is not the target of the observation (i.e., it is located at an off-axis angle of $2.9'$). The eastern component was not detected in the detection process and will be addressed in the dedicated section (see 4.5).

The photon index is quite high ($\Gamma \sim 3.3$). This suggests that the X-ray emission is dominated by a soft component, possibly linked to thermal processes. Such a steep slope is not typical of heavily obscured AGN, where absorption usually flattens the spectrum. The measured absorption is moderate, meaning that while some gas is present along the line of sight, it does not significantly alter the observed spectrum. The observed X-ray flux and intrinsic luminosity place this source within the range expected for a low-luminosity AGN (see tab 4.6).

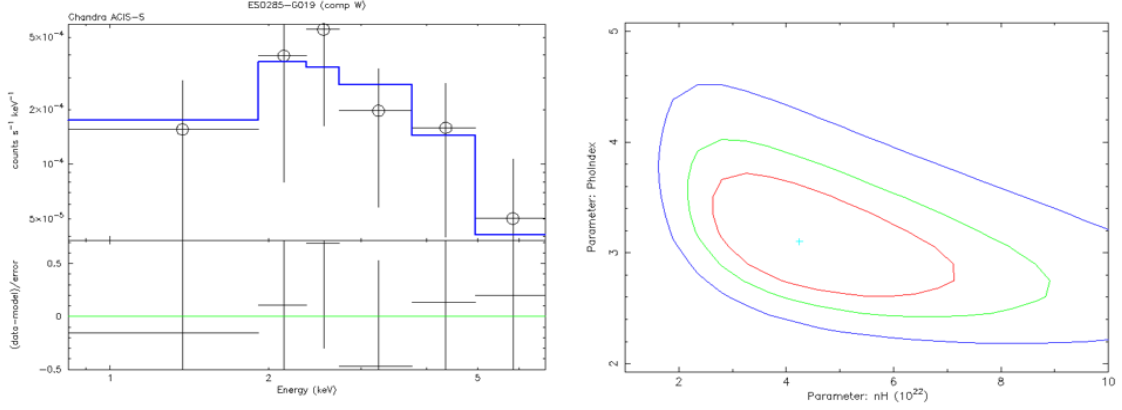


Figure 4.13: The best-fit model for the Chandra spectrum of ESO 285-G 019 (West) on the left, while the right panel presents the $N_{\text{H}}(z) - \Gamma$ contour plot, confidence levels equal to Fig. 4.5.

ESO285-G019 (West)	
Model	a.
Statistics	$\frac{C}{\text{d.o.f.}} = \frac{3.0}{9}$
Γ	$3.33^{+0.68}_{-0.54}$
$N_{\text{H}}(z)$	$4.51^{+3.31}_{-1.83}$
F_{2-10}	$-13.59^{+1.52}_{-0.41}$
L_{2-10}	$41.25^{+1.65}_{-0.42}$

Table 4.6: Main spectral parameters of Chandra spectra of ESO285-G019 (West component). All errors are reported at the 90% of confidence level.

4.4.6 Arp 200

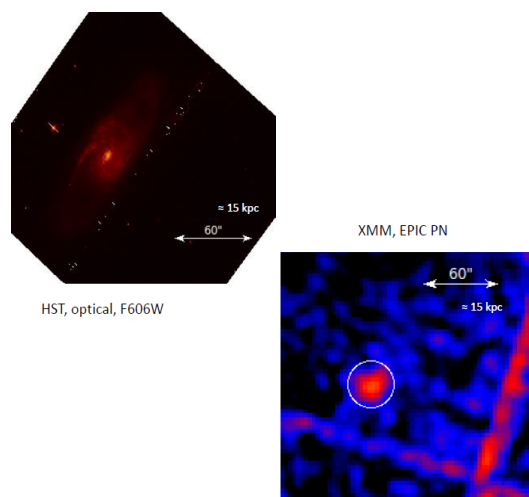


Figure 4.14: On the left, the HST image of Arp 200 using the F606W filter is shown, while on the right is the XMM image of the same region in the 0.3-10 keV band.

In literature, Arp 200 (a.k.a. NGC 1134) is classified as spiral galaxy; it is included in Halton Arp’s Atlas of Peculiar Galaxies under the category “Galaxies with material ejected from nuclei”. Condon et al. 2002 classify it as a starburst galaxy based on the following criteria: (1) the radio to far-infrared (FIR) flux ratio, (2) the 25 micron to 60 micron flux ratio, and (3) the absence of extended radio structures.

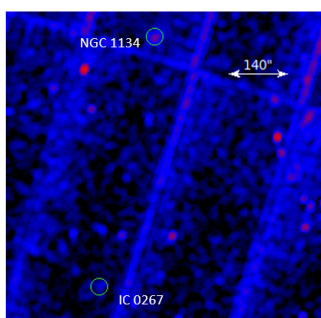


Figure 4.15: Region in the XMM 0.3-10 keV band of about 800×800 arcsec². As can be seen, there is a significant distance between these two interacting galaxies. This system exhibits the largest separation (about 150 kpc) between the interacting galaxies, with NGC 1134 at the top and IC 0267 at the bottom.

Together with the galaxy IC 0267, NGC 1134 forms an interacting system. However, IC 0267 does not appear in the HST image because it is located at a significant distance

from NGC 1134, over 150 kpc away. In the following panel, its position is shown within the XMM-Newton observation field; unfortunately, it was not detected in X-rays, and upper limits on its flux and luminosity have been derived (see section 4.5).

It is located at a redshift $z=0.012$. Below are reported best fit and main spectral results of this target, analyzed with XMM-Newton.

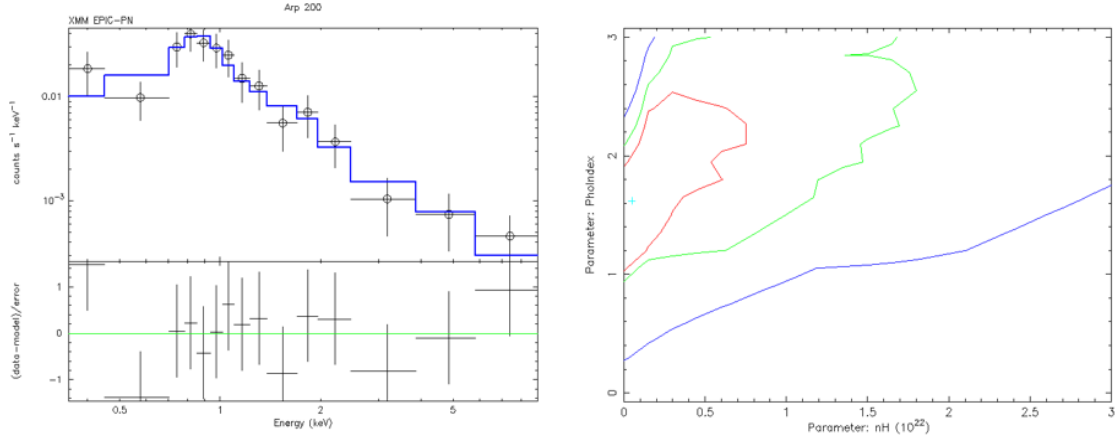


Figure 4.16: The left panel shows the best fit of the XMM Arp 200 spectrum, while the right panel displays the $N_H(z) - \Gamma$ contour plot. Confidence levels are the same as in Fig.4.5.

The results (Table 4.16) suggest that the galaxy may host either a weak AGN or a SF galaxy. The spectrum indicates a non-thermal emission source. The column density of neutral hydrogen along the line of sight derived from spectral analysis is only an upper limit ($N_H < 0.33 \cdot 10^{22} cm^{-2}$ at the 90% c.l.). The power-law spectrum is consistent with the low luminosity and moderate column density typically observed in both weak AGN and star-forming galaxies. However, given the low luminosity of about 10^{40} erg/s, the power-law emission could be also attributed to an unresolved population of X-ray binaries located near the core region of the galaxy. More detailed studies across different wavelengths would be needed to fully understand the nature of its X-ray emission.

Arp 200	
Model	b.
Statistics	$\frac{C}{d.o.f.} = \frac{79.2}{100}$
Γ	$1.62^{+1.00}_{-0.63}$
$N_H(z)$	< 0.95
F_{2-10}	$-13.17^{+0.21}_{-0.29}$
L_{2-10}	$40.33^{+0.21}_{-0.29}$

Table 4.7: Main spectral parameters of XMM spectra of Arp 200. All errors are reported at the 90% of confidence level.

4.4.7 Arp255 (UGC 05304b)

Arp 255 (a.k.a. UGC 05304) is a peculiar system, observed by XMM-Newton, composed of a pair of galaxies that show signs of interaction. The larger component of the system is the spiral galaxy UGC 05304a (not detected in X-ray), followed by its companion UGC 05304b, whose results are reported below. It is located at a redshift of $z=0.04$, and the distance from aim point of observation is about 3.6 arcmin.

The X-ray analysis of UGC 05304b indicates a relatively soft X-ray spectrum, suggesting that the source could be emitting non-thermal radiation, which could be associated with AGN, but may also represent the emission of a population of X-ray binaries or some emission from the host. The presence of a thermal component is also observed, with a temperature that suggests hot gas in the galaxy's surroundings, potentially linked to either star formation or the environment around an AGN. The flux and intrinsic luminosity are both moderate, consistent with the possibility of a weak AGN or strong star-forming activity that contributes to the X-ray emission. Overall, data point to UGC 05304b being a source of moderate X-ray luminosity, with both thermal and non-thermal emission components.

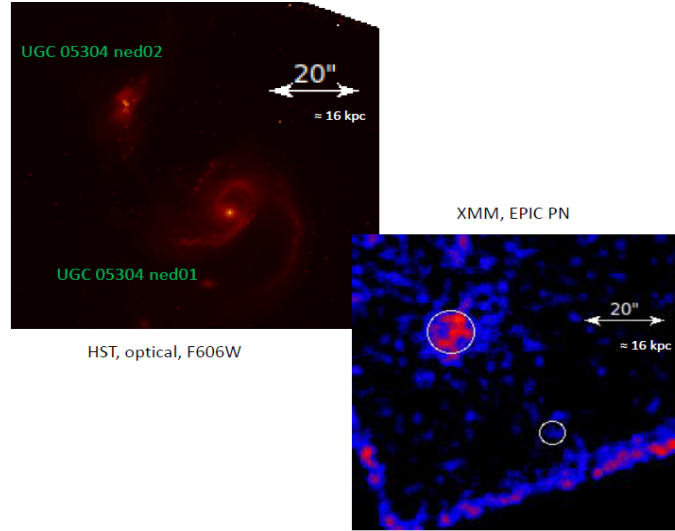


Figure 4.17: On the left, the HST image of Arp 255 obtained with filter F606W, while on the right the XMM 0.3-10 keV image of the same region.

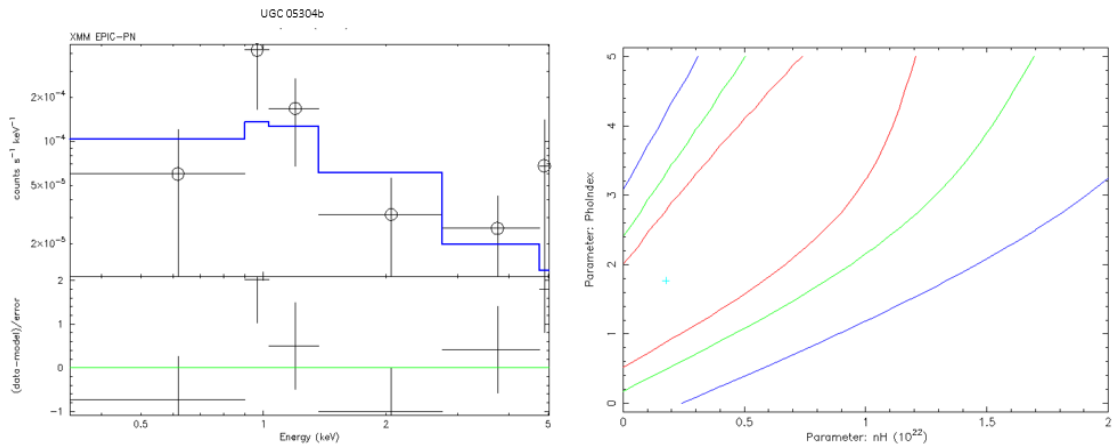


Figure 4.18: On the left panel best, the fit of XMM UGC 05304b spectra is shown. On the right panel it is reported the $N_{\text{H}}(z)$ - Γ contour plot, with color codex equal to Fig. 4.5.

UGC 05304b	
Model	b.
Statistics	$\frac{C}{\text{d.o.f.}} = \frac{139.3}{189}$
Γ	$1.67^{+0.68}_{-0.56}$
$N_{\text{H}}(z)$	< 0.34
kT	$0.68^{+0.16}_{-0.11}$
F_{2-10}	$-13.84^{+0.19}_{-0.22}$
L_{2-10}	$40.72^{+0.18}_{-0.21}$

Table 4.8: Main spectral parameters of XMM spectra of UGC 05304b. All errors are reported at the 90% of confidence level.

4.4.8 Arp 303

Arp 303 is a system of interacting galaxies, comprising two barred spiral galaxies: IC 0563 (bottom right) and IC 0564 (top left). These galaxies are very bright at infrared wavelengths ($\log(L_{\text{IR}}/L_{\odot}) \simeq 11.23$) and host many bright star-forming regions, in fact they are also classified as Luminous Infrared Galaxies (LIRGs) (Armus et al. 2009). A LIRG is a galaxy whose infrared emission exceeds $10^{11} L_{\odot}$ (typically in 8-1000 μm band). The infrared energy primarily comes from dust that is heated by radiation from young stars, but it can also be associated with the presence of an AGN. LIRGs are typically in a phase of vigorous star formation, often triggered by galactic mergers, and can be a precursor to ULIRGs (Ultra Luminous Infrared Galaxies), which are even more luminous in the infrared ($> 10^{12} L_{\odot}$).

The system, observed by the Chandra telescope, is situated at $z=0.02$. The main results of spectral analysis are reported below.

For IC 0563, the photon index suggests a relatively soft X-ray spectrum, indicating non-thermal emission, probably related with an AGN. IC 0564 shows a much steeper photon index, which may indicate a stronger non-thermal component. However, the flux and luminosity values in the 2-10 keV X-ray band for these interacting galaxies are relatively low (see Table 4.9). Therefore, the non-thermal emission probably is not associated with an AGN but rather originates from dense star-forming regions or an unresolved population of X-ray binary stars near the core regions of the two galaxies.

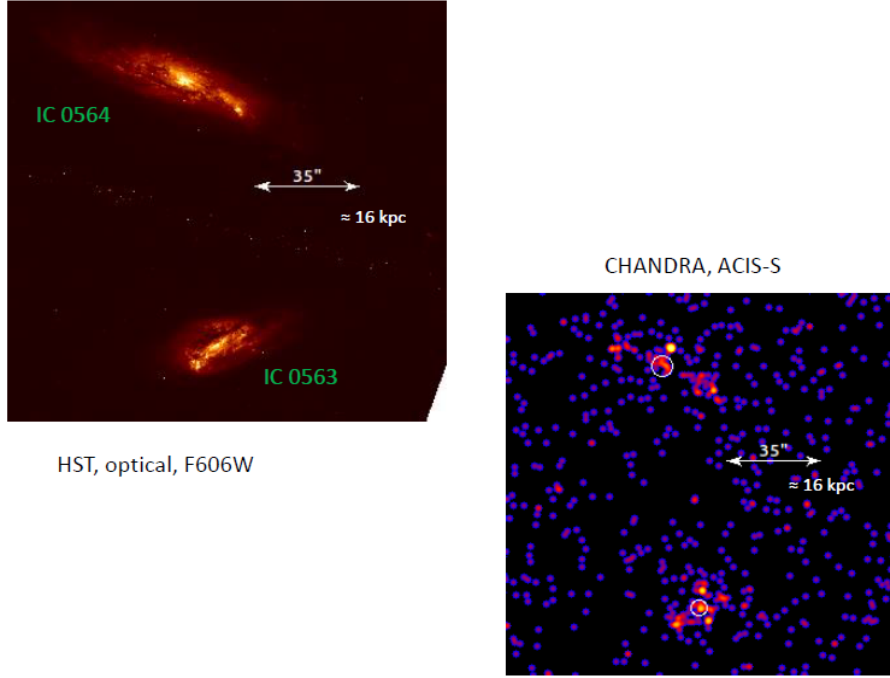


Figure 4.19: On the left, the HST image of Arp 303 with filter F606W, while on the right the Chandra 0.3-7 keV image of the same region.

	IC 0563	IC 0564
Model	a.	a.
Statistics	$\frac{C}{\text{d.o.f.}} = \frac{19.5}{14}$	$\frac{C}{\text{d.o.f.}} = \frac{19.9}{12}$
Γ	$1.31^{+0.85}_{-0.75}$	$2.69^{+2.85}_{-0.92}$
$N_{\text{H}}(z)$	< 0.22	< 0.58
F_{2-10}	$-13.83^{+0.35}_{-0.40}$	$-14.64^{+0.43}_{-0.80}$
L_{2-10}	$40.08^{+0.38}_{-0.41}$	$39.33^{+0.48}_{-0.78}$

Table 4.9: Main spectral parameters of Chandra spectra of IC 0563 and IC 0564, respectively. All errors are reported at the 90% of confidence level.

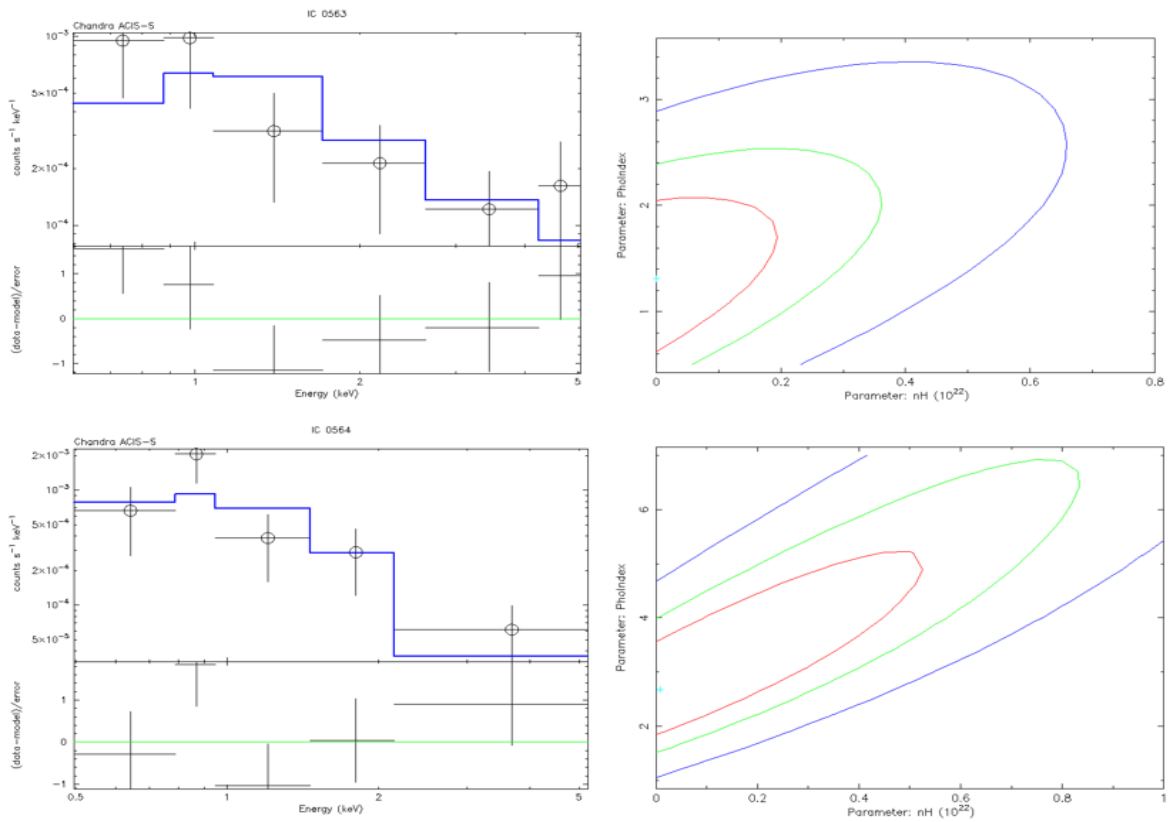


Figure 4.20: The left panel displays the Chandra best fit of the Arp 303 spectrum, while the right panel shows the $N_{\text{H}}(z) - \Gamma$ contour plot, with confidence levels equal to Fig. 4.5.

4.4.9 Arp 245

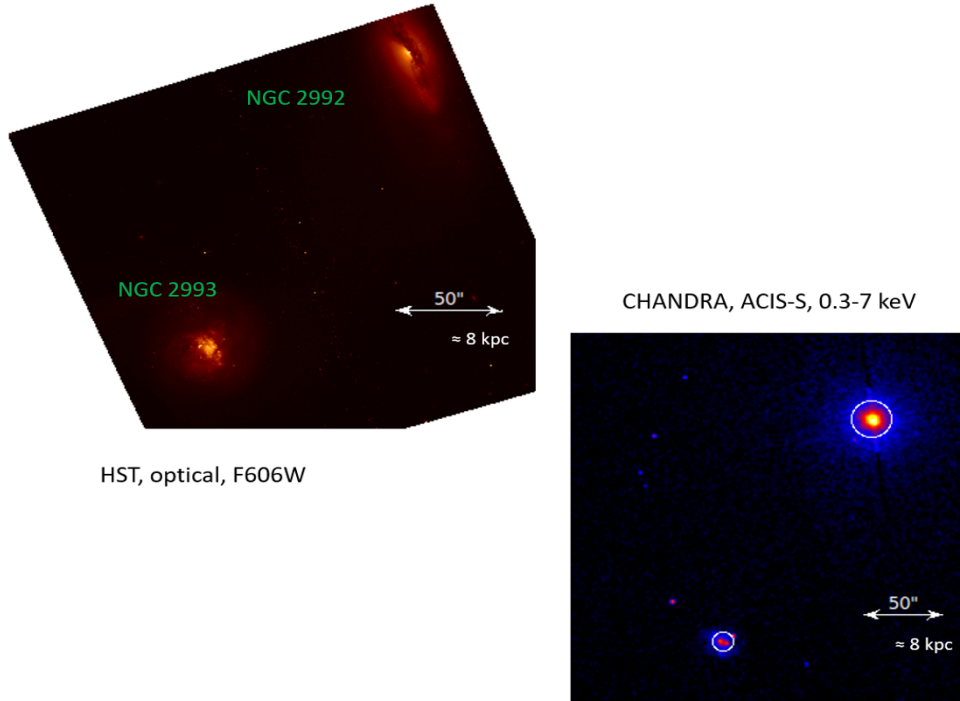


Figure 4.21: On the left, the HST image of Arp 245 with the F606W filter is shown, while on the right the Chandra image in the 0.3-7 keV band of the same region is presented.

Arp 245 is an interacting galaxy system composed of two primary galaxies: NGC 2992 and NGC 2993. This system, located at $z=0.0077$, is in interaction and forms an interacting galaxy system characterized by extended tidal features visible in optical images. In the mid-ultraviolet (MUV) spectrum, NGC 2992 exhibits faint and diffuse emission corresponding to its optical central bulge and disk, with minimal internal color variation. This galaxy appears very dim in the far-ultraviolet (FUV) images.

NGC 2993 is prominently visible in both FUV and MUV images taken by the Ultraviolet Imaging Telescope (UIT). Notably, NGC 2993 displays one of the bluest UV-optical colors among the UIT sample, indicating intense star formation. These newly formed stars are the primary contributors to the galaxy's ultraviolet SED. The uniformity in color between the MUV and optical images suggests that the young stars also significantly influence the emission in these wavelengths (Papovich et al. 2003).

In the X-rays, this galaxy has no previous information, the main results from Chandra spectral data are reported below (this component has only Chandra observation, while for his companion NGC 2992 there are also XMM and NuSTAR observation).

The photon index Γ suggests a moderately soft X-ray spectrum, indicative of non-

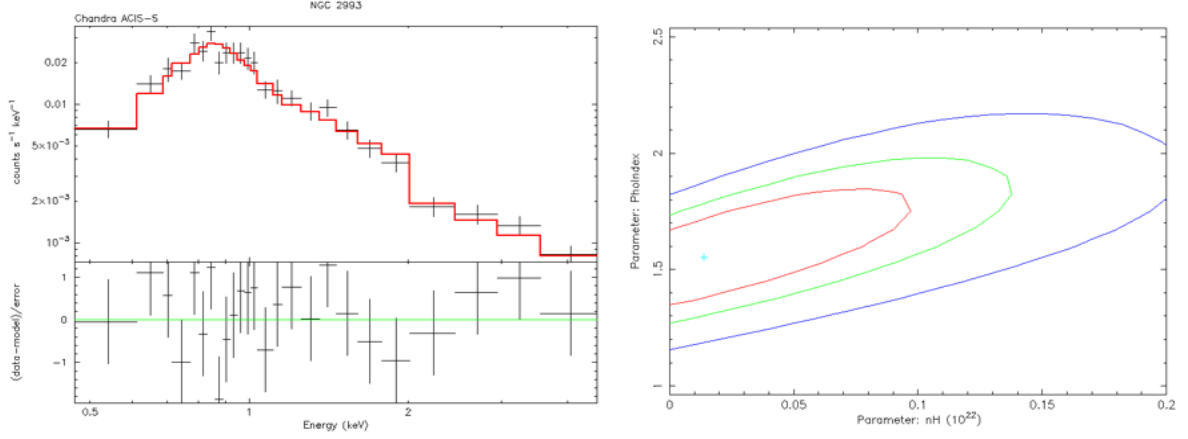


Figure 4.22: The left panel shows the best fit of the Chandra NGC 2993 spectra, while the right panel presents the $N_{\text{H}}(z)$ - Γ contour plot. The confidence levels are the same as Fig. 4.5.

NGC 2993	
Model	b.
Statistics	$\frac{\chi^2}{\text{d.o.f.}} = \frac{28.9}{34}$
Γ	$1.55^{+0.32}_{-0.18}$
$N_{\text{H}}(z)$	< 0.10
kT	$0.64^{+0.05}_{-0.06}$
F_{2-10}	$-13.03^{+0.08}_{-0.11}$
L_{2-10}	$40.08^{+0.09}_{-0.11}$

Table 4.10: Main spectral parameters of Chandra spectra of NGC 2993. All errors are reported at the 90% of confidence level.

thermal emission, the neutral hydrogen column density is constrained to be less than 10^{21} cm^{-2} , indicating minimal X-ray absorption along the line of sight. The thermal component of the spectrum is characterized by $kT \sim 0.64$ keV, with a small uncertainty. This suggests the presence of hot gas, which may be associated with the galaxy’s environment, such as a cooling flow or material heated by the AGN or star formation activity.

The flux and luminosity values indicate that the X-ray emission is unlikely to be associated with an AGN (see Tab 4.10). Instead, it is more plausibly attributed to processes linked to active star formation or an unresolved population of X-ray binaries.

Conversely, NGC 2992 is optically classified as a Seyfert 1.9 galaxy (Ward et al. 1980), indicating it has an AGN which is extinguished in the UV/optical band, features typical of Seyfert 1 galaxies and broad emission lines visible in the infrared spectrum. The interaction with NGC 2993 has led to tidal distortions, including a prominent tidal tail and a bridge of material connecting the two galaxies. These features are indicative of past gravitational interactions that have disturbed the galaxy’s structure.

NGC 2992 has been extensively studied in X-rays, providing insights into the activity in its nucleus. The galaxy shows strong X-ray emission from its core, which is attributed to the AGN. The X-ray emission is variable, highlighting X-ray flux variability on timescales ranging from hours to months (Middei et al. 2022), which is common in AGN and is likely due to changes in the accretion rate onto the supermassive black hole (Colbert et al. 2005a), although variability in the column density may be present as well (see also section 4.6).

Extended soft X-ray emission has been observed in the circumnuclear region of NGC 2992. This emission extends asymmetrically from the nucleus and is more prominent in the soft X-ray band (0.3–2 keV). The extended emission is believed to be the result of shock heating of gas in the galaxy’s central region due to the interaction and AGN activity (Murphy et al. 2017).

The X-ray and radio activity of NGC 2992 has been associated with flares generated by magnetic reconnection events in the accretion disk. These flares can trigger outbursts of ionized material, resulting in an overall increase in brightness in the hard X-ray spectrum (Fernandez et al. 2022).

For this galaxy, observations from Chandra (2003), XMM, and NuSTAR (both in 2019) were available. The main results from the spectral analysis are reported below.

It should be noted that the spectral analysis of Chandra data was complex because, unlike NGC 2993, NGC 2992 is affected by significant pileup (over 60%). Therefore, it was necessary to introduce a pileup component (`pileup` model, an implementation of the fast pile-up algorithm proposed by John Davis)¹ in front of the spectral model used in the analysis in `XSPEC`. The main parameters of this model are the PSF fraction (the fraction of counts in the region that are from the point source whose pileup is being modeled), set

¹more information on <http://space.mit.edu/~davis/papers/pileup2001.pdf>

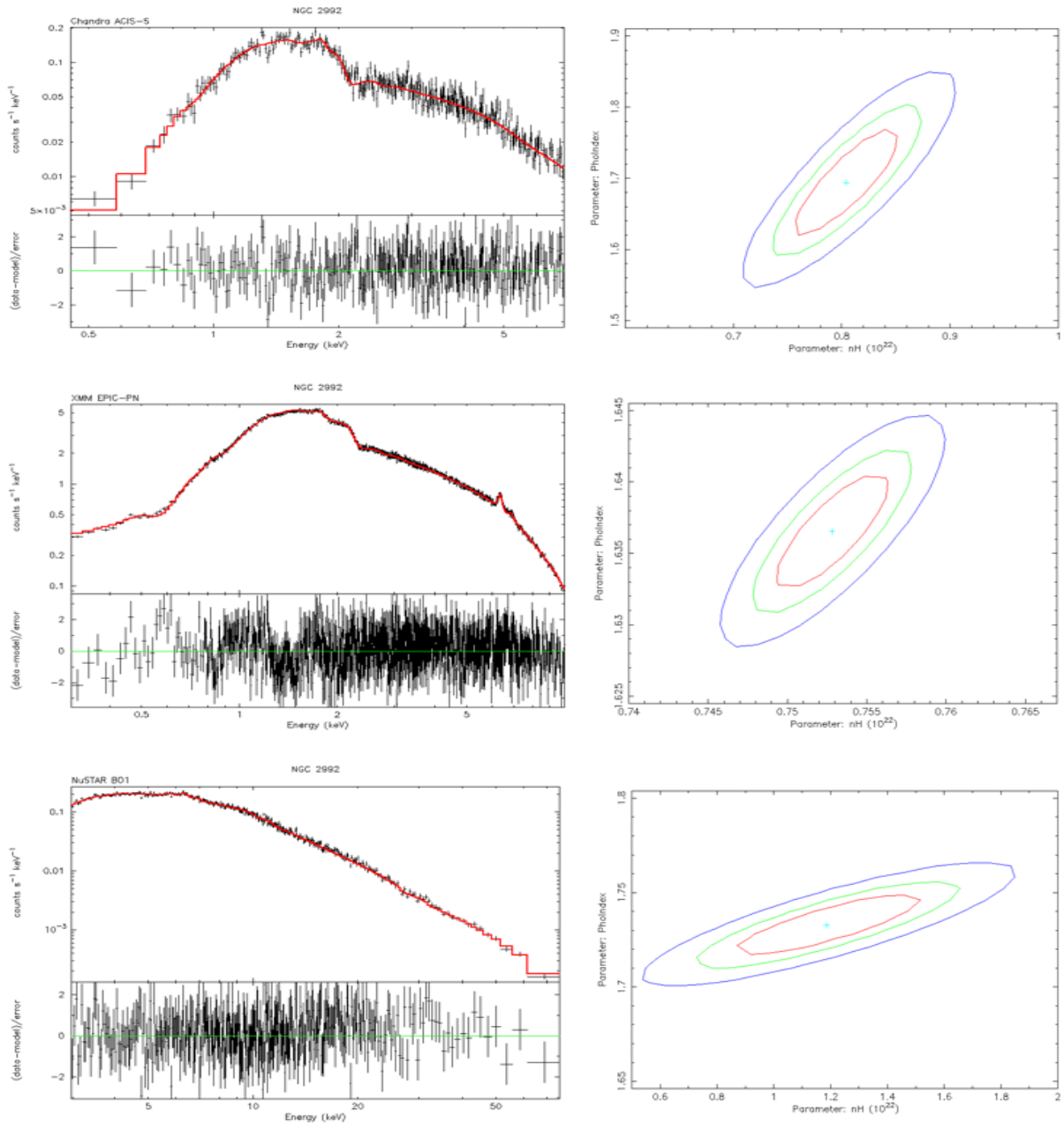


Figure 4.23: The left panel shows the best fit of the Chandra, XMM, and NuSTAR spectra of NGC 2992, from top to bottom. The right panel presents the $N_H(z)$ - Γ contour plot, with confidence levels equal to Fig. 4.5.

at a value of 85%, and the α parameter (grade correction for single photon detection)², which was found to be $\alpha = 0.83_{-0.04}^{+0.04}$. It can also be inferred from the Chandra spectrum that, in this case, no iron line is detected.

	CHANDRA	XMM	NUSTAR
Model	pileup*b	g.	b.
Statistics	$\frac{\chi^2}{\text{d.o.f.}} = \frac{373.3}{346}$	$\frac{\chi^2}{\text{d.o.f.}} = \frac{2307.9}{1932}$	$\frac{\chi^2}{\text{d.o.f.}} = \frac{653.7}{670}$
Γ	$1.69_{-0.08}^{+0.08}$	$1.64_{-0.01}^{+0.01}$	$1.73_{-0.02}^{+0.02}$
$N_{\text{H}}(z)$	$0.80_{-0.05}^{+0.05}$	$0.75_{-0.01}^{+0.01}$	$1.19_{-0.36}^{+0.36}$
Line E, EQW		$6.39_{-0.01}^{+0.01}, 0.08_{-0.01}^{+0.01}$ $6.91_{-0.03}^{+0.04}, 0.02_{-0.01}^{+0.01}$	$5.84_{-0.11}^{+0.12}, 0.03_{-0.01}^{+0.02}$ $6.38_{-0.05}^{+0.05}, 0.08_{-0.01}^{+0.02}$ $6.93_{-0.12}^{+0.12}, 0.03_{-0.01}^{+0.02}$
F_{2-10}	$-10.59_{-0.03}^{+0.03}$	$-10.04_{-0.01}^{+0.01}$	$-10.00_{-0.01}^{+0.01}$
L_{2-10}	$42.53_{-0.03}^{+0.03}$	$43.08_{-0.01}^{+0.01}$	$43.11_{-0.01}^{+0.01}$

Table 4.11: Main spectral parameters of Chandra, XMM and NuSTAR spectra of NGC 2992. All errors are reported at the 90% of confidence level. Note that for the calculation of the X-ray flux and luminosity for the Chandra telescope it was necessary to remove the pileup component, and as an error 10% of the error on the count rate for these two quantities was considered.

The X-ray data from Chandra, XMM, and NuSTAR for NGC 2992 reveal a consistent picture of the active galactic nucleus. All three instruments show a similar soft X-ray spectrum, indicating non-thermal emission typically associated with an AGN. The photon index Γ from the three instruments are close to each other, ranging from 1.64 to 1.73, suggesting that the X-ray emission mechanism is consistent across all observations.

²In XSPEC, the grade correction parameter α in the pileup model represents the probability that a piled-up event retains its original grade rather than being misclassified or rejected. In X-ray CCD detectors, photon events are categorized by grades based on pixel charge distribution, which helps distinguish real X-ray photons from background noise. When pileup occurs, multiple photons interact within the same detector pixel in a single readout frame, increasing the chance of grade misclassification. The parameter α corrects for this effect, where $\alpha=1$ implies no grade migration, while $\alpha=0$ assumes complete misclassification.

In terms of absorption, the neutral hydrogen column density varies slightly between instruments: Chandra and XMM show similar values ($0.75\text{-}0.80 \cdot 10^{22} \text{ cm}^{-2}$), while NuSTAR is slightly higher at $1.19 \cdot 10^{22} \text{ cm}^{-2}$. However, all values are consistent within $\sim 2\sigma$.

The iron $K\alpha$ line, a key feature often associated with the accretion disk around a supermassive black hole, is present in XMM and NuSTAR data, but not revealed with Chandra (maybe because the extraction band of the Chandra spectrum is at the limit for the iron line's detection). The line energy is consistent across the instruments, with small variations. The equivalent width of the line also remains quite stable across the observations, indicating that the iron emission is a stable feature of the source.

Looking at the flux, the values are also consistent across XMM and NuSTAR but slightly lower in Chandra, also reflected in the X-ray luminosity, by about a factor of 0.5. This is most likely due to the fact that the XMM and NuSTAR observations are temporally close (same year, 2019, but different months), while the Chandra observation dates back to 2003. Given that NGC 2992 is a highly variable X-ray source, this could indicate that during the Chandra observation, the central AGN was experiencing a period of lower X-ray emission.

Furthermore, a historical behavior (in terms of photon index, absorption column density and hard X-ray flux) of this galaxy is reported in section 4.6.

4.4.10 AM 2048-571

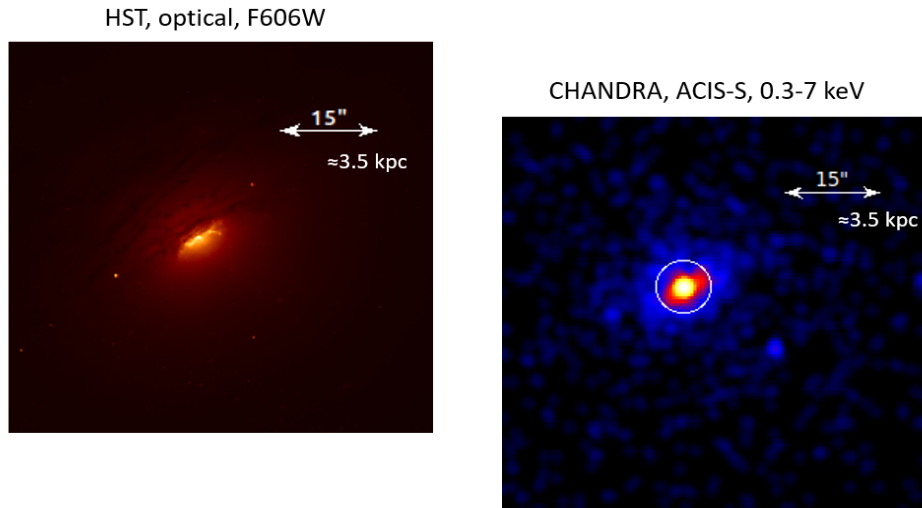


Figure 4.24: On the left, the HST image of AM 2048-571 with filter F606W is depicted, while on the right the Chandra 0.3-7 keV image of the same region is shown.

This system, also called IC 5063, is a Seyfert 2 galaxy situated at redshift $z=0.011$ in the constellation Indus. It is a critical object of study for exploring the interaction

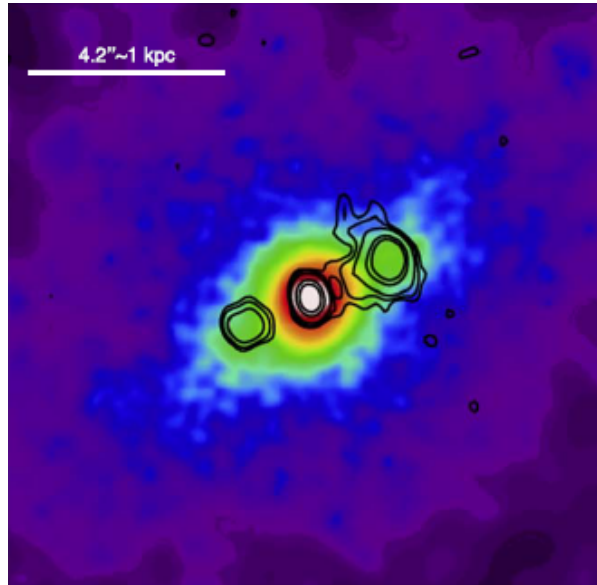


Figure 4.25: This figure shows the X-ray emission of IC 5063 in the 0.3-7 keV band from the Chandra telescope. The black contours represent the radio emission observed with ATCA at 17 GHz. From Travascio et al. [2021a](#).

between AGN, radio jets, and their surrounding environments (Mukherjee et al. [2018](#)). Its X-ray emission, analyzed extensively through observatories like Chandra, ROSAT, and ASCA, provide rich insights into the dynamics of AGN-driven processes.

X-ray studies of IC 5063 reveal a complex spectrum. The soft X-ray emission (<3 keV) is interpreted as arising from a combination of photoionized gas and collisionally ionized gas, indicative of interactions between the galaxy’s powerful radio jets and its interstellar medium (ISM). These jets create clumpy, filamentary structures observable in soft X-rays along the jet trails, suggesting significant heating and displacement of gas due to jet-ISM collisions. This phenomenon has been highlighted in Travascio et al. [2021a](#), who noted that these interactions not only shape the ISM but also generate extensive outflows, potentially influencing star formation and galaxy evolution.

The hard X-ray component (>3 keV) is dominated by a continuum emission and a prominent Fe $K\alpha$ line at 6.4 keV. This line is thought to result from reflection off dense molecular clouds or a dusty torus near the AGN. Travascio et al. [2021a](#) also reported that these emissions are spatially extended along the galaxy’s bicone, which aligns with the AGN’s radiation field, further supporting a scenario where nuclear photons illuminate nearby dense gas.

Earlier studies, such as those using the ASCA and ROSAT observatories, identified a “soft excess” component in the X-ray spectrum, alongside evidence for anisotropic radiation escaping the torus. This soft component likely includes scattered emission

from ionized gas above the torus, consistent with IC 5063's Seyfert 2 classification. A dual-power-law model combined with a reflection component best fits the observed data, highlighting the complexity of the galaxy's X-ray emissions (Caldwell et al. 1981).

The X-ray morphology also strongly correlates with the radio structure of IC 5063. The northwest cone, for instance, exhibits Fe XXV emission spatially aligned with intense radio hotspots, a direct indication of jet-induced shock heating (Travascio et al. 2021a).

The available data for this galaxy were obtained from Chandra (2007) and NuSTAR (2013), with the main results from the spectral analysis summarized below.

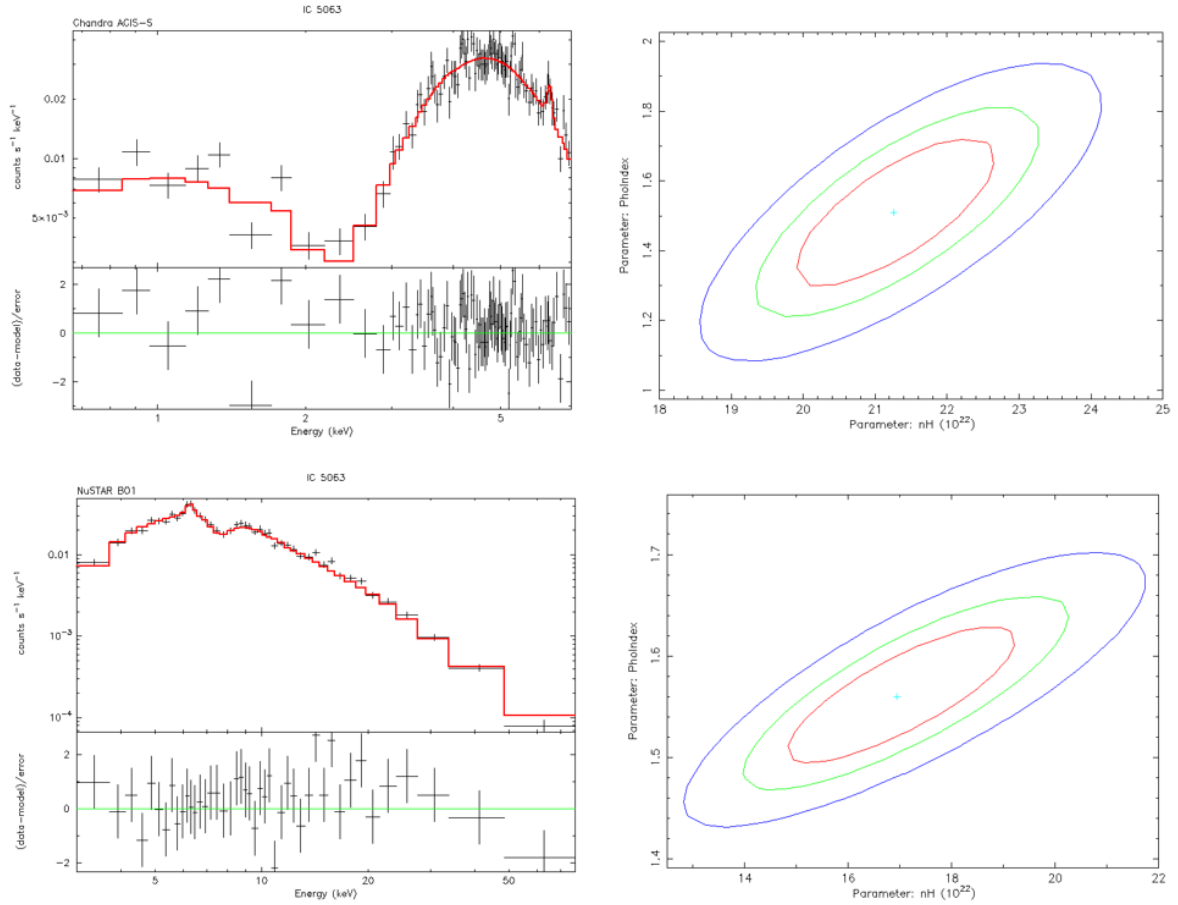


Figure 4.26: On the left panel, the best fit of Chandra and NuSTAR spectra of IC 5063 is shown. On the right panel it is reported the $N_{\text{H}}(z)$ - Γ contour plot; the codex color is the same as Fig. 4.5.

It is worth noting that for the NuSTAR spectral analysis, the inclusion of the `gabs` parameter was necessary. In XSPEC, the model `gabs` is used to model broad absorption features in the X-ray spectrum. Specifically, it represents a broad absorption line by using a Gaussian function, which is particularly useful when fitting spectra of sources

	CHANDRA	NUSTAR
Model	c	gabs*f
Statistics	$\frac{\chi^2}{\text{d.o.f.}} = \frac{151.4}{132}$	$\frac{\chi^2}{\text{d.o.f.}} = \frac{173.4}{194}$
Γ	$1.51^{+0.23}_{-0.23}$	$1.56^{+0.07}_{-0.07}$
$N_{\text{H}}(z)$	$21.26^{+1.54}_{-1.49}$	$16.94^{+2.51}_{-2.31}$
Line E, EQW	$6.36^{+0.05}_{-0.05}, 0.07^{+0.05}_{-0.04}$	$6.35^{+0.08}_{-0.07}, 0.19^{+0.08}_{-0.07}$
F_{2-10}	$-10.92^{+0.03}_{-0.03}$	$-10.66^{+0.04}_{-0.04}$
L_{2-10}	$42.51^{+0.03}_{-0.03}$	$42.76^{+0.04}_{-0.04}$

Table 4.12: Main spectral parameters of Chandra and NuSTAR spectra of IC 5063. All errors are reported at the 90% of confidence level.

with broad, unresolved absorption features. The main parameters obtained for this component are as follows: the central energy $E = 7.76^{+0.23}_{-0.25}$ keV of the absorption feature, the width $\sigma = 0.35^{+0.32}_{-0.23}$ keV of the Gaussian, and the line depth $d = 0.27^{+0.15}_{-0.13}$ keV (which corresponds to the strength of the absorption).

The addition of this model was evaluated using the F-test, which indicated that the inclusion of this component is statistically significant at $\sim 2.6\sigma$. At 7.76 keV, the absorption could be attributed to blueshifted Fe XXV or Fe XXVI K-shell transitions, which would suggest the presence of high-velocity outflows moving away from the central AGN, i.e. UFOs.

Unfortunately, there are no specific references in the literature discussing this absorption feature at 7.76 keV in IC 5063. However, similar features have been observed in other Seyfert galaxies and AGN, often linked to relativistic outflows or highly ionized absorption due to Fe XXV-XXVI transitions (Tombesi et al. 2010, Gofford et al. 2013).

The X-ray data for IC 5063 from both Chandra and NuSTAR reveal that both instruments provide similar results for the photon index Γ .

The column density of neutral hydrogen, which measures the amount of material absorbing the X-ray emission, shows some differences between the data from Chandra and NuSTAR. The distance between the two values in units of sigma is $\sim 2.5\sigma$, indicating that they are moderately consistent with each other.

The iron line was detected in both telescopes. The two measurements are consistent

with each other, with the line energy showing excellent agreement, while the equivalent width exhibits a slight difference ($\sim 2\sigma$), which remains within an acceptable statistical range. These results confirm the presence of an active AGN, with negligible variations in the line energy and only a minor difference in the equivalent width.

The X-ray luminosities obtained from spectral analysis are consistent with AGN emission in the Seyfert regime. With values around 10^{42-43} erg/s, they fall within the typical range for Seyfert galaxies, distinguishing the source from purely star-forming processes or LINER-like emission.

Finally, an historical behavior in terms of photon index, absorption column density and observed X-ray flux is also briefly discussed for IC 5063 in section 4.6.

4.5 Undetected X-ray sources

Unfortunately, some of the sources within the sample were not detected by the respective X-ray detection tools, in particular 2 for Chandra and 4 for XMM. This could be due to various factors, such as the low X-ray emission from these galaxies, a short exposure time insufficient to collect enough counts, or because these sources are located far from the aim-point of observation (e.g. Arp 100 system). For these sources, whenever possible, it was necessary to estimate an upper limit on the observed flux, which could then be converted into an X-ray luminosity. These constraints allow us to rule out the presence of bright AGN but do not exclude lower-luminosity, highly obscured sources. The procedure to achieve this differed for the non-detected targets in Chandra and XMM, as will be explained below.

4.5.1 Chandra

Regarding the Chandra telescope, two targets were not detected: specifically, the second galaxy in the AM 2026-424 system, ESO285-G019 east (see 4.12) and AM 0642-801 companion, WISEA J063828.58-801458.0 (see 4.4.2). In this case, it was necessary to use a tool from the CIAO software called `aprates`.

The `aprates` tool is designed to compute values and limits for source quantities, such as net counts, source rate, photon flux, and energy flux, based on counts and exposure data obtained from source and background apertures. To determine the intensity values, the tool solves a pair of simultaneous linear equations:

$$n = f * S + b \tag{4.7}$$

$$m = g * S + r * b \tag{4.8}$$

The total counts observed in the source and background apertures, represented by n and m respectively, are used to estimate the intensity quantity S . In these equations,

b represents the background counts in the source aperture, while the quantities f and g describe the fractions of the source point response function contained in the source and background apertures, but, depending on the intensity quantity of interest, may also include factors that convert the intensity quantity S into counts. Additionally, the parameter r is the “backscale” factor, which scales the background counts from the source aperture to the background aperture. The tool calculates the values of f, g, and r based on more fundamental input data: in this specific case, the number of counts in the source and background apertures (n=5, m=8), their geometric areas in pixel² ($A_s = 43.3$, $A_b = 379.3$), their PSF fractions ($\alpha = 0.955$, $\beta = 0.025$)³, and the exposure time (approximately 9.9 ks) were considered.

To estimate credible intervals for the source intensity, the tool applies a Bayesian approach, specifically calculating the background-marginalized posterior probability distribution function (PDF) for the intensity quantity S. This calculation assumes non-informative priors for the intensities in both the source and background apertures. The mode of the PDF is identified, and the lower and upper bounds of the credible interval are then determined by accumulating the values of the PDF above and below the mode until the desired confidence level is achieved. Since this method is fully Bayesian, the term “credible interval” is used instead of “confidence interval,” which is associated with frequentist statistics.

This approach allows the tool to account for uncertainties and provides a probabilistic estimate of net source counts: $\text{cts-rate} < 4.3 \cdot 10^{-4}$ cts/s.

Once this value was obtained, an online tool called PIMMS (Portable, Interactive Multi-Mission Simulator) was used to convert the derived count rate into an observed flux. By setting the main parameters, such as redshift ($z=0.05$), Galactic absorption ($N_H = 5.29 \cdot 10^{20}$ cm⁻²), and the spectral index ($\Gamma=1.8$), the tool provided the flux value in the selected 2–10 keV band based on the previously calculated count rate:

$$\log(F_{(2-10)\text{keV}}/\text{erg}/\text{cm}^2/\text{s}) < -14.3 \quad (4.9)$$

This value can finally be quantified in terms of X-ray luminosity through the formula:

$$L = 4\pi D^2(1+z)^{\Gamma-2}F \quad (4.10)$$

where D identifies the distance in parsec of the galaxy. From which the following is derived:

$$\log(L_{(2-10)\text{keV}}/\text{erg}/\text{s}) < 40.5 \quad (4.11)$$

The same procedure was performed for the galaxy WISEA J063828.58-801458.0, yielding the values n=35, m=230, $A_s=324.5$, $A_b=3331.5$, $\alpha=0.927$, and $\beta=0.031$, with

³ α is the PSF fraction of the source within the chosen region, while β is the PSF fraction of the source in the background region.

an exposure time of approximately 38.5 ks. Using the `aprates` tool, an estimate of the net source counts was obtained: $\text{cts-rate} < 3.5 \cdot 10^{-4}$ cts/s.

Next, using PIMMS, by setting $\Gamma=1.8$, using the spectroscopic redshift of AM 0642-801 ($z=0.016$), and a column density N_{H} of $1.1 \cdot 10^{21}$ cm^{-2} , it is possible to convert the net count rate into a flux value in the 2–10 keV band:

$$\log(F_{(2-10)\text{keV}}/\text{erg}/\text{cm}^2/\text{s}) < -14.4 \quad (4.12)$$

And the luminosity in the same band:

$$\log(L_{(2-10)\text{keV}}/\text{erg}/\text{s}) < 39.4 \quad (4.13)$$

4.5.2 XMM

For XMM, upper limits are computed using a sensitivity estimator based on the Flux Limits from Images from XMM-Newton (FLIX) tool. The main purpose of FLIX is to produce estimates of the detection threshold of the X-ray flux at a given point in the sky.

The tool operates by scanning the 4XMM catalog and listing the closest sources to the specified position. The latest version of the catalog, 4XMM-DR12 at the time of writing, has been incorporated into the sensitivity estimator.

The main input parameters are the position of the target of interest, the detection likelihood threshold for detection threshold estimation (in this work, this value is chosen equal to 6, corresponding at $\sim 3\sigma$) and the radius of the circle in arcsec used for the flux estimation, taking a value of 5 arcsec. The selected energy band to obtain flux upper limits is band 7 (approximately, the sum of 4 and 5 bands of the standard EPIC energy bands)⁴, corresponding to a range of 2-12 keV, values then converted to 2-10 keV using the conversion factor of 0.88 from a power law.

Sensitivity estimates are empirically derived by following the algorithm described in Carrera et al. 2007. These calculations utilize the detector mask to identify valid pixels in the image, the exposure map data to determine the exposure time, and the background map to measure the fitted background level. If a source is present at the designated position, the flux is computed by summing the counts within the user-defined radius (in this work 5 arcsec), incorporating the background level from the background map data and an approximation of the point-spread function from the calibration files. The applied energy conversion factors are consistent with those used in the 4XMM catalog (Webb et al. 2020).

The formula used to calculate the flux is as follows:

$$FEST = \frac{IMCIRC - BGCIRC}{TEXPOS * ECF * EEF} \quad (4.14)$$

⁴more information on <http://flix.irap.omp.eu/docs/>

where IMCIRC and BGCIRC are the sum of image counts and image background counts in the circle of the chosen radius (note that IMCIRC and BGCIRC values result from summing flux and background only for valid pixels, i.e. pixels in chip gaps or other places where the EPIC Detection Mask is zero are simply ignored): TEXPOS is exposure time (sec) averaged over the circle radius CUTRAD, the radius in pixel (4arcsec/pixel) which optimises the flux-limit estimated for each energy band (for band 7 the CUTRAD corresponds to a value of 5.7); finally ECF is the energy conversion factor (cts cm² ergs⁻¹) and EEF the encircled energy fraction within the circle of radius set.

Arp255 (UGC 05304a)

The second component of system Arp255 (see 4.4.7), for UGC 05304a FLIX has derived an upper limit flux of $8.4 \cdot 10^{-15}$ erg/cm²/s in band 7, corresponding to a value in logarithm in the 2-10 keV band of

$$\log(F_{(2-10)keV}/erg/cm^2/s) < -14.1 \quad (4.15)$$

From which using the 4.10 relation gives a luminosity of

$$\log(L_{(2-10)keV}/erg/s) < 40.4 \quad (4.16)$$

WISEA J063828.58-801458.0

The companion of AM 0642-801 (see 4.4.2), for this galaxy FLIX has detected an u.l. on the flux in band 7, equal to $1.5 \cdot 10^{-14}$ erg/cm²/s, which, when converted to a logarithmic value, corresponds to a flux in the 2–10 keV band of

$$\log(F_{(2-10)keV}/erg/cm^2/s) < -13.9 \quad (4.17)$$

This value in terms of luminosity becomes (using 4.10)

$$\log(L_{(2-10)keV}/erg/s) < 40.0 \quad (4.18)$$

Arp 100

Arp 100 is a pair of interacting galaxies, IC 0018 and IC 0019, classified as spiral with elliptical galaxy companion. IC 0018 was likely an Sb-type spiral galaxy before its close encounter with IC 0019.

This system is located at redshift $z=0.02$, and there is no X-ray information available.

FLIX evaluated a flux for this pair of interacting galaxies respectively of $9.2 \cdot 10^{-14}$ erg/cm²/s for IC 0018 and $8.8 \cdot 10^{-14}$ erg/cm²/s for IC 0019 (always in band 7), from which derive a flux in band (2-10)keV of

$$\log(F_{(2-10)keV}/erg/cm^2/s) < -13.1 \quad \text{IC 0018} \quad \text{and} \quad \text{IC 0019} \quad (4.19)$$

In terms of X-ray luminosity in 2-10 keV band, they become

$$\log(L_{(2-10)keV}/erg/s) < 40.9 \quad \text{IC 0018} \quad \text{and} \quad \text{IC 0019} \quad (4.20)$$

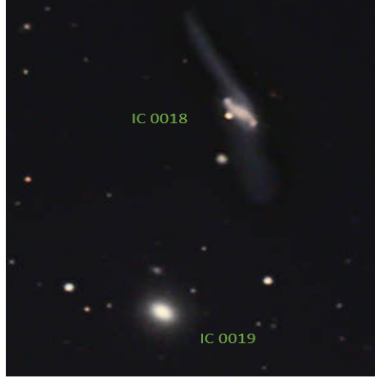


Figure 4.27: An HST view of Arp 100 system.

IC 0267

IC 0267 is a spiral galaxy, located at $z=0.012$, that is currently undergoing an interaction with Arp 200 (a.k.a. NGC 1134, see 4.16). For this galaxy FLIX evaluated a flux u.l. in band 7 of $6.1 \cdot 10^{-14}$ erg/cm²/s, corresponding to a value in logarithm in the 2-10 keV band of

$$\log(F_{(2-10)keV}/erg/cm^2/s) < -13.3 \quad (4.21)$$

This value in terms of luminosity becomes (using 4.10)

$$\log(L_{(2-10)keV}/erg/s) < 40.2 \quad (4.22)$$

The upper limits to the X-ray luminosities, ranging from 39.4 to 40.9 erg/s, suggest that these sources may belong to the category of low-luminosity AGN, especially IC 0018 and IC 0019. However, these galaxies are most likely experiencing a period of intense star formation, making them probably classifiable as SF galaxies.

4.6 More consideration about IC 5063 and NGC 2992

In this session, further considerations are made regarding the two most well-known galaxies, NGC 2992 and IC 5063, by comparing X-ray analysis data with findings from other scientific studies. Long-term X-ray observations of these galaxies reveal significant variability in flux (in the 2-10 keV band), absorption column density (N_H), and photon index Γ . These variations offer crucial insights into the accretion process, the nature of the obscuring medium, and potential AGN feedback mechanisms.

4.6.1 IC 5063

Over the past decades, X-ray observations of IC 5063 have revealed significant variability in flux, absorption column density and Γ , highlighting the complex nature of its AGN.

The GINGA observation in 1990 (Koyama et al. 1992) recorded one of the highest flux levels, indicative of strong AGN activity. However, by the time of the Chandra analysis in 2007, the flux had significantly decreased, suggesting either a decline in the accretion rate or an increase in obscuration along the line of sight. A further drop was recorded in 2009 with Suzaku and Swift-BAT observations (Tazaki et al. 2011), consistent with a period of reduced AGN emission or a phase of heightened obscuration. Interestingly, the NuSTAR analysis in 2013 showed a slight flux recovery, potentially due to an increased contribution from hard X-ray photons capable of penetrating deeper into the obscuring material. Furthermore, the differences in flux do not always directly correlate with Γ or N_{H} , suggesting that the variability could be driven by intrinsic changes in the AGN's activity rather than just absorption effects.

The evolution of absorption in IC 5063 appears highly dynamic. The GINGA (1990) and ASCA/ROSAT (1991–92) observations (Vignali et al. 1997) indicated moderate absorption levels, suggesting a relatively clear line of sight. However, by the time of the Chandra (2007) analysis, significant variability in N_{H} was observed, implying the possible movement of denser clouds into the observer's line of sight. The Suzaku and Swift-BAT (2009) measurement showed an even larger column density, reinforcing the idea that the AGN was undergoing a phase of increased obscuration. The NuSTAR (2013) analysis then indicated a lower value, possibly due to the temporary clearing of the obscuring material, or is it due to the fact that NuSTAR operates over a spectral range toward hard X-rays that are less affected by obscuration. However, the Chandra (2018) observation (Travascio et al. 2021b) recorded the highest N_{H} to date, suggesting a highly dynamic torus structure in which clouds of gas and dust continuously drift in and out of view.

The photon index Γ of IC 5063 also exhibits considerable variability. The GINGA (1990) observation recorded a relatively low $\Gamma \sim 1.5$, indicative of a harder spectrum, possibly due to moderate absorption or a strong Compton reflection component. By 2007, Chandra data showed significant scatter, likely a result of increased variability in obscuration. The Suzaku/Swift-BAT (2009) observations suggested a slightly softer spectrum ($\Gamma \sim 1.75$), which could indicate a clearer line of sight or an accretion state with higher radiative efficiency. However, both the NuSTAR (2013) and Chandra (2018) observations recorded lower Γ values once again, suggesting either an increase in obscuration or a larger contribution from reflected X-ray emission.

There are some possible connections between the different X-ray parameters observed in IC 5063 over time. The increase in obscuration detected in the Chandra (2018) observation coincides with a harder spectral shape, suggesting that higher absorption may be affecting the observed emission. This could indicate the presence of dense gas or

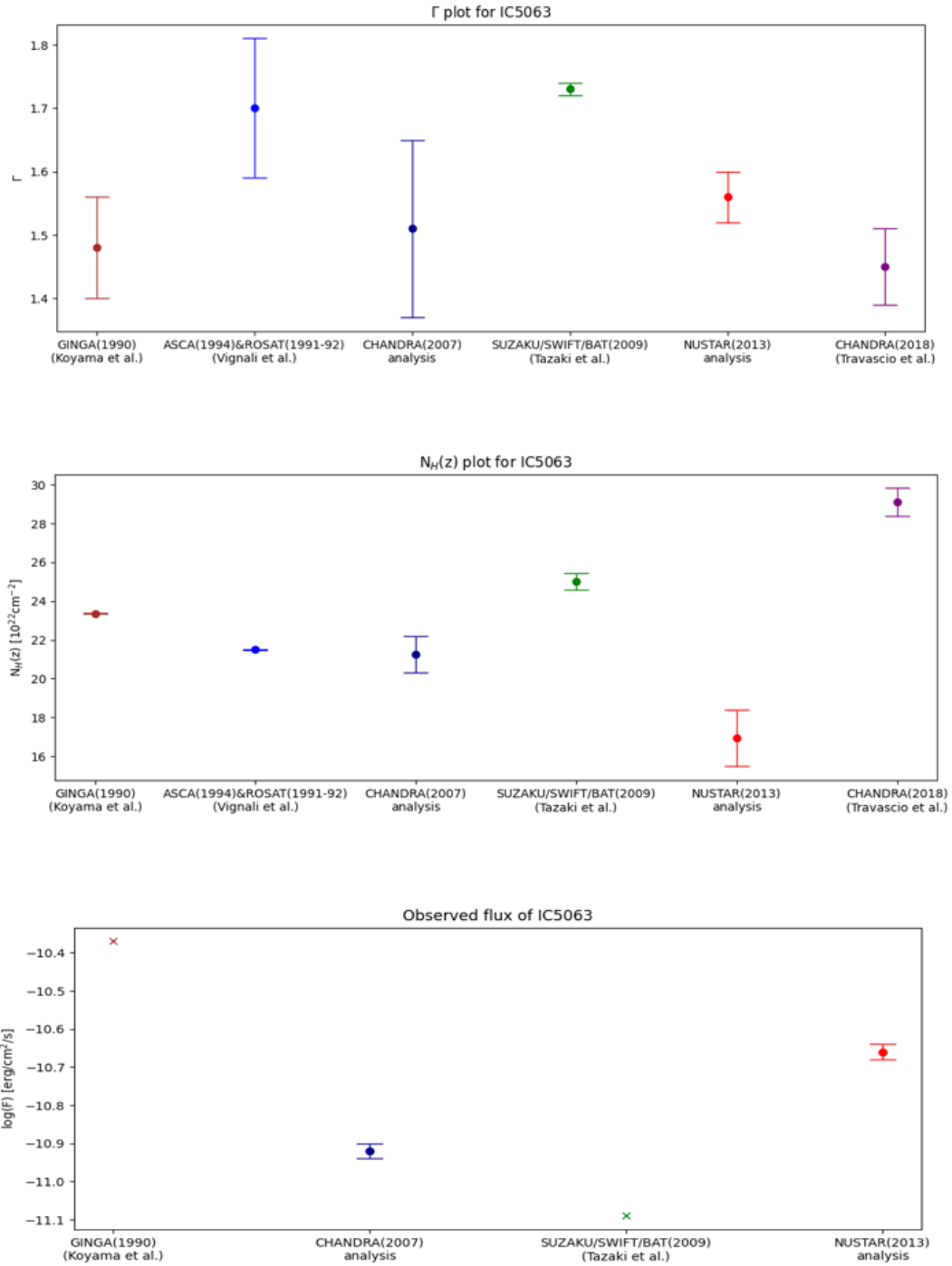


Figure 4.28: These plots show the temporal evolution of the main parameters of IC 5063: spectral index, intrinsic absorption, and observed flux in 2-10 keV band. X-ray analysis results are compared with data from different time periods reported in various studies.

dust moving into the line of sight, altering the way the X-ray photons reach us.

Furthermore, the observed flux varies between different observations, which could be the result of intrinsic changes in the activity of the AGN or variations in the amount of obscuring material. These trends suggest that both the emission from the central engine and the environment around it are highly dynamic, influencing the overall X-ray properties of IC 5063.

4.6.2 NGC 2992

NGC 2992 exhibits pronounced flux variability over the decades, with observations ranging from HEAO1 (1977–78) by Mushotzky et al. 1980 to XMM and NuSTAR (2019) by Middei et al. 2022. The BeppoSAX observations (Gilli et al. 2000) recorded a significant flux drop compared to earlier data, suggesting a phase of reduced AGN activity. However, Chandra (2003) observations indicated that the AGN remained active, and the subsequent XMM (2003) study (Shu et al. 2010) revealed a flux increase, possibly marking the beginning of a reactivation phase. By 2019, NuSTAR and XMM observations confirmed that the AGN had regained significant luminosity, highlighting the highly dynamic nature of its central engine.

The comparison between different observations suggests a possible connection between the flux changes and spectral parameters, with a brighter state often associated with a softer spectrum. This could be indicative of variations in the accretion rate or changes in the geometry of the absorbing material around the nucleus.

The absorption variability in NGC 2992 follows a similar pattern. The HEAO1 (1977–78) data (Mushotzky et al. 1980) reported a relatively high absorption column density, which gradually decreased in subsequent observations. SAX2 (1998) and CHANDRA (2003) measurements indicated significantly lower N_{H} , suggesting that the obscuring material had thinned out, allowing for a clearer view of the AGN. However, in 2019, NUSTAR observations recorded an increase in N_{H} , which might indicate temporary changes in the surrounding material. If this increase in obscuration coincides with spectral hardening, it could suggest that the source is undergoing phases of higher absorption due to clumpy material moving across the line of sight.

The photon index Γ in NGC 2992 also exhibits considerable variability, reflecting changes in both obscuration and accretion. The HEAO1 (1977–78) data suggested a typical AGN photon index of ~ 1.8 . The Chandra (2003) study (Colbert et al. 2005b) recorded the highest Γ value ($\Gamma \sim 1.85$), suggesting a very soft spectrum, likely caused by a temporary reduction in obscuration, but it must be noted that this observation is affected by pileup so this value may not be entirely reliable. In contrast, the NuSTAR (2019) analysis revealed a lower Γ (< 1.75), which could indicate a reflection-dominated state. This variability could be associated with changes in the accretion process or intermittent obscuration events.

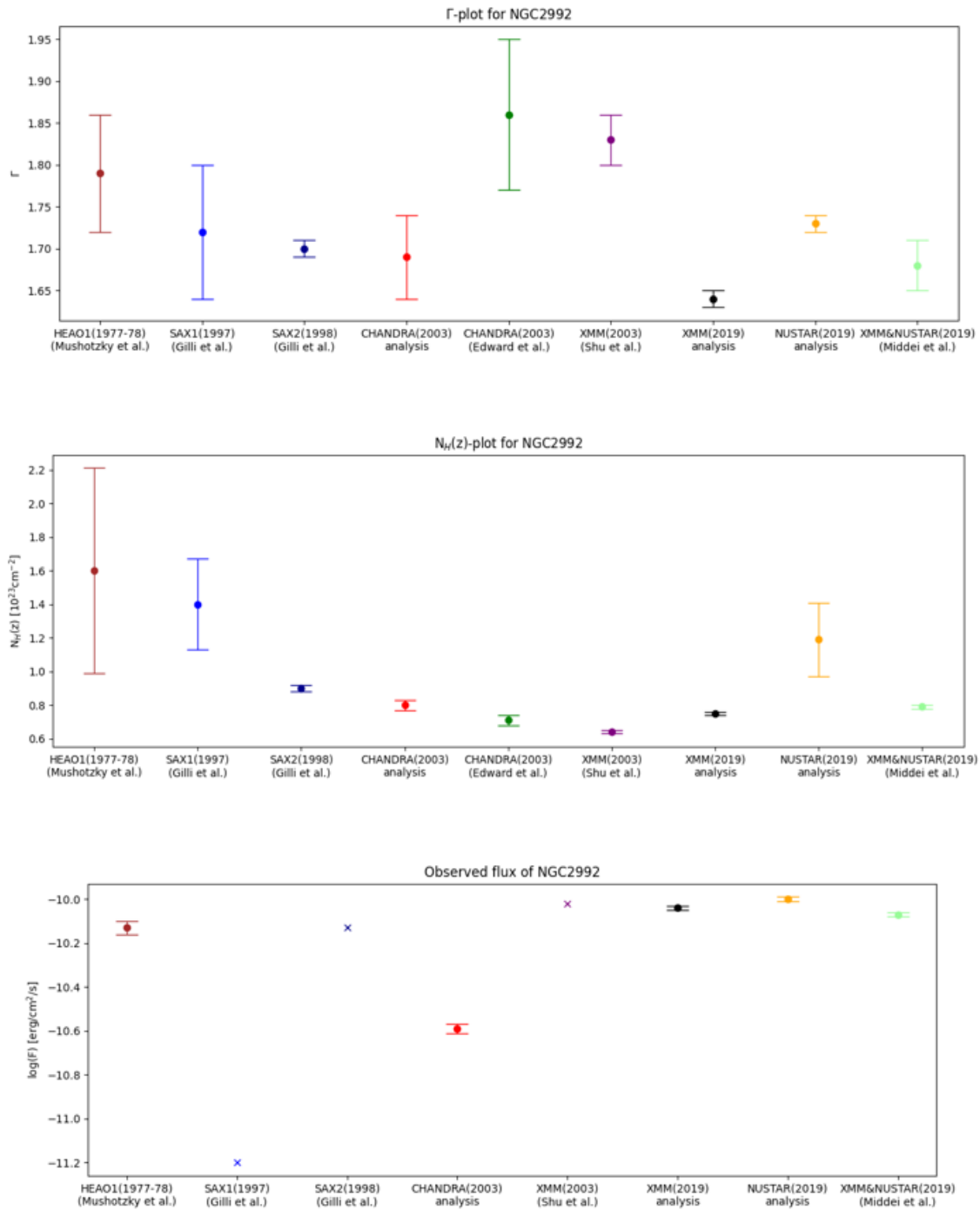


Figure 4.29: These plots illustrate the time evolution of key parameters in NGC 2992, including the spectral index, intrinsic absorption at the galaxy’s redshift, and observed flux. X-ray analysis results are presented alongside data from different epochs reported in previous studies.

The long-term monitoring of IC 5063 and NGC 2992 supports the hypothesis that AGN undergo episodic accretion phases, where periods of high activity alternate with more quiescent states. The variability in flux, absorption, and spectral properties is consistent with models where a clumpy torus dynamically evolves over time, leading to intermittent obscuration of the central engine.

4.7 Additional information from the preliminary MUSE analysis

This section presents a brief analysis of the MUSE spectra extracted from the core regions of the galaxies examined in this study. The analysis of optical spectra serves as a preliminary step to have an initial comparison with the data obtained from the X-ray analysis of the galaxy sample analyzed in this work. The spectra were obtained within a spatial range of approximately 1–3 arcseconds from the core of the galaxy, allowing for a detailed investigation of the spectral properties of the nuclear regions, that are presented in Appendix B. The scales, for an average redshift of $z=0.03$, correspond to a range of (0.5-2) kpc. This approach is particularly useful for identifying emission features that may provide further evidence supporting the X-ray analysis presented in previous sections. By focusing on the central regions, it becomes possible to distinguish AGN-related features from surrounding star-forming activity, helping to refine the classification of each source. These spectra offer valuable insights into the ionization mechanisms at play and serve as an additional diagnostic tool for confirming AGN signatures or star-forming contributions.

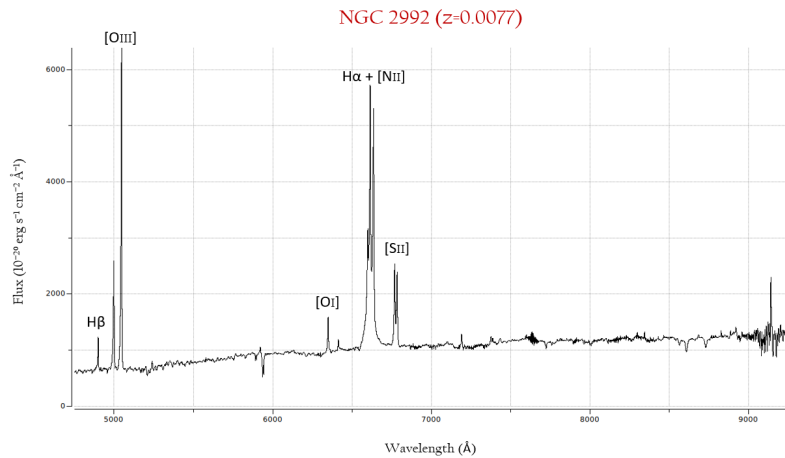


Figure 4.30: The optical spectrum of NGC 2992, obtained using MUSE data and extracted from a 2.5-arcsecond region of the nuclear area, is presented. The x-axis corresponds to the observed wavelength in Angstroms. The continuum of the spectrum appears red, this indicates that the accretion disk emission is extinguished, and therefore a significant amount of interstellar dust is absorbing blue light. The main emission lines, attributed to the presence of an AGN, are clearly visible (particularly [O III] and H α), the latter being apparently broad. This confirms that NGC 2992 hosts a Seyfert type AGN, specifically in literature it is defined as Seyfert-1.9.

To determine whether the MUSE spectra of the analyzed sources correspond to AGN

or SFGs, key spectral characteristics were examined, as emission lines and continuum shape.

If the optical continuum appears red, this can be due to several factors. One of the most common causes is dust extinction, where dust absorbs and scatters shorter-wavelength light more efficiently than longer wavelengths, making the spectrum appear redder. A high level of extinction indicates significant dust along the line of sight. The red color can also be intrinsic to the source, as in the case of old stellar populations dominated by cooler stars, or in systems where star formation has ceased and only evolved stars remain.

If the continuum appears blue, it suggests a strong presence of high-energy processes. This can occur in galaxies with AGN, the emission from the accretion disk can be approximated as a sum of blackbody spectra at different temperatures, which can then be parameterized as a power law in the UV-optical region of the spectrum. A blue continuum is also a hallmark of vigorous star formation, where young, massive O- and B-type stars emit strongly in the ultraviolet and blue optical wavelengths.

The presence of strong narrow emission lines, as low-excitation lines $H\alpha$ $\lambda 6563$ and $H\beta$ $\lambda 4861$, typically indicates star formation, while high-excitation lines such as [O III] $\lambda 5007$, and [N II] $\lambda 6548, 6584$, as well as broad components, suggest AGN activity.

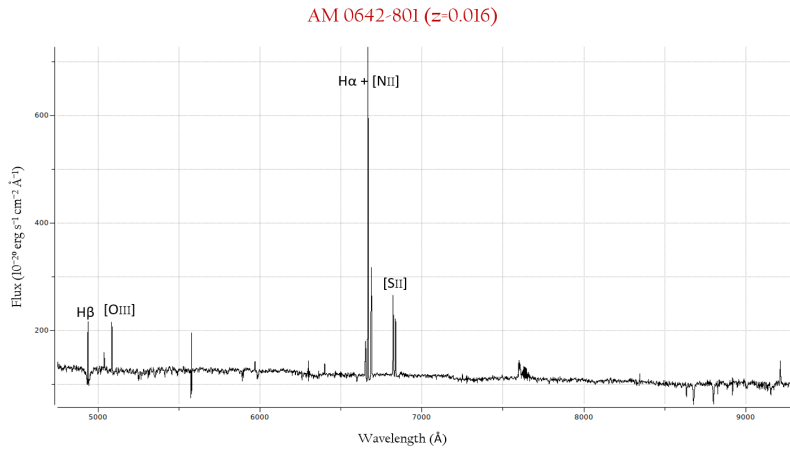


Figure 4.31: In the optical spectrum of MUSE for AM 0642-801, extracted from the core region ($r \sim 1.5$ arcsec), the $H\alpha$ line, a key indicator of star formation, appears highly prominent. On the other hand, the forbidden [O III] line is quite weak, comparable in strength to the $H\beta$ emission.

The spectral analysis revealed distinct trends among the sources. Several objects exhibited clear AGN signatures. In particular, NGC 2992 and IC 5063 displayed strong high-ionization lines, including strong [O III] emission, with no significant broad-line components, confirming their classification as Seyfert II galaxies. Similarly, other galax-

ies, such as galaxies that compose AM 0018-484 system, slightly exhibit these spectral properties, but more in-depth analysis is needed for these galaxies for an appropriate conclusion.

In contrast, several sources were more likely associated with star formation. AM 0642-801 (see 4.31), IC 0563 and other galaxies displayed strong $H\alpha$ emission but weak [O III], aligning with typical star-forming regions. A similar spectral profile was observed in AM2133-384, where a relatively flat continuum and prominent hydrogen emission lines pointed to ongoing star formation.

Some spectra instead, such as those of Arp 100 (i.e. IC 0018 and IC 0019), are quite challenging to analyze. For these types of spectra, a more in-depth analysis is certainly required.

The classification of these galaxies highlights the complexity of distinguishing AGN from star-forming activity.

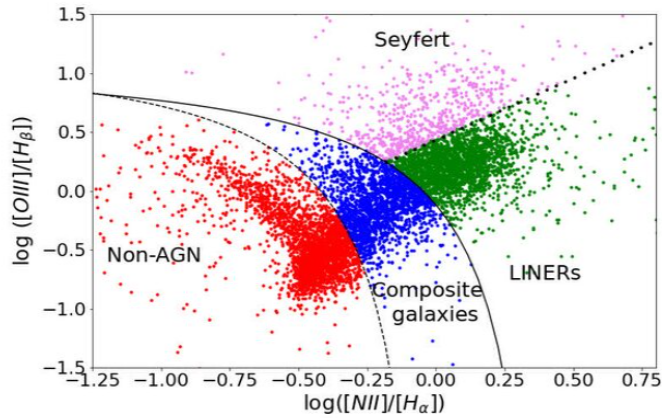


Figure 4.32: An example of a BPT diagram. By studying the line ratios of [OIII]/ $H\beta$ and [NII]/ $H\alpha$ from the MUSE optical spectra, it is possible to classify qualitatively the type of galaxy, based on where the point falls within the diagram. The different colors indicate the classification type that can be assigned to a galaxy exhibiting these emission features. From Woreta et al. 2022.

The optical spectral analysis of these sources can be further enhanced by properly creating a BPT diagram, which is a powerful tool for classifying galaxies based on their emission-line ratios. The classical BPT diagram plots the ratios of two pairs of emission lines: [O III] $\lambda 5007/H\beta$ on the y-axis and [N II] $\lambda 6584/H\alpha$ on the x-axis. These line ratios allow astronomers to distinguish between various types of ionization sources within galaxies, such as star-forming regions, AGN, and LINERs (see Fig. 4.32).

The advantage of using the BPT diagram lies in its ability to separate the emission-line spectra from star-forming galaxies and AGN. On the one hand, star-forming galaxies typically occupy a distinct region on the diagram, where the [O III] and [N II] emission

lines are relatively weak compared to $H\beta$ and $H\alpha$, respectively. On the other hand, AGN, with their strong high-ionization emission lines, fall in a separate region, indicating higher levels of ionization due to the presence of a central active nucleus. Additionally, LINERs, which represent galaxies with lower ionization states than typical AGN, occupy a region between star-forming galaxies and AGN.

Creating and analyzing a BPT diagram for the sources in this study would provide a clearer understanding of the ionization mechanisms at play in the nuclear regions. It would help confirm whether the emission lines observed are predominantly due to star formation or whether they are signatures of AGN activity. By incorporating this diagnostic tool, it could further possible to refine the classification of these galaxies, providing more robust support for the conclusions drawn from the X-ray analysis and MUSE spectral data.

Chapter 5

Discussion and future prospects

5.1 Discussion

AGN are among the most energetic and intriguing phenomena in the Universe. They are powered by the accretion of matter onto SMBHs located at the centers of galaxies, producing emissions across the entire electromagnetic spectrum. These emissions are a key tool for investigating the nature of black holes, their growth mechanisms, and their impact on galaxy evolution. A fundamental question in modern astrophysics concerns the role of galaxy interactions and mergers in triggering AGN activity. My thesis focuses on unveiling the presence and properties of AGN in a sample of interacting galaxies, using primarily X-ray observations to identify active nuclei and characterize their spectral properties.

The study is conducted within the framework of the SoSimple project, an observational program designed to explore the properties of merging galaxies using a combination of optical and X-ray data. The optical data come from the MUSE instrument at VLT, which provides integral field spectroscopy for spatially resolved studies of gas and stellar kinematics. The X-ray data are obtained from the Chandra, XMM-Newton, and NuSTAR telescopes, which allow us to probe the high-energy emission associated with AGN. The combination of these datasets enables a comprehensive analysis of how nuclear activity is linked to galaxy interactions.

A key focus of this work is the connection between AGN and galaxy interactions. Galaxy mergers are expected to funnel gas into the central regions, potentially triggering AGN activity. This process has been extensively investigated in simulations, which predict that the fraction of AGN should increase in merging galaxies compared to isolated ones. However, observational confirmation of this trend remains challenging due to selection effects and the difficulty of distinguishing AGN from star formation in the host galaxies. My thesis aims at contributing to this debate by systematically analyzing the AGN content in a sample of interacting galaxies using X-ray observations and, in a

preliminary way, MUSE data.

The sample consists of 11 interacting systems that span different stages of merger, and comprises a total of 23 targets. Eight of them are in early interaction phases ($d > 20$ kpc), where the galaxies are still well separated, while the remaining three are in advanced stages of merging or coalescence ($d < 10$ kpc), where tidal forces may have significantly altered their morphology. This diversity allows us to investigate whether AGN activity depends on the merger stage. The sources were selected based on their inclusion in the SoSimple catalog, ensuring the availability of both optical and X-ray data.

As an initial step, detection tools were used to identify various targets across different telescope observations. This analysis revealed 4 high-statistics targets ($\text{cts} > 1000$), which were examined using χ^2 statistics (Gaussian regime). Additionally, 13 low-statistics targets ($5 < \text{cts} < 300$) were analyzed using Cash statistics (Poissonian regime). The remaining 6 targets were not detected, requiring alternative methods to estimate upper limits on X-ray flux and luminosity. To this purpose, the `aprates` tool was used for Chandra data, while the web tool FLIX was applied to XMM-Newton observations, providing at least indicative X-ray properties, in particular upper limits on observed flux and X-ray luminosity in 2-10 keV band.

X-ray spectral analysis forms the core of my study, with the aim of characterizing the emission properties of the AGN. The spectra were fitted using phenomenological models that included a power-law component to describe the primary AGN emission (also accounting for the emission from possible unresolved X-ray binaries), an absorption component to account for intrinsic obscuration, and, when necessary, thermal emission components to model contributions from hot gas. The presence of Fe $K\alpha$ emission lines was also investigated, as they provide a strong indication of AGN activity.

In terms of the photon index Γ , excluding the six galaxies that were not detected and therefore lack X-ray spectral analysis, an average value $\Gamma = 1.9 \pm 0.9$ (with a dispersion for the photon index distribution of about 0.6) was obtained. Due to the lack of generally good constraints on the power-law photon index (with the exception of the few sources with the highest number of counts), it would be risky to distinguish sources as either AGN or SFG purely on the basis of the continuum emission.

The presence of Fe $K\alpha$ emission line, in particular for NGC 2992 and IC 5063 (the two brightest galaxies in X-rays) further support the AGN classification. The iron emission line has also been detected in NGC 0089 ($\text{EW} \sim 3$ keV) and in ESO119-IG054 ($\text{EW} < 3$ keV), but the presence of upper limit on the EW of the line prevents us from confidently confirming the presence of an AGN in the latter galaxy.

The observed X-ray flux distribution (Fig. 5.1) reveals that the majority of the sources exhibit flux values in the range of $\log(F/\text{erg}/\text{cm}^2/\text{s}) \sim [-14, -12]$, while only two sources display high X-ray fluxes (NGC 2992 and IC 5063).

The column density (N_{H}) distribution (Fig. 5.2) offers additional properties on the nature of these X-ray sources. From X-ray spectral analysis, an absorption component

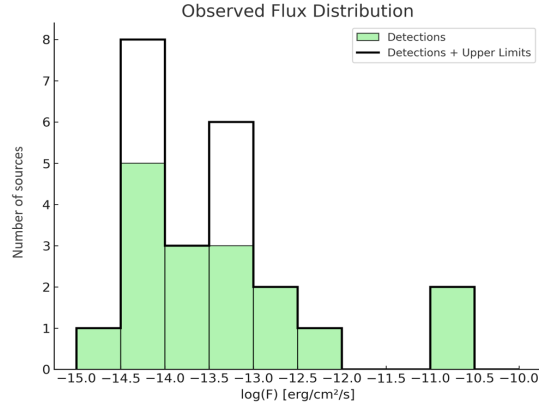


Figure 5.1: Histogram of the X-ray observed flux distribution in the 2-10 keV band, displaying detected sources (green bars) and all of the sources including both detections and upper limits (black outline). The white space between the green bars and the black outline represents the number of upper limits in each bin. The x-axis corresponds to the logarithm of the observed flux $\log(F/\text{erg}/\text{cm}^2/\text{s})$, while the y-axis indicates the number of sources per bin.

was measured only for five sources; all of the remaining sources have upper limits on N_{H} . In particular, there are three sources with $\log(N_{\text{H}}/\text{cm}^2) > 22.5$, indicative of a heavily obscured AGN, including IC 5063 (Travascio et al. 2021a) and NGC 0089, which suggests the presence of a Compton-thick AGN. The presence of these highly obscured AGN seems to support the scenario in which merger-driven gas inflows lead to increased nuclear obscuration before AGN feedback disperses the surrounding medium (e.g. Hopkins et al. 2006).

For what concerns the 2-10 keV luminosity (Fig. 5.3), the sources under investigation span a large range of values, from $\log(L/\text{erg}/\text{s}) = 39$ to 43. While NGC 2992 and IC 5063, having an X-ray luminosity above 42.5 (log), are clearly AGN, the interpretation of the remaining sources is a bit more challenging. In particular, at values below $\log(L_{\text{X}}) = 41$, low-luminosity AGN and/or emission from star forming galaxies (including unresolved X-ray binaries) may be present.

Two sources, more specifically NGC 0089 and ESO285-G019, are in the $\log(L/\text{erg}/\text{s}) \sim [41.0, 41.5]$ bin, and this luminosity range likely could be a possible indication of an actively accreting AGN.

Therefore, in conclusion, there would be two clear AGN and two potential AGN candidates.

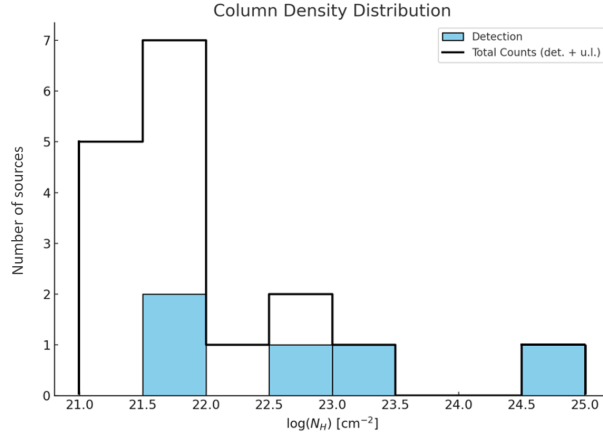


Figure 5.2: Histogram of column density distribution, illustrating detected sources (blue bars), while the black line indicates the sum of detection and upper limits (the white-space, therefore, indicates the number of upper limits present in the number of sources). The x-axis represents the logarithm of the hydrogen column density $\log(N_{\text{H}}/\text{cm}^2)$, while the y-axis indicates the number of sources in each bin.

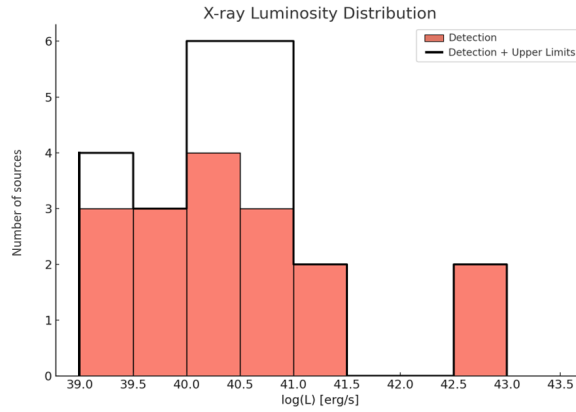


Figure 5.3: Histogram of the 2-10 keV luminosity distribution, showing detected sources (red bars) and total counts including both detections and upper limits (black outline). The white space between the red bars and the black outline represents the number of upper limits in each bin. The x-axis corresponds to the logarithm of the X-ray luminosity $\log(L/\text{erg/s})$, while the y-axis indicates the number of sources per bin.

5.1.1 MUSE Spectroscopy and AGN-SF discrimination

MUSE spectroscopic analysis may play a crucial role in differentiating AGN from star-forming galaxies by examining optical line ratios. The presence of high-ionization lines such as [O III], broad H α components, and elevated [N II]/H α ratios suggests AGN activity (Kewley et al. 2006). In my sample, notable cases include NGC 2992 and IC 5063, which exhibit clear Seyfert-like spectral signatures consistent with their X-ray classification. The detection of AGN indicators across multiple wavelengths strengthens the reliability of classification and highlights the advantages of combining X-ray and optical diagnostics.

Conversely, sources dominated by strong H α emission and weak [O III] lines, such as AM 0642-801 or AM 2133-384 (more details on Appendix B), are more consistent with star formation signatures.

After a preliminary analysis of the optical spectra of a total 23 examined sources (unfortunately, for one galaxy, IC 0267, no MUSE archive was available), the information obtained from the X-ray spectral analysis can be “combined” with that derived from the MUSE spectra to gently guess the classification of the galaxies analyzed in this study. This has been enlightened in Table 5.1, where the different sources are listed along with their X-ray indication (based on 2-10 keV luminosity) and evidences derived from optical spectra, in particular the presence of prominent emission lines (as H α and [OIII]). This provides an initial overview of which sources might host a possible AGN or are more likely to be star-forming galaxies.

In conclusion, the classification of the sources in this sample, based on their X-ray luminosity and optical spectral features, reveals a diverse population of galaxies that may host AGN activity, star formation, or a combination of both. As summarized in Table 5.1, a significant fraction of the sources exhibit H α emission, indicative of star formation, while others (i.e., NGC 2992 and IC 5063) show high X-ray luminosities and/or [OIII] emission, pointing to the presence of an AGN. Notably, several objects may harbor coexisting black hole accretion and star formation processes (e.g. NGC 0089, ESO285-G019(W)).

The “overlap” between AGN and SFG classifications highlights the complex interplay between nuclear activity and star formation, particularly in sources that may be experiencing concurrent growth of their central black hole and stellar component. While X-ray observations provide crucial insight into AGN activity, optical spectral features such as H α and [OIII] offer complementary information that may help disentangle different emission mechanisms.

Target	L_X	MUSE	AGN-like	SFG-like
NGC 0087	39.4 ± 0.3	H α		✓
NGC 0088	39.0 ± 0.5	H α		✓
NGC 0089	41.4 ± 0.9	H α	✓	
NGC 0092	40.5 ± 0.1	H α	✓	✓
AM 0642-801	39.7 ± 0.3	H α		✓
WISEA J0	< 39.4	H α		✓
ESO119-IG054	40.8 ± 0.2	H α	✓	✓
ESO119-IG055	39.8 ± 0.8	none		
AM 2133-384 (c1)	40.8 ± 0.2	H α	✓	✓
AM 2133-384 (c2)	39.8 ± 0.6	H α		✓
ESO285-G019 (W)	41.2 ± 1.0	H α	✓	✓
ESO285-G019 (E)	< 40.5	none		
NGC 1134	40.3 ± 0.3	H α		✓
IC 0267	< 40.2	no spectrum		
UGC 05304a	< 40.4	none		
UGC 05304b	40.7 ± 0.2	H α	✓	✓
IC 0563	40.1 ± 0.4	H α		✓
IC 0564	39.3 ± 0.7	H α		✓
NGC 2992	42.5 ± 0.1	[OIII], H α	✓	
NGC 2993	40.1 ± 0.1	H α		✓
IC 5063	42.5 ± 0.1	[OIII], H α	✓	
IC 0018	< 40.9	H α		✓
IC 0019	< 40.9	none		

Table 5.1: Summary of the X-ray luminosities (L_X) and optical (MUSE) spectral classifications for the analyzed sample. The AGN-like classification is assigned to sources with $\log(L_X/\text{erg/s}) \geq 40.5$, as high X-ray luminosities are indicative of accreting supermassive black holes. Additionally, the presence of strong [OIII] emission line also may lead to an AGN-like classification regardless of the X-ray luminosity. The SFG-like classification is attributed to sources that either exhibit moderate X-ray luminosity or show prominent H α emission in their optical spectra, a strong indicator of intense star formation. In the cases where both AGN and SFG indicators are present, the classification could be AGN, star-forming galaxies or composite systems that harbor both AGN activity and significant star formation. Entries marked as “none” indicate the absence of indicative emission lines, most likely classifiable as passive galaxies. The green symbols are for the two, already well-known AGN.

5.2 Conclusion and future prospects

The analysis in my thesis work revealed a diverse range of AGN properties. In particular, one source, NGC 0089, which is part of the AM 0018-485 system, showed evidence of being heavily obscured AGN, with extremely high column density ($N_{\text{H}} > 10^{24} \text{ cm}^{-2}$) and strong Fe $K\alpha$ line, suggesting, for the first time in the literature, that could be a Compton-thick AGN. Other sources, like NGC 2992 or IC 5063, exhibited moderate-to-high absorption and a clear AGN spectral signature, with a prominent power-law component and reflection features indicative of X-ray reprocessing by surrounding material, in literature classified as Seyfert-Type AGNs. In contrast, the majority of galaxies in the sample, such as AM 0642-801, showed weak or negligible AGN activity, suggesting that not all interacting galaxies host active nuclei. These sources could potentially be SFGs; alternatively, the X-ray emission might be a combination of both components.

A further step has been taken by initiating a very preliminary analysis of the optical MUSE spectra of these sources to gather more information for a more complete classification of the objects in the analyzed sample. This can be seen as a starting point to investigate the presence of AGN in interacting systems.

In the future, an effort could be made to expand this initial catalog to obtain a larger statistical sample, allowing for a better quantification of the AGN fraction in a completely unbiased sample. This could then be compared with a control sample of isolated galaxies (at the same redshift and with similar stellar mass distribution) to examine potential differences and assess whether galaxy interactions may serve as a triggering mechanism for AGN activity.

Additionally, with a statistically larger sample and a stricter analysis approach, a comparison could be made with some of the most significant studies in this field, as Koss et al. 2012, who found that approximately 10% of hard X-ray selected AGN are in mergers, and Ellison et al. 2013, who reported a 2–3 \times increase in AGN activity in closely interacting systems compared to isolated galaxies.

In addition to the detected sources, my thesis also addresses the non-detections, for which upper limits on the X-ray luminosity were estimated. These upper limits help constrain the AGN fraction in interacting galaxies and provide insights into whether some AGN possibly remain hidden due to extreme obscuration. The presence of dual AGN was also investigated, but no strong evidence was found, suggesting that simultaneous activation of both black holes in merging systems may be rare. The limited size of the sample prevents us from drawing firm conclusions on the increasing AGN activity at later stages of the merger. It would be interesting to expand in the future this analysis, since mergers are expected to play an interesting role in fueling SMBHs. It must be said, though, that this process might be complex, since the availability of cold gas, the efficiency of angular momentum transport, and feedback may impact AGN activation.

Furthermore, deep observations in the hard X-ray band ($E > 10 \text{ keV}$), particularly with NuSTAR, could help identify heavily obscured AGN that may have been missed

in the present study. Multi-wavelength follow-ups, including radio and infrared observations, would also be valuable in further constraining the nature of the AGN population in merging galaxies.

An essential complement to this analysis will be the use of appropriate BPT diagrams (i.e., properly removing the stellar continuum) derived from MUSE spectroscopic data. The BPT diagrams allow for the classification of emission-line galaxies by distinguishing AGN from star-forming regions based on key diagnostic line ratios such as $[\text{O III}]/\text{H}\beta$ and $[\text{N II}]/\text{H}\alpha$. This will enable a direct comparison between X-ray-detected AGN and optically classified AGN candidates, providing a deeper understanding of the relationship between nuclear activity and galaxy interactions. By mapping spatially resolved BPT diagnostics across merger systems, it will be possible to investigate how AGN ionization regions evolve during different merger stages, offering a more complete picture of AGN triggering mechanisms.

In conclusion, my thesis provides insights-though very preliminary-into the connection between galaxy interactions and AGN activity, demonstrating that mergers are an important driver of SMBH accretion, but that the relationship is complex and influenced by multiple factors. The results contribute to a better understanding of the co-evolution of galaxies and their central black holes, a key question in extragalactic astrophysics.

Appendix A

Dataset table information

Target	RA (J2000)	DEC (J2000)	Obsid	Date	Exp (ks)	Off-axis angle (')
Chandra						
Arp245	09:45:45.462	-14:21:16.57	3956	2003-02-16	49.54	1.5
Arp303	09:46:20.707	+03:03:42.52	15070	2013-01-19	14.96	0.2
AM0642-801	06:38:36.050	-80:14:48.01	14925	2013-08-27	38.47	0.0
AM2026-424	20:29:32.620	-42:30:14.86	22360	2019-09-01	9.92	2.9
AM0519-611	05:20:17.681	-61:16:40.42	13001	2011-02-06	4.90	0.3
AM2048-571	20:52:01.846	-57:04:17.40	7878	2007-06-15	34.10	0.0
XMM-Newton						
Arp245	09:45:45.462	-14:21:16.57	0840920201	2019-05-07	134.30	0.0
Arp255	09:53:09.433	+07:52:07.40	0103260801	2002-05-08	84.29	3.6
AM0642-801	06:38:36.050	-80:14:48.01	0781710101	2016-05-03	46.90	4.3
Arp100	00:28:36.727	-11:34:50.71	0742500701	2014-12-21	10.00	9.5
AM0018-485	00:21:23.017	-48:38:02.67	0152330101	2002-12-24	47.96	0.1
Arp200	02:53:40.299	+13:00:48.17	0693540101	2012-07-19	24.77	0.1
NuSTAR						
Arp245	09:45:45.462	-14:21:16.57	90501623002	2019-05-10	57.49	2.1
AM2048-571	20:52:01.846	-57:04:17.40	60061302002	2013-07-08	18.45	1.9

Table A.1: This table shows the main information about all the observations from the three X-ray Chandra, XMM-Newton and NuSTAR telescopes that were analyzed in this thesis work. The colored targets indicate cases of multiple observations found on more than one telescope. Where the off-axis angle turns out to be 0.0 means that the system is the target of the observation.

Appendix B

MUSE spectra

The following section provides a very preliminary analysis of the MUSE spectra presented in this study, focusing on the classification of the observed sources into AGN, SFGs, and unclassified cases where the spectral features remain ambiguous. The classification is based on the identification of key spectral lines, the continuum shape, and emission line-ratios.

The spectra analyzed were extracted using the MUSE data cube, focusing on the core region of each host galaxy to maximize the contribution from nuclear emission while minimizing contamination from surrounding stellar populations and star-forming regions. Given the different spatial extent of nuclear emission across different galaxies, a variable extraction radius was employed, ranging from 1 to 3 arcseconds, depending on the compactness of the emission in each case. The selection of the extraction aperture was optimized to maximize nuclear emission by centering the region of the host galaxy's core and to minimize extended star-forming contamination, particularly in systems with prominent tidal features or diffuse ionized gas. It should be noted that for Arp 200's companion galaxy (a.k.a. NGC 1134), specifically IC 0267, no available MUSE data archive has been found. As a result, the optical spectrum of the core region is not available for this galaxy.

Several sources in the sample exhibit strong high-ionization emission lines and broad spectral components, indicative of AGN activity. The defining spectral features include:

- Strong [O III] $\lambda 5007$ emission, often exceeding $H\beta$ in intensity.
- Presence of [N II] $\lambda 6584$ and $H\alpha$ broad component, suggesting a significant contribution from an accretion-powered ionization mechanism.
- Spectrum with a usually flat or red continuum which may be due to extinction.

The spectra of NGC 2992 (see Fig. 4.30) and IC 5063 display clear AGN signatures. NGC 2992 exhibits a Seyfert-type spectrum, with apparent broad $H\alpha$ emission and a

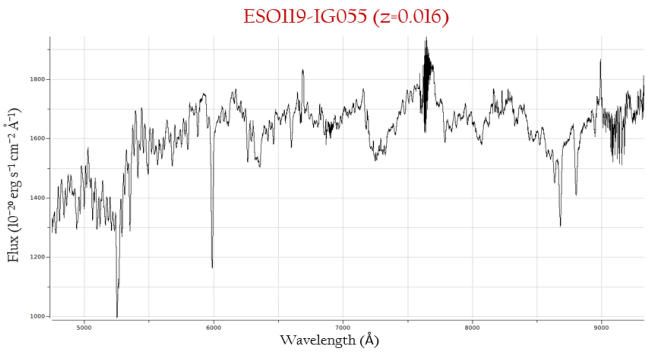
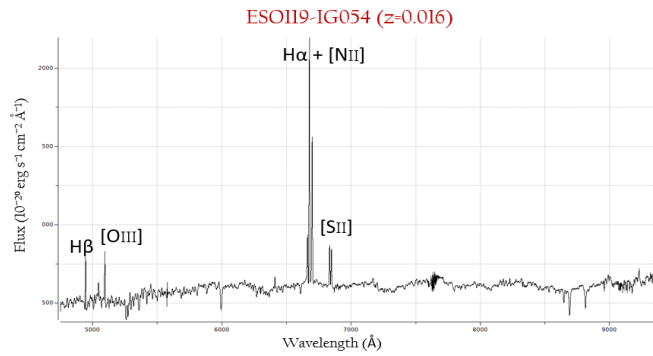
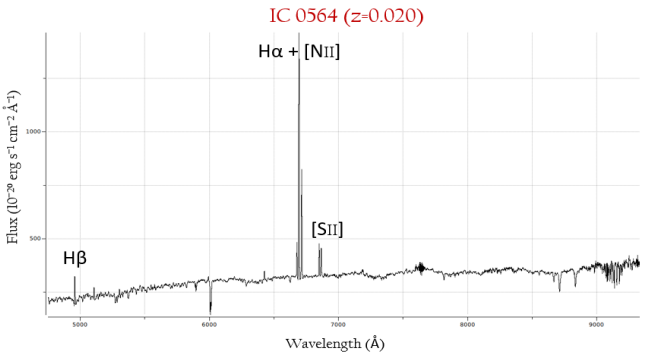
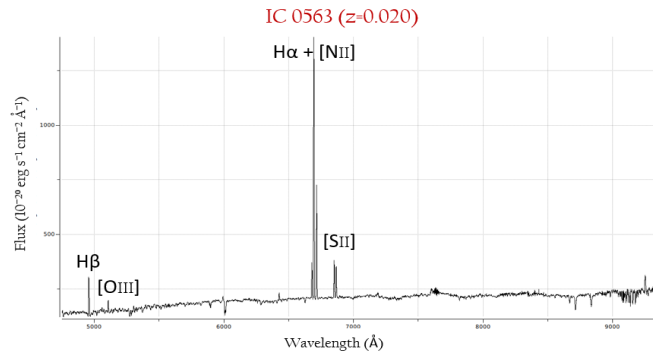
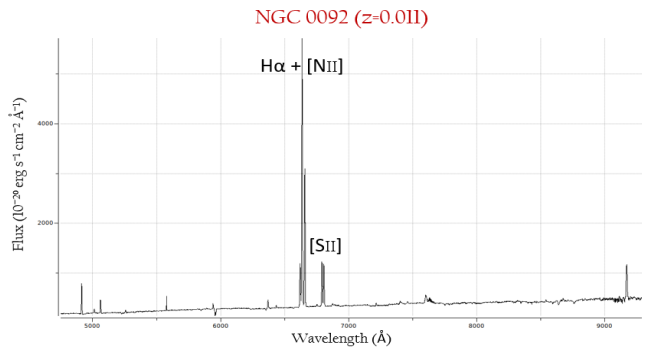
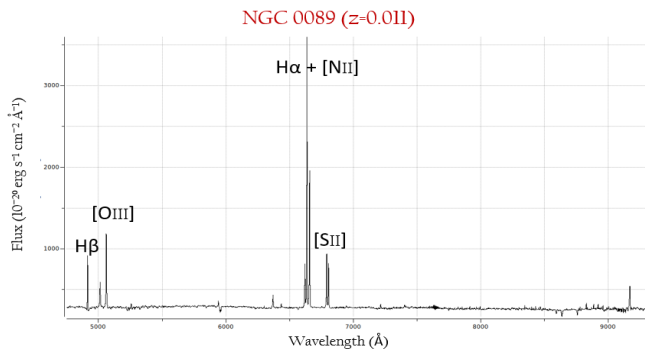
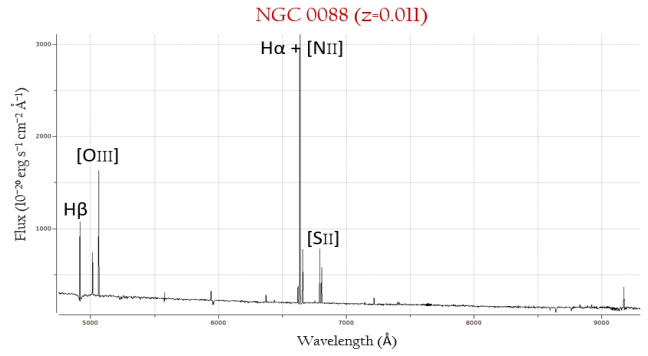
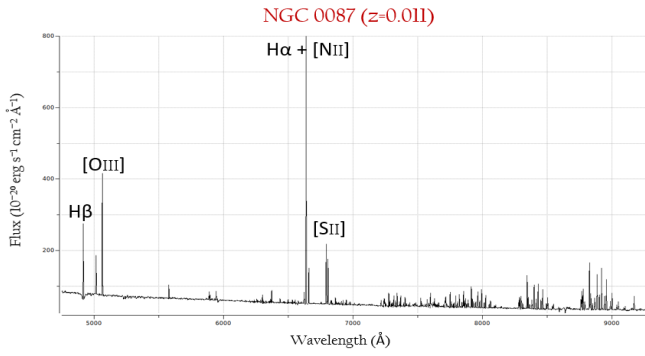
strong [O III] line, classified in the literature as Seyfert-1.8/1.9, most likely due to the fact that it exhibits a highly extinct disk continuum, typical of Seyfert Type-II galaxies. Conversely, IC 5063 shows characteristics of a Seyfert II galaxy, with prominent narrow emission lines indicative of AGN activity in a highly obscured nucleus.

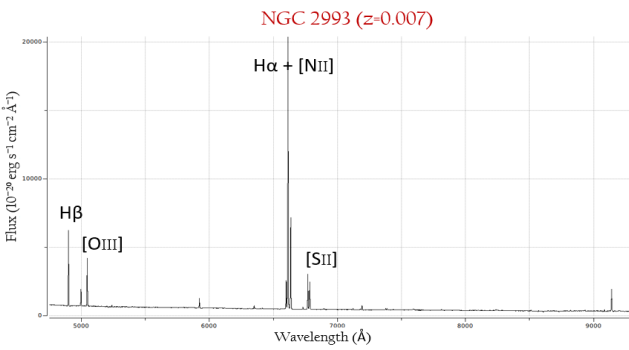
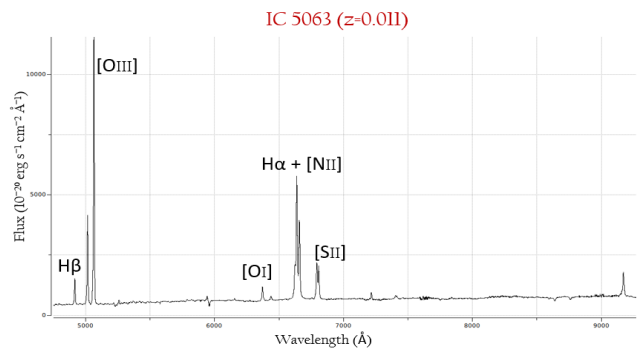
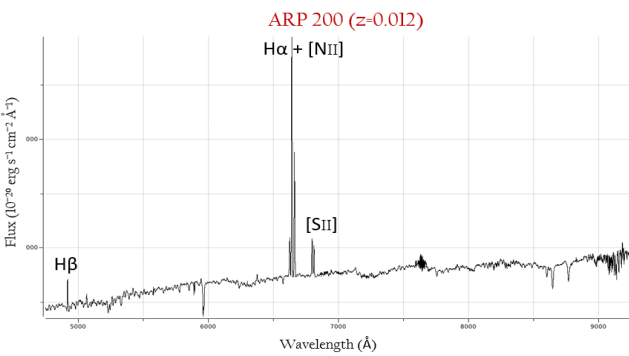
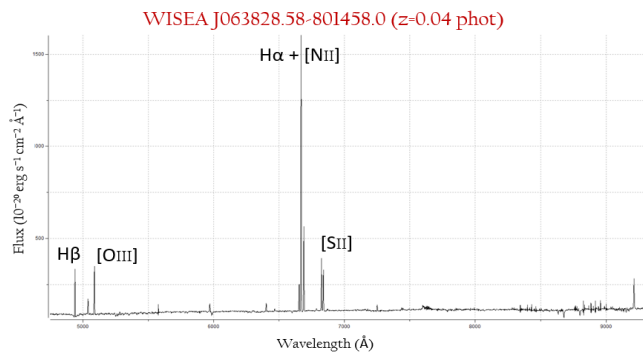
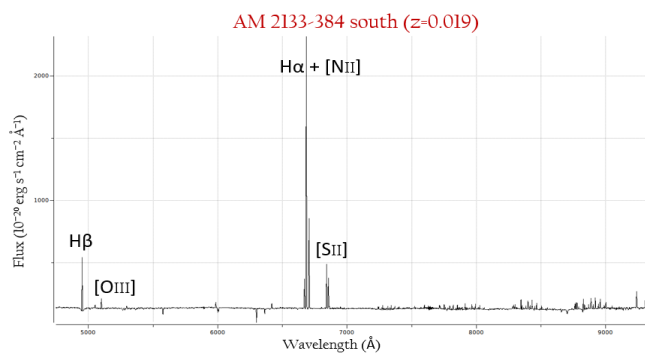
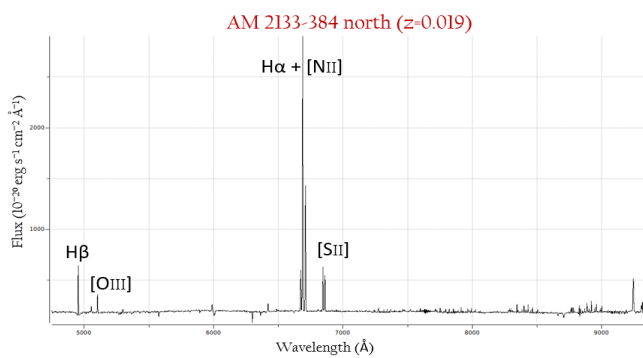
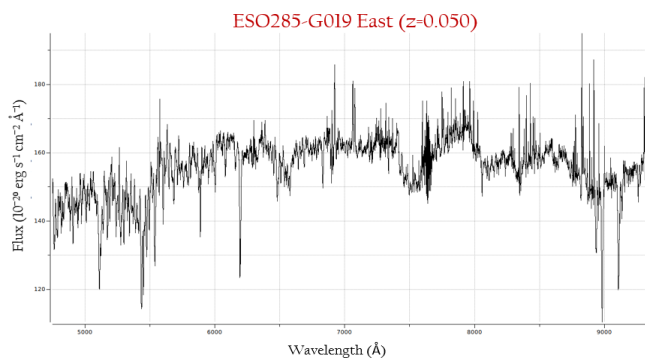
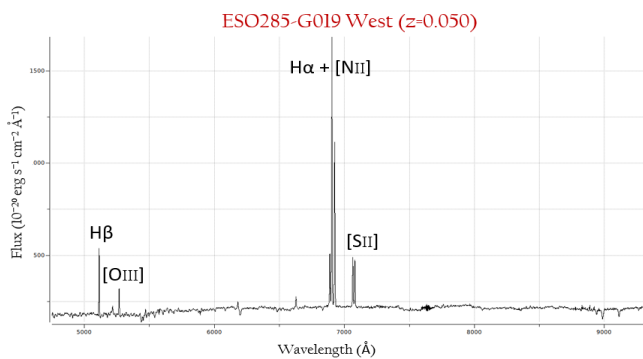
Similarly, NGC 0089 reveal high-ionization condition that suggest AGN-like behavior. Its spectrum contain narrow [O III] and [N II] lines that align with the expected ionization mechanisms of AGN. The other galaxies in AM 0018-485 (NGC 0087, NGC 0088 and NGC 0092) also exhibit prominent emission lines, which could suggest an AGN classification. However, their low X-ray luminosities ($\log(L_X) < 40$ erg/s) are more consistent with SF galaxies. For a more detailed analysis of these sources, which present possible “intermediate” or uncertain classifications, a future in-depth study of their optical spectra is required. This would first involve subtracting the stellar continuum (e.g. through ppxf (Cappellari 2012)) and then evaluating the key line ratios. By using a BPT diagram, it would be possible to determine where these sources fall within the classification scheme, providing a clearer understanding of their nature.

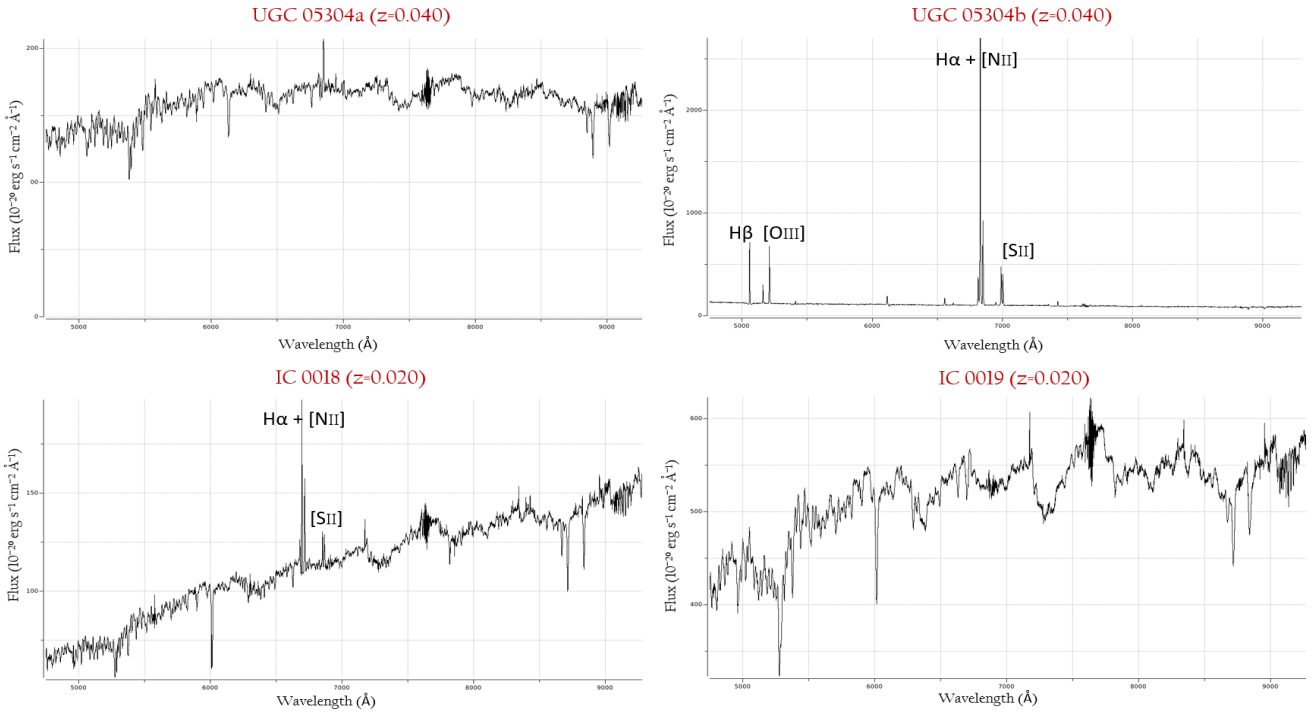
In contrast, several sources show emission features typically associated with ongoing star formation, with key indicators including:

- Strong $H\alpha$ emission, significantly exceeding [O III].
- Weak [N II] and [O III] lines, consistent with photoionization by young stellar populations rather than AGN activity.
- Relatively sloped or blue continuum, indicative of active star formation of young population stars in the host galaxy; however, it can also be attributed to the presence of an AGN (Vanden Berk et al. 2001).

Examples include AM 0642-801 (see Fig. 4.31), IC 0563, and AM 2133-384, which all display dominant $H\alpha$ emission with weak [O III] contributions. In these cases, the spectra suggest active star formation as the primary ionization mechanism.







Furthermore, some spectra remain ambiguous due to the presence of mixed ionization signatures or insufficient spectral resolution. For example, Arp 100 (IC 0018 and IC 0019) spectral features do not clearly distinguish between AGN and star-forming ionization. Other cases present spectra which can be classified as passive galaxies: sources like UGC 05304a or ESO285-G019 (East component) that lack prominent emission lines. Passive galaxies are galaxies that exhibit little to no ongoing star formation. They are typically characterized by old stellar populations, low gas content, and a red spectral continuum. These galaxies have already exhausted or lost most of their cold gas, which is necessary for star formation, and are often dominated by evolved stars, such as red giants and white dwarfs.

Bibliography

- Abazajian, Kevork N. et al. (2009). “The Seventh Data Release of the Sloan Digital Sky Survey”. In: *The Astrophysical Journal, Supplement* 182, pp. 543–558.
- Abramowicz, Marek et al. (1995). “Thermal equilibria of accretion disks”. In: *arXiv preprint astro-ph/9409018*.
- Ahn, Christopher P. et al. (2012). “The Ninth Data Release of the Sloan Digital Sky Survey: First Spectroscopic Data from the SDSS-III Baryon Oscillation Spectroscopic Survey”. In: *The Astrophysical Journal, Supplement* 203, p. 21.
- Almeida, R. Cristina and Claudio Ricci (2017). “Nuclear obscuration in active galactic nuclei”. In: *arXiv astro-ph/1709.00019*.
- Antonucci (1993). “Unified models for active galactic nuclei and quasars”. In: *Annual review of astronomy and astrophysics* 31, pp. 473–521.
- Antonucci and Miller (1985). “Spectropolarimetry and the nature of NGC 1068”. In: *The Astrophysical Journal* 297, pp. 621–632.
- Armus, L. et al. (2009). “GOALS: The Great Observatories All-Sky LIRG Survey”. In: *Publications of the Astronomical Society of the Pacific* 121.880, pp. 559–576.
- Arnaud, K. A. (Jan. 1996). “XSPEC: The First Ten Years”. In: *Astronomical Data Analysis Software and Systems V*. Ed. by George H. Jacoby and Jeannette Barnes. Vol. 101. Astronomical Society of the Pacific Conference Series, p. 17.
- Arp, Halton C. and B. Madore (1987). *A catalogue of southern peculiar galaxies and associations*.
- Baldi et al. (2015). “Pilot study of the radio-emitting AGN population: the emerging new class of FR 0 radio-galaxies”. In: *Astronomy & Astrophysics* 576, A38.
- Baldwin, J. A., M. M. Phillips, and R. Terlevich (Feb. 1981). “Classification parameters for the emission-line spectra of extragalactic objects.” In: *Publications of the Astronomical Society of the Pacific* 93, pp. 5–19.
- Barrera-Ballesteros et al. (2015). “Tracing kinematic (mis)alignments in CALIFA merging galaxies - Stellar and ionized gas kinematic orientations at every merger stage”. In: *Astronomy & Astrophysics* 582, A21.
- Beckmann, Volker and Chris R. Shriver (2012). *Active Galactic Nuclei*.
- Berk, Daniel E Vanden et al. (2001). “Composite quasar spectra from the sloan digital sky survey”. In: *The Astronomical Journal* 122.2, p. 549.

- Blandford and DG Payne (1982). “Hydromagnetic flows from accretion discs and the production of radio jets”. In: *Monthly Notices of the Royal Astronomical Society* 199.4, pp. 883–903.
- Blandford and Martin J Rees (1978). “Extended and compact extragalactic radio sources: interpretation and theory”. In: *Physica Scripta* 17.3, p. 265.
- Blandford and Roman L Znajek (1977). “Electromagnetic extraction of energy from Kerr black holes”. In: *Monthly Notices of the Royal Astronomical Society* 179.3, pp. 433–456.
- Blecha, Laura, Abraham Loeb, and Ramesh Narayan (Jan. 2013). “Double-peaked narrow-line signatures of dual supermassive black holes in galaxy merger simulations”. In: *Monthly Notices of the Royal Astronomical Society* 429.3, pp. 2594–2616.
- Buchner et al. (2019). “X-ray spectral and eclipsing model of the clumpy obscurer in active galactic nuclei”. In: *arXiv preprint arXiv:1907.13137*.
- Bundy, Kevin et al. (2015). “Overview of the SDSS-IV MaNGA Survey: Mapping nearby Galaxies at Apache Point Observatory”. In: *The Astrophysical Journal* 798.1, p. 7.
- Burtscher, Leonard et al. (2013). “A diversity of dusty AGN tori—Data release for the VLTI/MIDI AGN Large Program and first results for 23 galaxies”. In: *Astronomy & Astrophysics* 558, A149.
- Caldwell, N. and M. M. Phillips (Mar. 1981). “An observational inquiry into the nature of the galaxy IC 5063.” In: *The Astrophysical Journal* 244, pp. 447–457.
- Capelo, Pedro R. et al. (May 2017). “A survey of dual active galactic nuclei in simulations of galaxy mergers: frequency and properties”. In: *Monthly Notices of the Royal Astronomical Society* 469.4, pp. 4437–4454.
- Capetti et al. (2020). “Large-scale environment of FR 0 radio galaxies”. In: *Astronomy & Astrophysics* 633, A161.
- Cappellari, Michele (Oct. 2012). *pPXF: Penalized Pixel-Fitting stellar kinematics extraction*. Astrophysics Source Code Library, record ascl:1210.002.
- Carrera, F. J. et al. (July 2007). “The XMM-Newton serendipitous survey. III. The AXIS X-ray source counts and angular clustering”. In: *Astronomy & Astrophysics* 469.1, pp. 27–46.
- Cash, W. (1979). “Parameter estimation in astronomy through application of the likelihood ratio”. In: *Astrophysical Journal, Part 1* 228, pp. 939–947.
- Chen et al. (1995). “Unified description of accretion flows around black holes”. In: *arXiv preprint astro-ph/9502015*.
- Colbert, Edward J. M. et al. (July 2005a). “Extranuclear X-Ray Emission in the Edge-on Seyfert Galaxy NGC 2992”. In: *The Astronomical Journal* 628.1, pp. 113–128.
- (July 2005b). “Extranuclear X-Ray Emission in the Edge-on Seyfert Galaxy NGC 2992”. In: *The Astrophysical Journal* 628.1, pp. 113–128.
- Condon, J. J. (1992). “Radio emission from normal galaxies.” In: *Annual Review of Astronomy and Astrophysics* 30, pp. 575–611.

- Condon, J. J., W. D. Cotton, and J. J. Broderick (2002). “Radio Sources and Star Formation in the Local Universe”. In: *The Astronomical Journal* 124.2, pp. 675–689.
- Czerny, Bozena and Martin Elvis (1987). “Constraints on quasar accretion disks from the optical/ultraviolet/soft X-ray big bump”. In: *The Astrophysical Journal* 321, pp. 305–320.
- Dadina, Mauro (2008). “Seyfert galaxies in the local Universe ($z < 0.1$): the average X-ray spectrum as seen by BeppoSAX”. In: *Astronomy & Astrophysics* 485.2, pp. 417–424.
- Darg, D. W. et al. (2010). “Galaxy Zoo: the fraction of merging galaxies in the SDSS and their morphologies”. In: *Monthly Notices for the Royal Astronomical Society* 401, pp. 1043–1056.
- Das et al. (1985). “Kinematics of the Narrow-Line Region in the Seyfert 2 Galaxy NGC 1068: Dynamical Effects of the Radio Jet”. In: *The Astronomical Journal* 132.2, p. 620.
- Davies, L. J. M. et al. (2015). “Galaxy And Mass Assembly (GAMA): the effect of close interactions on star formation in galaxies”. In: *Monthly Notices for the Royal Astronomical Society* 452, pp. 616–636.
- De Rosa, Alessandra et al. (2019). “The quest for dual and binary supermassive black holes: A multi-messenger view”. In: *New Astronomy Reviews* 86, p. 69.
- De Rosa, Alessandra et al. (Dec. 2023). “The X-ray view of optically selected dual AGN”. In: *Monthly Notices of the Royal Astronomical Society* 519.4, pp. 5149–5160.
- Dey, Arjun et al. (2008). “A significant population of very luminous dust-obscured galaxies at redshift $z \sim 2$ ”. In: *The Astronomical Journal* 677.2, p. 943.
- Djorgovski, S. G. et al. (2007). “Discovery of a Probable Physical Triple Quasar”. In: *The Astrophysical Journal, Letters* 662, pp. L1–L5.
- Donato, D et al. (2001). “Hard X-ray properties of blazars”. In: *Astronomy & Astrophysics* 375.3, pp. 739–751.
- Done (2007). “The Origin of the soft excess in AGN”. In: *arXiv preprint astro-ph/0703449*.
- Donley, J. L. et al. (2005). “Unveiling a Population of AGNs Not Detected in X-Rays”. In: *The Astrophysical Journal* 634, pp. 169–182.
- Dopita, M. A. et al. (2002). “Star Formation Rates in Interacting Starburst Galaxies”. In: *The Astrophysical Journal Supplement* 143.1, pp. 47–72.
- Eisenhardt et al. (2012). “The first hyper-luminous infrared galaxy discovered by WISE”. In: *The Astrophysical Journal* 755.2, p. 173.
- Elitzur, Moshe (2008). “The toroidal obscuration of active galactic nuclei”. In: *New Astronomy Reviews* 52.6, pp. 274–288.
- Ellison et al. (May 2008). “Galaxy Pairs in the Sloan Digital Sky Survey. I. Star Formation, Active Galactic Nucleus Fraction, and the Mass-Metallicity Relation”. In: *The Astronomical Journal* 135.5, pp. 1877–1899.
- (2018). “Star formation is boosted (and quenched) from the inside-out: radial star formation profiles from MaNGA”. In: *Monthly Notices for the Royal Astronomical Society* 474, pp. 2039–2054.

- Ellison et al. (2013). “Galaxy pairs in the Sloan Digital Sky Survey - VIII. The observational properties of post-merger galaxies”. In: *Monthly Notices of the Royal Astronomical Society* 435, pp. 3627–3638.
- Faber, S. M. et al. (2007). “Galaxy Luminosity Functions to $z \sim 1$ from DEEP2 and COMBO-17: Implications for Red Galaxy Formation”. In: *The Astrophysical Journal* 665, pp. 265–294.
- Fabian (2000). “Broad iron lines in active galactic nuclei”. In: *Publications of the Astronomical Society of the Pacific* 112.775, p. 1145.
- Fabian and Giovanni Miniutti (2005). “The X-ray spectra of accreting Kerr black holes”. In: *arXiv preprint astro-ph/0507409*.
- Fadda, Dario and Giulia Rodighiero (2014). “The hunt for red active galactic nuclei: a new infrared diagnostic”. In: *Monthly Notices of the Royal Astronomical Society: Letters* 444, pp. L95–L99.
- Fanaroff, Bernard L and Julia M Riley (1974). “The morphology of extragalactic radio sources of high and low luminosity”. In: *Monthly Notices of the Royal Astronomical Society* 167.1, 31P–36P.
- Farina, E. P. et al. (2013). “Caught in the act: discovery of a physical quasar triplet”. In: *Monthly Notices of the Royal Astronomical Society* 431, pp. 1019–1025.
- Fazio, GG et al. (2004). “The infrared array camera (IRAC) for the spitzer space telescope”. In: *The Astrophysical Journal Supplement Series* 154.1, p. 10.
- Fernandez, Luis C. et al. (Mar. 2022). “FRAMEX. II. Simultaneous X-Ray and Radio Variability in Active Galactic Nuclei-The Case of NGC 2992”. In: *The Astronomical Journal* 927.1, p. 18.
- Foreman, G et al. (2009). “Double Quasars: Probes of Black Hole Scaling Relationships and Merger Scenarios”. In: *The Astrophysical Journal* 693, pp. 1554–1562.
- Fossati, G et al. (1998). “A unifying view of the spectral energy distributions of blazars”. In: *Monthly Notices of the Royal Astronomical Society* 299.2, pp. 433–448.
- Fragos, T. et al. (2013). “X-Ray Binary Evolution Across Cosmic Time”. In: *The Astrophysical Journal* 764, p. 41.
- Ghisellini et al. (1994). “The contribution of the obscuring torus to the X-ray spectrum of Seyfert galaxies: a test for the unification model”. In: *Monthly Notices of the Royal Astronomical Society* 267.3, pp. 743–754.
- Gierlinski and Done (2004). “Is the soft excess in active galactic nuclei real?” In: *Monthly Notices of the Royal Astronomical Society* 349.1, pp. L7–L11.
- Gilli, R. et al. (Mar. 2000). “The variability of the Seyfert galaxy NGC 2992: the case for a revived AGN”. In: *Astronomy and Astrophysics* 355, pp. 485–498.
- Gofford, Jason et al. (Jan. 2013). “The Suzaku view of highly ionized outflows in AGN – I. Statistical detection and global absorber properties”. In: *Monthly Notices of the Royal Astronomical Society* 430.1, pp. 60–80.
- Halpern, JP (1984). “Variable X-ray absorption in the QSO MR 2251-178”. In: *the Astrophysical Journal* 281, pp. 90–94.

- Harrison, C. M. et al. (2014). “Kiloparsec-scale outflows are prevalent among luminous AGN: outflows and feedback in the context of the overall AGN population”. In: *Monthly Notices of the Royal Astronomical Society* 441, pp. 3306–3347.
- Hatziminaoglou et al. (2015). “A complete census of silicate features in the mid-infrared spectra of active galaxies”. In: *The Astrophysical Journal* 803.2, p. 110.
- Heckman, Timothy M and Philip N Best (2014). “The coevolution of galaxies and supermassive black holes: insights from surveys of the contemporary universe”. In: *Annual Review of Astronomy and Astrophysics* 52, pp. 589–660.
- Helou, G et al. (1985). “Thermal infrared and nonthermal radio : remarkable correlation in disks of galaxies.” In: *The Astrophysical Journal Letters* 298, pp. L7–L11.
- Hickox and Alexander (2018). “Obscured active galactic nuclei”. In: *Annual Review of Astronomy and Astrophysics* 56, pp. 625–671.
- Hine, RG and MS Longair (1979). “Optical spectra of 3CR radio galaxies”. In: *Monthly Notices of the Royal Astronomical Society* 188.1, pp. 111–130.
- Hopkins, Philip F. et al. (2006). “The Relation between Quasar and Merging Galaxy Luminosity Functions and the Merger-driven Star Formation History of the Universe”. In: *The Astrophysical Journal* 652, pp. 864–888.
- Hunter, Stanley D. et al. (2010). “Development of the Advance Energetic Pair Telescope (AdEPT) for medium-energy gamma-ray astronomy”. In: *SPIE Proceedings*. Ed. by Monique Arnaud, Stephen S. Murray, and Tadayuki Takahashi. SPIE.
- Ibar, Edo et al. (2008). “Exploring the infrared/radio correlation at high redshift”. In: *Monthly Notices of the Royal Astronomical Society* 386, pp. 953–962.
- Ichimaru, SETSUO (1977). “Bimodal behavior of accretion disks-Theory and application to Cygnus X-1 transitions”. In: *The Astrophysical Journal* 214, pp. 840–855.
- Iverson, R. J. et al. (2010). “The far-infrared/radio correlation as probed by Herschel”. In: *Astronomy & Astrophysics* 518, p. L31.
- Jaffe, Walter et al. (2004). “MIDI observations of the nuclear obscuring torus in NGC 1068”. In: *Proceedings of the International Astronomical Union* 2004.IAUS222, pp. 37–39.
- Jogee, Shardha et al. (2009). “History of Galaxy Interactions and Their Impact on Star Formation Over the Last 7 Gyr from GEMS”. In: *The Astrophysical Journal* 697, pp. 1971–1992.
- Kaspi, Shai et al. (2002). “The ionized gas and nuclear environment in NGC 3783. I. Timeaveraged 900 kilosecond Chandra grating spectroscopy”. In: *The Astrophysical Journal* 574.2, p. 643.
- Kaviraj, Sugata (2014). “The importance of minor-merger-driven star formation and black hole growth in disc galaxies”. In: *Monthly Notices of the Royal Astronomical Society* 440, pp. 2944–2952.
- Kellermann, KI et al. (1989). “VLA observations of objects in the Palomar Bright Quasar Survey”. In: *The Astronomical Journal* 98, pp. 1195–1207.

- Kewley, Lisa J. et al. (Nov. 2006). “The host galaxies and classification of active galactic nuclei”. In: *Monthly Notices of the Royal Astronomical Society* 372.3, pp. 961–976.
- Kewley, Lisa J. et al. (2010). “METALLICITY GRADIENTS AND GAS FLOWS IN GALAXY PAIRS”. In: *The Astrophysical Journal Letters* 721, p. L48.
- Kimball, Amy E and Željko Ivezić (2008). “A unified catalog of radio objects detected by NVSS, first, WENSS, GB6, and SDSS”. In: *The Astronomical Journal* 136.2, p. 684.
- Komossa, S. et al. (Jan. 2002). “NGC 6240, local key representative and pathfinder to the high-redshift universe of ULIRGs: the Chandra high-resolution view.” In: *Astronomische Gesellschaft Abstract Series*. Vol. 19. Astronomische Gesellschaft Abstract Series, pp. 46–46.
- Konstantopoulos, Iraklis et al. (2013). “The SAMI IFU Galaxy Survey”. In: *American Astronomical Society Meeting Abstracts #221*. Vol. 221. American Astronomical Society Meeting Abstracts, p. 215.01.
- Koss, Michael et al. (Feb. 2012). “UNDERSTANDING DUAL ACTIVE GALACTIC NUCLEUS ACTIVATION IN THE NEARBY UNIVERSE”. In: *The Astrophysical Journal* 2, p. L22.
- Koyama, Katsuji et al. (Nov. 1992). “Hard X-Ray Emission from a Narrow-Line Radio Galaxy IC 5063 and Obscured Active Nucleus”. In: *The Astrophysical Journal Letters* 399, p. L129.
- Krolik, Julian Hand Mitchell C Begelman (1988). “Molecular tori in Seyfert galaxies—Feeding the monster and hiding it”. In: *The Astrophysical Journal* 329, pp. 702–711.
- Laor, Ari (2000). “On Black Hole Masses and Radio Loudness in Active Galactic Nuclei”. In: *The Astrophysical Journal Letters* 543, pp. L111–L114.
- (June 2003). “On the Nature of Low-Luminosity Narrow-Line Active Galactic Nuclei”. In: *The Astrophysical Journal* 590.1, pp. 86–94.
- Ledlow, Michael J and Frazer N Owen (1996). “Optical Properties of Rich-Cluster Radio Galaxies”. In: *Energy Transport in Radio Galaxies and Quasars* 100, p. 359.
- Lehmer, B. D. et al. (2016). “The Evolution of Normal Galaxy X-Ray Emission through Cosmic History: Constraints from the 6 MS Chandra Deep Field-South”. In: *The Astrophysical Journal* 825, p. 7.
- Lin et al. (2004). “The DEEP2 Galaxy Redshift Survey: Evolution of Close Galaxy Pairs and Major-Merger Rates up to $z \sim 1.2$ ”. In: *The Astrophysical Journal, Letters* 617, pp. L9–L12.
- (2008). “The Redshift Evolution of Wet, Dry, and Mixed Galaxy Mergers from Close Galaxy Pairs in the DEEP2 Galaxy Redshift Survey”. In: *Panoramic Views of Galaxy Formation and Evolution*. Ed. by T. Kodama, T. Yamada, and K. Aoki. Vol. 399. Astronomical Society of the Pacific Conference Series, p. 298.
- Lotz, Jennifer M. et al. (2010). “The effect of gas fraction on the morphology and time-scales of disc galaxy mergers”. In: *Monthly Notices of the Royal Astronomical Society* 404, pp. 590–603.

- Lusso, Elisabeta et al. (2018). “The Spectral and Environment Properties of $z \sim 2.0$ -2.5 Quasar Pairs”. In: *The Astrophysical Journal* 860, p. 41.
- Madore, Barry F., Erica Nelson, and Kristen Petrillo (2009). “Atlas and Catalog of Collisional Ring Galaxies”. In: *The Astrophysical Journal Supplement Series* 181.2, pp. 572–604.
- Malkan et al. (1982). “The ultraviolet excess of Seyfert 1 galaxies and quasars”. In: *The Astrophysical Journal* 254, pp. 22–37.
- Maloney, Philip and Christopher Reynolds (2000). “ASCA Observation of an X-Ray-luminous Active Nucleus in Markarian 231”. In: *The Astrophysical Journal* 545.
- Mao, Minnie Y. et al. (2011). “No Evidence for Evolution in the Far-infrared-Radio Correlation out to $z \sim 2$ in the Extended Chandra Deep Field South”. In: *The Astrophysical Journal* 731, p. 79.
- Maoz, Dan (2007). “Low-luminosity active galactic nuclei: are they UV faint and radio loud?” In: *Monthly Notices of the Royal Astronomical Society* 377, pp. 1696–1710.
- McElroy, R. E. et al. (2016). “The Close AGN Reference Survey (CARS). Mrk 1018 returns to the shadows after 30 years as a Seyfert 1”. In: *Astronomy & Astrophysics* 593, p. L8.
- Meusinger, H. and N. Balafkan (2014). “A large sample of Kohonen-selected SDSS quasars with weak emission lines: selection effects and statistical properties”. In: *Astronomy & Astrophysics* 568, A114.
- Mewe, R., EHBM Gronenschild, and GHJ Van Den Oord (1985). “Calculated X-radiation from optically thin plasmas. V”. In: *Astronomy and Astrophysics supplement series* 62, pp. 197–254.
- Middei, R. et al. (Aug. 2022). “The lively accretion disc in NGC 2992 - II. The 2019/2021 X-ray monitoring campaigns”. In: *Monthly Notices of the Royal Astronomical Society* 514.2, pp. 2974–2993.
- Miller (1990). “The bimodal radio luminosity function of quasars.” In: *Monthly Notices of the Royal Astronomical Society* 244, pp. 207–213.
- Mitsuda, Kazuhisa et al. (1984). “Energy spectra of low-mass binary X-ray sources observed from TENMA”. In: *Publications of the Astronomical Society of Japan* 36, pp. 741–759.
- Morić, I. et al. (2010). “A Closer View of the Radio-FIR Correlation: Disentangling the Contributions of Star Formation and Active Galactic Nucleus Activity”. In: *The Astrophysical Journal* 724, pp. 779–790.
- Mukherjee, Dipanjan et al. (Jan. 2018). “The jet–ISM interactions in IC 5063”. In: *Monthly Notices of the Royal Astronomical Society* 476.1, pp. 80–95.
- Murakami, Hiroshi et al. (2007). “The infrared astronomical mission AKARI”. In: *Publications of the Astronomical Society of Japan* 59.sp2, S369–S376.
- Murphy, K. D., M. A. Nowak, and H. L. Marshall (May 2017). “The Nuclear X-Ray Emission-line Structure in NGC 2992 Revealed by Chandra-HETGS”. In: *The Astronomical Journal* 840.2, p. 120.

- Mushotzky, R. F. et al. (Sept. 1980). “The X-Ray Spectra and Time Variability of Narrow Emission Line Galaxies”. In: *Bulletin of the American Astronomical Society*. Vol. 12, p. 873.
- Nandra, K and KA Pounds (1994). “Ginga observations of the X-ray spectra of Seyfert galaxies”. In: *Monthly Notices of the Royal Astronomical Society* 268.2, pp. 405–429.
- Narayan, Ramesh and Jeffrey E McClintock (2008). “Advection-dominated accretion and the black hole event horizon”. In: *New Astronomy Reviews* 51.10-12, pp. 733–751.
- Narayan, Ramesh and Insu Yi (1994). “Advection-dominated accretion: A self-similar solution”. In: *arXiv preprint astro-ph/9403052*.
- Neenkova, Maia et al. (2002). “Dust emission from active galactic nuclei”. In: *The Astrophysical Journal Letters* 570.1, p. L9.
- Netzer, Hagai (2002). “The density and location of the X-ray-absorbing gas in NGC 3516”. In: *The Astrophysical Journal* 571.1, p. 256.
- (2013). “The physics and evolution of active galactic nuclei”. In: *Cambridge University Press*.
- (2015). “Revisiting the unified model of active galactic nuclei”. In: *Annual Review of Astronomy and Astrophysics* 53, pp. 365–408.
- Neugebauer, G et al. (1984). “The infrared astronomical satellite (IRAS) mission”. In: *The Astrophysical Journal* 278, pp. L1–L6.
- Nikolic, B et al. (2004). “Star formation in close pairs selected from the Sloan Digital Sky Survey”. In: *Monthly Notices of the Royal Astronomical Society* 355, pp. 874–886.
- Osterbrock, Donald E (1978). “Observational model of the ionized gas in seyfert and radiogalaxy nuclei”. In: *Proceedings of the National Academy of Sciences* 75.2, pp. 540–544.
- Padovani (2016). “The faint radio sky: radio astronomy becomes mainstream”. In: *The Astronomy and Astrophysics Review* 24.1, p. 13.
- (2017). “Active galactic nuclei: what’s in a name?” In: *The Astronomy and Astrophysics Review* 25.1, p. 2.
- Padovani et al. (2011). “The VLA Survey of Chandra Deep Field South. V. Evolution and Luminosity Functions of Sub-millijansky Radio Sources and the Issue of Radio Emission in Radio-quiet Active Galactic Nuclei”. In: *The Astrophysical Journal* 740, p. 20.
- Papovich, Casey et al. (Dec. 2003). “The Internal Ultraviolet-Optical Color Dispersion: Quantifying the Morphological K-Correction”. In: *The Astrophysical Journal* 598.2, pp. 827–847.
- Peterson, B.M. (2008). “The central black hole and relationships with the host galaxy”. In: *New Astronomy Reviews* 52, pp. 240–252.
- Petrucci, P-O et al. (2018). “Testing warm Comptonization models for the origin of the soft X-ray excess in AGNs”. In: *Astronomy & Astrophysics* 611, A59.

- Qiao, Erlin et al. (2013). “THE DISK EVAPORATION MODEL FOR THE SPECTRAL FEATURES OF LOW-LUMINOSITY ACTIVE GALACTIC NUCLEI”. In: *The Astrophysical Journal* 777, p. 102.
- Rich, J. A. et al. (2012). “An Integral Field Study of Abundance Gradients in nearby Luminous Infrared Galaxies”. In: *The Astrophysical Journal* 753, p. 5.
- Risaliti and Martin Elvis (2004). “A Panchromatic view of AGN”. In: *Supermassive Black Holes in the Distant Universe* Springer, pp. 187–224.
- Ross et al. (2015). “Extremely red quasars from SDSS, BOSS and WISE: classification of optical spectra”. In: *Monthly Notices of the Royal Astronomical Society* 453.4, pp. 3932–3952.
- Roy, A. L. and R. P. Norris (1997). “Radio-excess infrared galaxies: a new population of active galaxies?” In: *Monthly Notices of the Royal Astronomical Society* 289, pp. 824–830.
- Sánchez et al. (2014). “A characteristic oxygen abundance gradient in galaxy disks unveiled with CALIFA”. In: *Astronomy & Astrophysics* 563, A49.
- Sánchez et al. (2012). “CALIFA, the Calar Alto Legacy Integral Field Area survey. I. Survey presentation”. In: *Astronomy & Astrophysics* 538, A8.
- Satyapal, Shobita et al. (2014). “Galaxy pairs in the Sloan Digital Sky Survey - IX. Merger-induced AGN activity as traced by the Wide-field Infrared Survey Explorer”. In: *Monthly Notices of the Royal Astronomical Society* 441, pp. 1297–1304.
- Schawinski et al. (2014). “The green valley is a red herring: Galaxy Zoo reveals two evolutionary pathways towards quenching of star formation in early- and late-type galaxies”. In: *Monthly Notices for the Royal Astronomical Society* 440, pp. 889–907.
- (2015). “Active galactic nuclei flicker: an observational estimate of the duration of black hole growth phases of $\sim 10^5$ yr”. In: *Monthly Notices for the Royal Astronomical Society* 451, pp. 2517–2523.
- Seyfert, Carl K (1943). “Nuclear Emission in Spiral Nebulae”. In: *The Astrophysical Journal* 97, p. 28.
- Seymour, N. et al. (2008). “The Contribution of Radio Selected Star Forming Galaxies to the IR Energy Density Budget”. In: *Panoramic Views of Galaxy Formation and Evolution*. Ed. by T. Kodama, T. Yamada, and K. Aoki. Vol. 399. Astronomical Society of the Pacific Conference Series, p. 197.
- Shakura, N. I. and R. A. Sunyaev (1973). “Reprint of 1973A&A.... 24.. 337S. Black holes in binary systems. Observational appearance.” In: *A&A* 500, pp. 33–51.
- Sharma, Ray S et al. (Nov. 2023). “The connection between mergers and AGN activity in simulated and observed massive galaxies”. In: *Monthly Notices of the Royal Astronomical Society* 527.3, pp. 9461–9479.
- Shemmer, Ohad et al. (2010). “Weak Line Quasars at High Redshift: Extremely High Accretion Rates or Anemic Broad-line Regions?” In: *The Astrophysical Journal Letters* 722, pp. L152–L156.

- Shu, X. W. et al. (Apr. 2010). “NGC 2992 in an X-ray High State Observed by XMM-Newton: Response of the Relativistic Fe K α Line to the Continuum”. In: *The Astrophysical Journal* 713.2, pp. 1256–1265.
- Singh, Ankit et al. (2023). “On the Effects of Local Environment on Active Galactic Nucleus (AGN) in the Horizon Run 5 Simulation”. In: *The Astrophysical Journal* 953:64, p. 17.
- Steinborn, Lisa K. et al. (2016). “Origin and properties of dual and offset active galactic nuclei in a cosmological simulation at $z=2$ ”. In: *Monthly Notices for the Royal Astronomical Society* 458, pp. 1013–1028.
- Stern et al. (2005). “Mid-infrared selection of active galaxies”. In: *The Astrophysical Journal* 631.1, p. 163.
- Stewart, Kyle R. et al. (2008). “Merger Histories of Galaxy Halos and Implications for Disk Survival”. In: *The Astrophysical Journal* 683, pp. 597–610.
- Stocke, John T. et al. (1992). “The Radio Properties of the Broad-Absorption-Line QSOs”. In: *The Astrophysical Journal* 396, p. 487.
- Tazaki, Fumie et al. (Sept. 2011). “Suzaku View of the Swift/BAT Active Galactic Nuclei. IV. Nature of Two Narrow-line Radio Galaxies (3C 403 and IC 5063)”. In: *The Astrophysical Journal* 738.1, 70, p. 70.
- Telfer, Randal C et al. (2002). “The rest-frame extreme-ultraviolet spectral properties of quasi-stellar objects”. In: *The Astrophysical Journal* 565.2, p. 773.
- Tombesi et al. (Oct. 2010). “Evidence for ultra-fast outflows in radio-quiet AGNs: I. Detection and statistical incidence of Fe K-shell absorption lines”. In: *Astronomy and Astrophysics* 521, A57.
- (2013). “The density and location of the X-ray-absorbing gas in NGC 3516”. In: *Monthly Notices of the Royal Astronomical Society* 430.2, pp. 1102–1117.
- (2014). “Ultrafast outflows in radio-loud active galactic nuclei”. In: *Monthly Notices of the Royal Astronomical Society* 443, pp. 2154–2182.
- Tran, Kim-Vy H. et al. (2005). “Spectroscopic Confirmation of Multiple Red Galaxy-Galaxy Mergers in MS 1054-03 ($z = 0.83$)1,” in: *The Astrophysical Journal, Letters* 627, pp. L25–L28.
- Travascio, A. et al. (Nov. 2021a). “AGN-Host Interaction in IC 5063. I. Large-scale X-Ray Morphology and Spectral Analysis”. In: *The Astrophysical Journal* 921.2, 129, p. 129.
- (Nov. 2021b). “AGN-Host Interaction in IC 5063. I. Large-scale X-Ray Morphology and Spectral Analysis”. In: *The Astrophysical Journal* 921.2, 129, p. 129.
- Trump, Jonathan R. et al. (2009). “The Nature of Optically Dull Active Galactic Nuclei in COSMOS”. In: *The Astrophysical Journal* 706, pp. 797–809.
- Urry and Padovani (1995). “Unified schemes for radio-loud active galactic nuclei”. In: *Publications of the Astronomical Society of the Pacific* 107.715, p. 803.

- Van Wassenhove, Sandor et al. (Feb. 2012). “OBSERVABILITY OF DUAL ACTIVE GALACTIC NUCLEI IN MERGING GALAXIES”. In: *The Astrophysical Journal Letters* 748.1, p. L7.
- Vanden Berk, Daniel E. et al. (Aug. 2001). “Composite Quasar Spectra from the Sloan Digital Sky Survey”. In: *The Astronomical Journal* 122.2, pp. 549–564.
- Vignali, C. et al. (Jan. 1997). “ASCA and ROSAT X-ray spectra of IC 5063 and NGC 3998.” In: *Mem. Societa Astronomica Italiana* 68, pp. 139–140.
- Volonteri, Marta et al. (July 2022). “Dual AGN in the Horizon-AGN simulation and their link to galaxy and massive black hole mergers, with an excursus on multiple AGN”. In: *Monthly Notices of the Royal Astronomical Society* 514.1, pp. 640–656.
- Ward, M. et al. (Nov. 1980). “New optical and radio observations of the X-ray galaxies NGC 7582 and NGC 2992.” In: *Monthly Notices of the Royal Astronomical Society* 193, pp. 563–582.
- Webb, N. A. et al. (July 2020). *VizieR Online Data Catalog: XMM-Newton Serendipitous Source Catalogue 4XMM-DR9 (Webb+, 2020)*.
- Werner, Michael W et al. (2004). “The Spitzer space telescope mission”. In: *The Astrophysical Journal Supplement Series* 7 154.1, p. 1.
- Weston, Madalyn E. et al. (2017). “Incidence of WISE -selected obscured AGNs in major mergers and interactions from the SDSS”. In: *Monthly Notices of the Royal Astronomic Society* 464, pp. 3882–3906.
- Wheeler, John A. and Remo Ruffini (1971). “Introducing the black hole”. In: *Physics Today* 24, issue 1, pp. 30–41.
- Woods, Deborah Freedman and Margaret J. Geller (2007). “Minor Galaxy Interactions: Star Formation Rates and Galaxy Properties”. In: *The Astronomical Journal* 134, pp. 527–540.
- Woreta, Tilahun et al. (Mar. 2022). *Effect of AGN on the morphological properties of their host galaxies in the local Universe*.
- Wright, Edward L et al. (2010). “The Wide-field Infrared Survey Explorer (WISE): mission description and initial on-orbit performance”. In: *The Astronomical Journal* 140.6, p. 1868.
- York, Donald G. et al. (2000). “The Sloan Digital Sky Survey: Technical Summary”. In: *The Astronomical Journal* 120, pp. 1579–1587.
- Yun et al. (2001). “Radio Properties of Infrared-selected Galaxies in the IRAS 2 Jy Sample”. In: *The Astrophysical Journal* 554, pp. 803–822.